Technical Physics Letters, Vol. 29, No. 11, 2003, pp. 879–881. Translated from Pis'ma v Zhurnal Tekhnicheskoĭ Fiziki, Vol. 29, No. 21, 2003, pp. 1–6.

Subnanosecond Electron Beams Formed in a Gas-Filled Diode

V. F. Tarasenko[a,*], V. G. Shpak[b], S. A. Shunaĭlov[b], M. I. Yalandin[b], V. M. Orlovskiĭ[a], and S. B. Alekseev[a]

[a] *Institute of High-Current Electronics, Siberian Division, Russian Academy of Sciences, Tomsk, Russia*
[b] *Institute of Electrophysics, Ural Division, Russian Academy of Sciences, Yekaterinburg, Russia*
** e-mail: VFT@loi.hcei.tsc.ru*

Received April 22, 2003

Abstract—We have studied the conditions for the formation of a pulsed beam of runaway electrons in a diode filled with air at atmospheric pressure, whereby the current and voltage pulses in the system were measured with a subnanosecond time resolution. It is experimentally demonstrated for the first time that the electron beam appears on the leading front of the voltage pulse at a relatively small voltage on the discharge gap. At atmospheric pressure, a full width at half maximum of the current pulse does not exceed 0.3 ns. © *2003 MAIK "Nauka/Interperiodica".*

Introduction. Previously, we demonstrated that the use of high-voltage pulse generators with nanosecond front widths for discharge excitation provides for a significant increase in the runaway electron beam current in a gas diode filled with helium [1] or molecular gases (such as air, nitrogen, or CO_2–N_2–He mixtures) [2]. It was shown that electron beams with amplitudes reaching tens and hundreds of amperes can form at an average value of the E/p ratio as small as ~0.1 kV/(cm Torr), where E is the electric field strength and p is the gas pressure [1, 2]. This value is significantly below a critical level for the electron runaway effect [3].

The formation of runaway electron beams and X-ray radiation pulses in gas-filled diodes has been extensively studied (see, e.g., monograph [3], review [4], and references in [1–4]). However, the time resolution of detecting instrumentation used in these investigations was never better than 1 ns, which allowed neither detection of the onset of the runaway electron beam formation at elevated gas pressures nor determination of the current pulse duration. The lack of such data complicates understanding of the physical pattern of the phenomenon and the selection of conditions making the electron runaway effect most pronounced.

The aim of our experiments was to study the runaway electron beam formation in an air-filled diode at atmospheric pressure and small average E/p values, using detection equipment providing for subnanosecond time resolution.

Experimental. The experiments were performed with nanosecond pulse generators of the RADAN type [5, 6]. The first generator (RADAN-303 [5]) possessed an output wave impedance of 45 Ω and produced voltage pulses with a full width at half maximum (FWHM) of ~5 ns, a front width of ~1 ns, and an amplitude from 50 to 170 kV amplitude in a matched load (in the open circuit regime, the amplitude reached 340 kV). With this generator, the voltage applied to the discharge gap could be smoothly controlled. Another generator (RADAN-220 [6]) possessed an output wave impedance of 20 Ω and produced in the discharge gap a voltage pulse with an amplitude of up to ~220 kV (matched mode), a FWHM of ~2 ns, and a front width of ~0.3 ns. This generator was used in our previous experiments for obtaining electron beams in gas-filled diodes [2].

Figure 1 presents a schematic diagram of the gas-filled diode and indicates the position of a capacitive voltage divider. The cathode represented a tube with a diameter of 6 mm, made of a 50-μm-thick steel foil. The cathode–anode spacing in this system could be set within 13–20 mm. The electron beam was extracted from the diode via a 40-μm-thick AlBe foil, a 10-μm thick Al foil, or a grid with a geometric transparency of 0.5. Using a grid in the output window allowed visual observation of a discharge operating in the gas-filled diode.

The beam current was measured using a copper disk collector with a diameter of 49 mm, spaced by 10 mm from the output foil. The collector was loaded with a coaxial cable or with a cable and a low-ohmic shunt. In some experiments, the current was collected on small-area electrodes loaded with coaxial cables or on a graphite electrode connected to a strip line or a Faraday cup. The Faraday cup design allowed the space between the output foil and measuring electrode to be differentially pumped. The electron energy distribution was determined using the foil technique.

The measuring electrodes were connected to an oscillograph with wideband coaxial cables and attenuators of the 142-NM type (Barth Electronics) with a

1063-7850/03/2911-0879$24.00

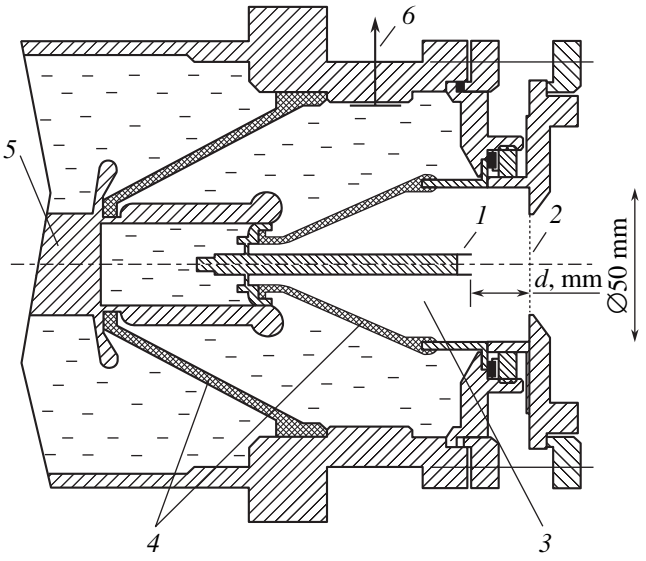

Fig. 1. A schematic diagram of the high-voltage generator output and a gas-filled diode: (*1*) cathode; (*2*) output window with foil or grid; (*3*) gas-filled diode; (*4*) insulators; (*5*) generator electrode; (*6*) capacitive voltage divider.

bandwidth of 30 GHz (at a –3 dB level). This allowed us to measure pulses with a front width of 0.1 ns. The detection circuit was tested using a low-voltage generator of pulses with a front width of 70 ps and a 6-GHz stroboscopic oscillograph of the TDS-820 type. At a 100-ps pulse front width, a decrease in the voltage pulse amplitude did not exceed 20%, while the amplitude of pulses with a 400-ps front width decreased by no more than 5%. Signals from the capacitive voltage divider and the electron beam collectors were measured using a digital oscillograph of the TDS-684B type (1 GHz and 5 Gs/s, which corresponds to 5 points/ns).

Results and discussion. Measurements of the beam current behind the foil or grid were performed for various anode–cathode distances and foil thicknesses in the diode driven by each of the two pulse generators. In the experiments with RADAN-303, it was possible to monitor the beam current and voltage pulses simultaneously. Figure 2 shows oscillograms of the electron beam current in the regime of maximum amplitude and oscillograms of the voltage pulses measured on the discharge gap and on the matched load (the latter is compared to the results of calculations using code KARAT [7]).

As can be seen from Fig. 2, the FWHM of the beam current pulse does not exceed ~0.4 ns (curves *1* and *3*) and decreases to ~0.3 ns (curve *2*) for the measurements using small-area electrodes (the latter value corresponds to the limiting resolution of a TDS-684B oscillograph). The maximum values of the beam current amplitude behind the 40-μm-thick AlBe foil was ~75 A for RADAN-220 (Fig. 2, curve *1*) and ~35 A for RADAN-303 (Fig. 2, curve *3*). A comparison of the data obtained with RADAN-220 to the results reported

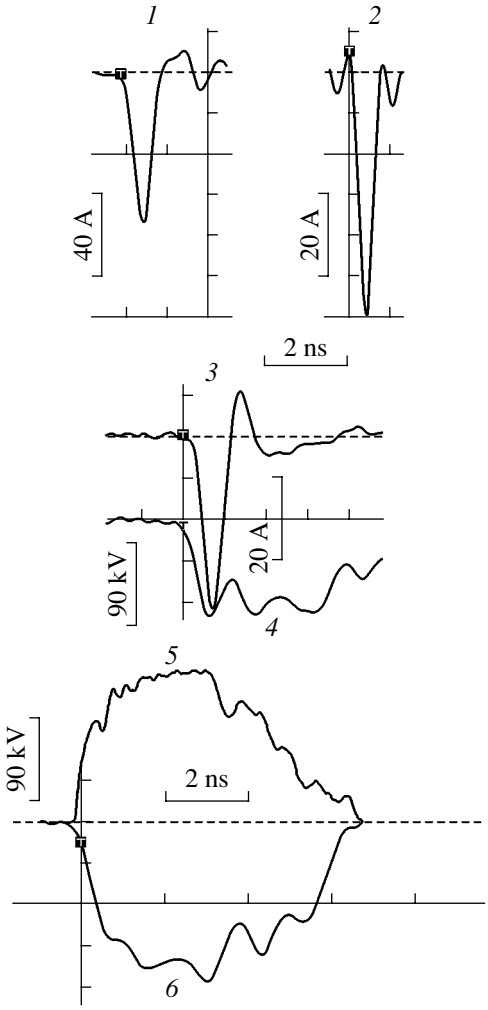

Fig. 2. Oscillograms of (*1–3*) the electron beam current pulses behind the foil and (*4–6*) the voltage pulses (*4*) on the gas diode and (*5*, *6*) on the matched load (calculation and experiment, respectively). Time scale: 1 ns/div (*1–4*); 2 ns/div (*5*, *6*). Gas pressure in the diode: p = 1 bar. Cathode–anode gap width: 16 mm (*1*, *2*); 17 mm (*3*, *4*). Generator: RADAN-220 (*1*, *2*); RADAN-303 (*3*, *4*, *6*). Current amplitude scale: 20 A/div (*1*); 10 A/div (*2*, *3*). Voltage amplitude scale: 45 kV/div (*4–6*).

previously [2] shows that increasing time resolution of the detection system has led to an increase in the current pulse amplitude and a decrease in the pulse width, while a product of the pulse amplitude by the pulse width remained virtually the same. The behavior of the runaway electron beam current amplitude depending on the experimental conditions was also the same as that observed in [1, 2]. The minimum electron beam current pulse width observed in the new experiments was ~0.3 ns (Fig. 2, curve *2*).

The high-resolution measurements showed that the electron beam appears on the leading front of the voltage pulse and terminates on a plateau of this pulse. The average value of the E/p ratio at the moment of the electron beam formation on the voltage pulse front is

~3 times lower than the value of this parameter upon termination of the electron beam current pulse. Termination of the current pulse at a high voltage on the discharge gap is probably explained by shunting of the anode–cathode gap by a plasma propagating from the cathode. As a result, the field distribution in the gap becomes more uniform and the critical E/p values (required for the electron runaway and the beam extraction through the foil) are not reached. An average electron energy in the beam measured for the RADAN-303 generator and a 40-μm-thick AlBe foil was ~60 keV, which amounts to about 60% of the maximum voltage applied to the discharge gap. The above results confirm the assumption that the runaway electron beam is formed, on reaching the critical field strength, in the region between the moving plasma boundary and the anode [2].

Conclusion. Thus, we have studied the runaway electron beam formation in an air-filled diode at atmospheric pressure and low average values of the E/p ratio. The results of the measurements performed with a subnanosecond time resolution showed that the electron beam appears on the leading front of the voltage pulse (at a small delay of ~0.5 ns) and has a small width (FWHM ~ 0.3 ns). The runaway electron beam pulse terminates at a high value of the E/p ratio (several times that corresponding to the appearance of the electron beam behind the foil), which is related to leveling of the electric field strength distribution in the anode–cathode gap shunted by the plasma propagating from the cathode.

The electron beam formation in a gas at high pressures plays an important role in the pulsed breakdown of gas diodes and in the formation of pulsed volume discharges. In order to monitor this phenomenon in more detail, it would be of interest to use a detection system with even better time resolution (to tens of picoseconds) and study the runaway electron beam formation at still higher pressures (several tens of bars).

REFERENCES

1. S. B. Alekseev, V. M. Orlovskiĭ, V. F. Tarasenko, *et al.*, Pis'ma Zh. Tekh. Fiz. **29** (16), 45 (2003) [Tech. Phys. Lett. **29**, 679 (2003)].
2. S. B. Alekseev, V. M. Orlovskiĭ, and V. F. Tarasenko, Pis'ma Zh. Tekh. Fiz. **29** (10), 29 (2003) [Tech. Phys. Lett. **29**, 411 (2003)].
3. Yu. L. Korolev and G. A. Mesyats, *The Physics of Pulse Breakdown* (Nauka, Moscow, 1991).
4. L. P. Babich, T. V. Loĭko, and V. A. Tsukerman, Usp. Fiz. Nauk **160** (7), 49 (1990) [Sov. Phys. Usp. **33**, 521 (1990)].
5. M. I. Yalandin and V. G. Shpak, Prib. Tekh. Éksp., No. 3, 5 (2001).
6. F. Ya. Zagulov, A. S. Kotov, V. G. Shpak, *et al.*, Prib. Tekh. Éksp., No. 2, 146 (1989).
7. V. P. Tarakanov, *User's Manual for Code KARAT* (BRA, Springfield, 1992).

Translated by P. Pozdeev

Technical Physics Letters, Vol. 29, No. 11, 2003, pp. 882–885. Translated from Pis'ma v Zhurnal Tekhnicheskoĭ Fiziki, Vol. 29, No. 21, 2003, pp. 7–16.

A Magnetooptical Study of the Odd Crystal Field Component in a Terbium–Yttrium Aluminum Garnet

U. V. Valiev, J. B. Gruber, U. R. Rustamov, K. S. Saidov, and V. Yu. Sokolov

National University of Uzbekistan, Tashkent, Uzbekistan

Physical Department, San Jose State University, San Jose, CA 9592-0106, USA

Received March 7, 2003; in final form, May 20, 2003

Abstract—We have studied the photoluminescence spectra and the luminescence magnetic circular polarization (LMCP) spectra in the region of the 4*f*–4*f* radiative transition $^5D_4 \longrightarrow {}^7F_6$ in the rare earth Tb^{3+} ion in a $Y_3Al_5O_{12}$ garnet matrix. A comparison of the experimental and theoretically calculated LMCP spectra allowed parameters of the odd crystal field component to be determined that removes the prohibition with respect to parity from the 4*f*–4*f* transitions in Tb^{3+} ion in the garnet structure. The energy spectra and wave functions of $^5D_4$ and $^7F_6$ multiplets of Tb^{3+} ion in a crystal field with the D_2 symmetry have been calculated. © *2003 MAIK "Nauka/Interperiodica".*

The considerable interest in the optical investigations pertaining to 4*f*–4*f* transitions in rare earth (RE) ions in various compounds [1, 2] is related to their possible use as active media in visible-range lasers operating in both up-conversion [3] and traditional [4] systems of optical pumping. For most RE ions in various matrices (including paramagnetic garnets), the odd crystal field component, responsible for the admixture of excited $4f^{(n-1)}5d$ (or 5*g*, etc.) configurations to the ground state configuration $4f^{(n)}$ and for the removal of parity prohibition for some practically important 4*f*–4*f* transitions, is almost unknown (in contrast to the well-studied component responsible for the Stark splitting of multiplets in the spectra of RE ions [5, 6]). Some parameters of the odd crystal field component in garnets were calculated for Nd^{3+} ions within the framework of the charge exchange model [7] and determined for Dy^{3+} [8] and Yb^{3+} [9] from a comparison between calculated intensity distributions and experimental spectra. However, this problem has not even been formulated for Tb^{3+} ion in garnets (and in other matrices), despite the importance of such data for description of the special features of optics of the 4*f*–4*f* transitions.

We report on the first attempt to establish a quantitative relationship between the coefficients of expansion of the odd component of the crystal field potential in odd spherical harmonics (B_{tp}) and the 4*f*–4*f* transition intensities $\Xi(t, \lambda)$ [7, 9] by comparing the theoretical spectra of the magnetic circular polarization of luminescence (LMCP) calculated for Tb^{3+} ions in an $Y_3Al_5O_{12}$ garnet (YAG) to the experimental data.[1] Obvious advantages of this approach to determining the odd crystal field component parameters are relatively simple modeling and calculation of the LMCP spectra, related to a significant reduction in the number of possible optical transitions allowed by the selection rules for RE compounds in a magnetic field, in contrast to the case of their optical spectra.

The LMCP and photoluminescence (PL) spectra of a $Tb_{0.2}Y_{2.8}Al_5O_{12}$ garnet were measured along the [001] direction in the region of the radiative transition $^5D_4 \longrightarrow {}^7F_6$ (a blue fluorescence band) at ~20400 cm^{-1} with a spectral resolution of ≈2 cm^{-1}. The LMCP and PL measurements were performed at T = 90 and 78 K, respectively. The luminescence was excited and observed in the transmission mode. Unpolarized photoexcitation was produced by a mercury lamp with a UV filter. The sample was magnetized in a longitudinal (relative to the direction of light propagation) external magnetic field H = 5 kOe ($H \parallel [001]$). A change in the circular polarization of secondary emission in the applied magnetic field, as expressed by the LMCP factor $P = \dfrac{I_+ - I_-}{I_+ + I_-}$ (where $I_\pm$ are the intensities of clockwise- and counterclockwise-polarized emission components), was studied using a high-sensitivity technique based on modulation of the secondary emission using a photoelastic light modulator [10, 11]. The error of the LMCP determination was ~2–3% at the center of the emission band and increased to ~5% at the band edge.

Figure 1 shows the LMCP and PL spectra of a $Tb_{0.2}Y_{2.8}Al_5O_{12}$ garnet measured at T = 90 and 78 K, respectively. A comparison of these spectra shows that the $P(\nu)$ spectrum (ν is the wavenumber in cm^{-1}) in the

[1] It is well known that λ = 2, 4, 6 for RE ions (l = 3), while the indices of expansion with respect to spherical harmonics in the symmetry group D_2 for the odd crystal field component are t = 3, 5, 7 and p = 2, 4, 6 (for $t > p$) [8, 9].

region of PL lines *3* and *4* exhibits linear variation within the corresponding bands and crosses zero at their centers. A more complicated LMCP structure in the region of closely spaced PL lines *6* and *7* represents the superposition of sloped $P(\nu)$ dependences in this energy interval. A sharp drop in the PL line width observed when decreasing the temperature from 300 to 78 K is correlated with a significant increase in the slope of LMCP for these lines at $T = 90$ K.

The aforementioned features in the behavior of the LMCP spectra in the region of the radiative transition $P(\nu)$ are inherent in the so called diamagnetic contribution (*A* term [12]) characterized by the linear variation of the $P(\nu)$ value within an emission line (with the sign reversal at the center). The slope is proportional to the "effective" Zeeman splitting ΔE_Z^{eff} of the degenerate (doublet [12]) or quasidegenerate (quasidoublet [13]) states combined in the $4f$–$4f$ radiative transition.[2] When the line width decreases, the slope grows in proportion to $1/\Gamma^2$, where 2Γ is the line width determined for $I = \frac{I_0}{2.72}$ (I_0 being the line intensity at the center) [12].

Taking a doubled product of the LMCP slope for line *7* and squared halfwidth (Γ^2) determined from the experimental data at $T = 90$ K (Fig. 1), we determine the effective Zeeman splitting $\Delta E_Z^{\text{eff}} = 1.48$ cm^{-1} ($H = 5$ kOe) of the quantum states of $^5D_4$ and $^7F_6$ multiplets of Tb^{3+} ion in the garnet, which are responsible for the *A* term of LMCP on this line ($2\Gamma \cong 9.5$ cm^{-1}).

For interpreting the results of the magnetooptical and optical study of the radiative transition $^5D_4 \longrightarrow {}^7F_6$, we have numerically calculated the wave functions and energies of the Stark sublevels of $^5D_4$ and $^7F_6$ multiplets of Tb^{3+} ion occurring in one of the nonequivalent positions in the crystal structure of YAG with the symmetry group D_2. The calculation was performed using the complete crystal field Hamiltonian

$$\hat{H}_{\text{CF}} = \sum_{k,q} B_{kq}(C_k^q + C_k^{-q}) + g_0\mu_B\mathbf{HJ}, \qquad (1)$$

where B_{kq} are the crystal field parameters (nine of which are nonzero for the D_2 symmetry: $k = 2, 4, 6$; $q = 0, 2, 4, 6$); C_k^q are irreducible tensor operators [15]; μ_B is the Bohr magneton; $g_0 = 1.5$ is the Lande factor for $^5D_4$ and $^7F_6$ multiplets; and **J** is the angular momentum operator.

The calculated Stark energy sublevels of multiplets and the corresponding wavefunctions (written in the simple $|J, M_J\rangle$ basis) were classified with respect to symmetry using irreducible representations Γ_i ($i = 1, 2, 3, 4$) of the D_2 symmetry group [6, 14] (orientation of the crystal field symmetry axes was analogous to that adopted in [13, 15]). The initial data for the numerical calculations were represented by a set of crystal field parameters B_{kq} [5, 6] and the results of optical investigations of terbium yttrium garnets [15].

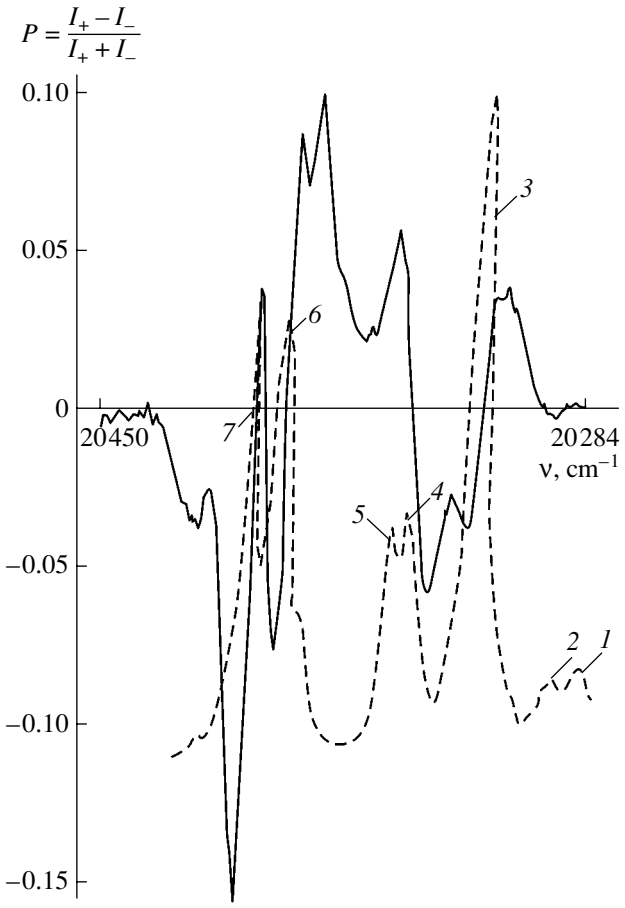

Fig. 1. LMCP spectrum (solid curve) for the radiative transition $^5D_4 \longrightarrow {}^7F_6$ in $Tb_{0.2}Y_{2.8}Al_5O_{12}$ garnet measured at $T = 90$ K in a magnetic field of $H = 5$ kOe parallel to [001] axis. Dashed curve shows the PL spectrum of Tb^{3+} in the same garnet measured at $T = 78$ K.

Reliable assignment of the observed *A* type features in the LMCP spectra (Fig. 1) to the radiative transitions between Stark sublevels of the excited $^5D_4$ and ground $^7F_6$ multiplets of the $4f^{(9)}$ configuration of Tb^{3+} ion in YAG (Fig. 2) can be performed by considering the symmetry selection rules for the components of the dipole moment of optical transitions determining the magnitude (and sign) of the *A* term of LMCP. Indeed, the "diamagnetic" contribution to the LMCP of a non-Kramers RE ion (or the *A* term) is related to the appearance of allowed (in the electric dipole approximation)

[2] The "effective" Zeeman splitting of a doublet (or quasidoublet) is determined by a product of the magnetic moment μ_g and the applied field strength *H* [14].

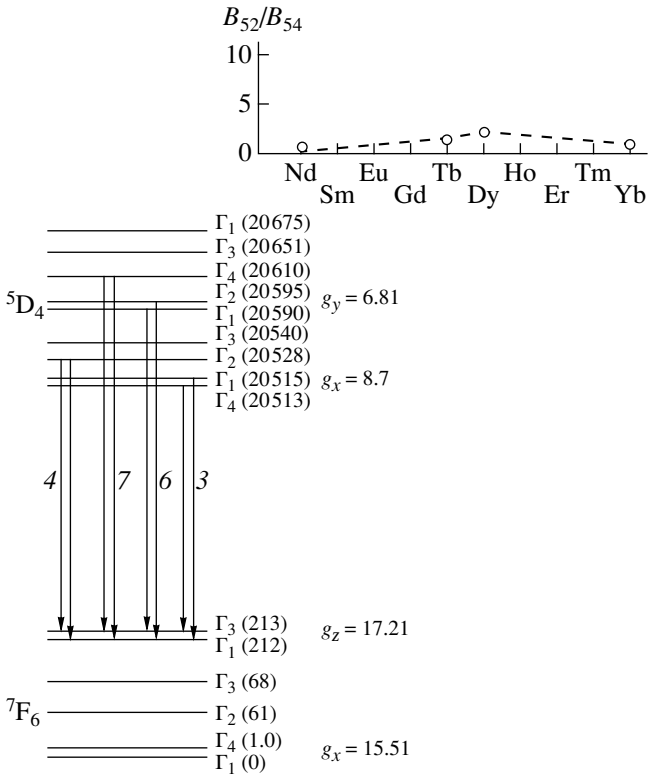

Fig. 2. A scheme of the radiative transitions of the "singlet (quasidoublet)–quasidoublet" type contributing to the LMCP spectrum of a paramagnetic $Tb_{0.2}Y_{2.8}Al_5O_{12}$ garnet measured on the radiative transition $^5D_4 \longrightarrow {}^7F_6$. Vertical arrows indicate allowed radiative transitions; g_x, g_y, g_z are the calculated components of the *g* tensor of quasidoublet relative to the local system of coordinates of a RE ion in the YAG structure. The energies of the Stark sublevels (in cm^{-1}) are measured from the lowest (ground) state in the $^7F_6$ multiplet. The inset shows a plot of the ratio of the odd crystal field coefficients B_{52}/B_{54} versus the RE ion position in the lanthanide series, constructed using our results and data from [7–9].

radiative transitions of the "isolated singlet–quasidoublet" type, which can be expressed as [13]

$$P^A = \frac{1}{2}\mu_B H \frac{(\nu - \nu_0)}{\Gamma^2}\left(\frac{A'}{D_2}\right) \qquad (2)$$

in the approximation of a Gaussian emission contour

$$I = I_0 \exp\left(\frac{\nu - \nu_0}{\Gamma}\right)^2.$$

The A'/D_2 ratio determining the magnitude and sign of the *A* term of LMCP depends on the magnetic moment μ_g of the quasidoublet. At the same time, this ratio is proportional to the product of matrix elements of the radiative transitions of the "isolated singlet–quasidoublet" type: electric-dipole elements for the transitions from Stark singlet to quasidoublet states and magnetic-dipole elements for the transitions between quasidoublet states mixed by the external field *H*.[3] Using the known symmetry selection rules [13, 15] and the energies of the Stark sublevels of $^5D_4$ and $^4F_6$ multiplets calculated in this study, we obtain a scheme of radiative 4*f*–4*f* transitions responsible for the features observed in the LMCP spectrum of the $Tb_{0.2}Y_{2.8}Al_5O_{12}$ garnet in the energy interval studied (Fig. 2).

It is important to note that modeling of the LMCP spectra must include, besides taking into account the selection rules, summing of the contributions from RE ions occurring in various nonequivalent positions (*c*-sites) in the RE sublattice of the garnet on the passage from a local to crystal coordinate system. In our case, the *y* and *z* axes of the local coordinate system of the RE ion coincide with crystallographic directions of the [110] type, while the *x* axis is parallel to directions of the [100] type in the garnet crystal [13, 15]. In a crystal magnetized along the [001] axis, the acting (i.e., splitting) magnetic fields in the quasidoublets characterized by g_x, g_y, and g_z components of the *g* tensor (describing anisotropy of the Zeeman splitting in RE garnets [14]) are $H^X_{act} = H$, $H^{Y,Z}_{act} = H/\sqrt{2}$.

According to the results of numerical calculations, the effective Zeeman splitting of the $^7F_6(\Gamma_1, \Gamma_3)$ quasidoublet at 212 cm^{-1}, equal to $\Delta E_Z^{eff} = 1.43$ cm^{-1} in a field of $H = 5$ kOe ($H \parallel [001]$), is determined by the Ising mechanism (sharply anisotropic [14]) of magnetization of the RE ion with a magnetic moment of $\mu_g = (1/2)g_z\mu_B$ ($g_z = 17, 21$; $g_x, g_y \le 0.5$) oriented along the *z* axis of the local system of coordinates at the *c*-site. It should be noted that the Ising-like behavior of the *g* tensor in the given state is related to a considerable extent to the fact that the wave functions of the quasidoublet can be described with a good approximation by the "pure" $|J, M_J\rangle$ states: $|\Gamma_1\rangle = -0.672(|6, +6\rangle + |6, -6\rangle) + 0.129(|6, +4\rangle + |6, -4\rangle) + 0.083(|6, +2\rangle + |6, -2\rangle)$ and $|\Gamma_3\rangle = 0.696(|6, +6\rangle - |6, -6\rangle) - 0.076(|6, +4\rangle - |6, -4\rangle) - 0.0.38(|6, +2\rangle - |6, -2\rangle)$. A good conformity between theoretical and experimental values of ΔE_Z^{eff} for the $^7F_6(\Gamma_1, \Gamma_3)$ quasidoublet confirms correct assignment of the LMCP features on line *7* to the radiative transition $^5D_4(\Gamma_4) \longrightarrow {}^7F_6(\Gamma_1, \Gamma_3)$.

At the same time, direct calculation of the A'/D_2 ratio performed for the same transition by applying a

[3] According to [13],

$$A'/D_2 \sim 2\mathrm{Im}\{\langle j|\hat{\mu}_z|k\rangle\langle a|\hat{P}_x|j\rangle\langle k|\hat{P}_y|a\rangle\}, \qquad (3)$$

where $\hat{\mu}_z$ is the operator of the *z*-projection of the magnetic moment of a quasidoublet of the RE ion; $\hat{P}_x$ and $\hat{P}_y$ are the components of the dipole moment operator of the ion; $|j\rangle$, $|k\rangle$ are the wave functions of the Stark singlets forming a quasidoublet in the $^7F_6$ multiplet; and $|a\rangle$ is the wave function of the Stark singlet of the excited $^5D_4$ multiplet.

theoretical approach developed in [13] (based on the Jadd–Ofelt theory) to the wave function calculated in our study for the Stark singlet $^5D_4(\Gamma_4)$ ($|\Gamma_4\rangle$ = $0.637(|4, +1\rangle + |4, -1\rangle) - 0.302(|4, +3\rangle + |4, -3\rangle)$) showed that agreement with the experiment can be obtained provided that the parameters of the odd crystal field component obey the following relations: $B_{32}\Xi(3, 4)/B_{52}\Xi(5.6) = -1.26$ and $B_{54}/B_{52} = 0.852$. The matrix elements of the $4f$–$4f$ transitions entering into the expression for A'/D_2 (see formula (3)) were calculated taking into account a dominating contribution due the Jadd mechanism, whereby the odd crystal field components produce admixing of the states of the excited $4f^{n-1}5d$ ($l' = 2$) configuration to the states of the ground $4f^n$ ($l = 3$) configuration of the Tb^{3+} ion after removal of the parity prohibition from the $4f$–$4f$ transitions in the first order of the perturbation theory (see [16]).[4]

The obtained relations between the parameters of the odd crystal field component in $Tb_{0.2}Y_{2.8}Al_5O_{12}$ garnet allow us to explain the distribution of intensities observed for the emission lines *3* and *7* at $T = 78$ K. The calculation of the square matrix elements for the transitions $^5D_4(\Gamma_1, \Gamma_4) \longrightarrow {}^7F_6(\Gamma_1, \Gamma_3)$ and $^5D_4(\Gamma_4) \longrightarrow {}^7F_6(\Gamma_1, \Gamma_3)$ for lines *3* and *7*, respectively, using the wave function calculated in our study for the quasidoublet $^5D_4(\Gamma_1, \Gamma_4)$ ($|\Gamma_4\rangle = -0.643(|4, +3\rangle + |4, -3\rangle) - 0.305(|4, +1\rangle + |4, -1\rangle)$ and $|\Gamma_1\rangle = 0.095(|4, +4\rangle + |4, -4\rangle) + 0.696(|4, +2\rangle + |4, -2\rangle) + 0.114|0\rangle$) showed that their ratio at $T = 78$ K is 4.1. The experimental ratio of the oscillator strength (or areas) of the emission lines *3* and *7* at the same temperature is close to 5.

Thus, the ratios of the parameters of the odd crystal field component provide for a consistent explanation of the features of optical and magnetooptical spectra of Tb^{3+} ion in YAG and confirm a certain regularity in behavior in the sequence of RE elements. Indeed, a plot of the ratio of the odd crystal field coefficients B_{52}/B_{54} versus the ion position in the lanthanide series (involving data from [7–9]) shows that the ratio exhibits a maximum at the center of the lanthanide series (Fig. 2). Therefore, the fact that the orthorhombic component of the crystal potential B_{52} dominates over the cubic component B_{54} for Tb^{3+} and Dy^{3+} ions explains the Ising-like behavior of these ions (in contrast to the behavior of Nd^{3+} and Yb^{3+}) in the YAG matrix.

The above data can be used for calculating the relative intensities of the Stark components of the emission bands related to the radiative transitions $^5D_4 \longrightarrow {}^7F_J$ ($J = 6, 5$), which are of special interest for the development of up-conversion lasers on terbium–yttrium aluminum garnets.

[4] The spin prohibition of the transition $^5D_4 \longrightarrow {}^7F_6$ is removed in the second-order theory by the spin–orbit coupling mixing $^5D_4$ multiplet with the states of the ^7D term of the excited configuration $4f^{(n-1)}5d$ of Tb^{3+} ion [14, 16].

REFERENCES

1. P. Le Booulanger, J.-L. Doualan, S. Girard, *et al.*, Phys. Rev. B **60**, 11380 (1999).
2. I. S. Edel'man, A. V. Malakhovskiĭ, A. M. Potseluĭko, *et al.*, Fiz. Tverd. Tela (St. Petersburg) **43**, 1004 (2001) [Phys. Solid State **43**, 1037 (2001)].
3. R. Brede, E. Heumann, J. Koetke, *et al.*, Appl. Phys. Lett. **63**, 2030 (1993).
4. M. Sekita, Y. Miyazawa, S. Morita, *et al.*, Appl. Phys. Lett. **65**, 2380 (1994).
5. C. A. Morrison and R. P. Leavitt, *Handbook on the Physics and Chemistry of Rare-Earth* (North-Holland, Amsterdam, 1982), Vol. 5, pp. 461–692.
6. J. B. Gruber, M. E. Hills, R. M. Macfarlane, *et al.*, Phys. Rev. B **40**, 9464 (1989).
7. A. A. Kaminskiĭ, B. Z. Malkin, and L. L. Bumagina, Izv. Akad. Nauk SSSR, Ser. Fiz. **46**, 979 (1982).
8. S. Washimiya, J. Phys. Soc. Jpn. **27**, 56 (1969).
9. N. P. Kolmakova, S. V. Koptsik, G. S. Krinchik, *et al.*, Fiz. Tverd. Tela (Leningrad) **33**, 2674 (1991) [Sov. Phys. Solid State **33**, 1510 (1991)].
10. F. S. Richardson and J. P. Reihl, Chem. Rev. **77**, 773 (1977).
11. U. V. Valiev, T. Asilov, and R. A. Salyukov, Prib. Tekh. Éksp., No. 8, 87 (1994).
12. V. S. Zapasskiĭ and P. P. Feofilov, Usp. Fiz. Nauk **116**, 41 (1975) [Sov. Phys. Usp. **18**, 323 (1975)].
13. U. V. Valiev, V. Nekvasil, Sh. I. Mukhamedhanova, *et al.*, Phys. Status Solidi B **213**, 493 (1999).
14. A. K. Zvezdin, V. M. Matveev, A. A. Mukhin, and A. I. Popov, *Rare-Earth Ions in Magnetic-Ordered Crystals* (Nauka, Moscow, 1985).
15. R. Baurer, J. Heber, and D. Mateika, Z. Phys. B: Condens. Matter **64**, 201 (1986).
16. U. V. Valiev, A. A. Klochkov, and A. S. Moskvin, Fiz. Tverd. Tela (Leningrad) **34**, 406 (1992) [Sov. Phys. Solid State **34**, 218 (1992)]; B. R. Judd, Phys. Rev. **127**, 750 (1962).

Translated by P. Pozdeev

Technical Physics Letters, Vol. 29, No. 11, 2003, pp. 886–888. Translated from Pis'ma v Zhurnal Tekhnicheskoĭ Fiziki, Vol. 29, No. 21, 2003, pp. 17–21.

Semiconductor Converters of Continuous Laser Radiation into a Pulsed Beam

P. G. Kasherininov, A. N. Lodygin, and I. S. Tarasov

Ioffe Physicotechnical Institute, Russian Academy of Sciences, St. Petersburg, Russia

Received May 22, 2003

Abstract—We consider the possibility of creating a semiconductor device converting continuous laser radiation into a sequence of pulses in the visible and infrared wavelength range. *© 2003 MAIK "Nauka/Interperiodica".*

We propose a semiconductor device capable of converting continuous laser radiation into a sequence of pulses in the visible and IR range. The converter comprises a metal–gaseous dielectric–insulating electrooptical semiconductor crystal structure [1] placed between crossed polarizers. The structure, biased with a dc voltage V_0, is illuminated with a thin continuous beam of light partly absorbed in the crystal. The light is incident parallel to the electric field direction in the structure. At the converter output, we obtain a sequence of light pulses at a repetition rate determined by the incident light intensity. It was demonstrated [2] that the voltage V_0 applied to the structure is divided between the insulating electrooptical crystal and the gaseous

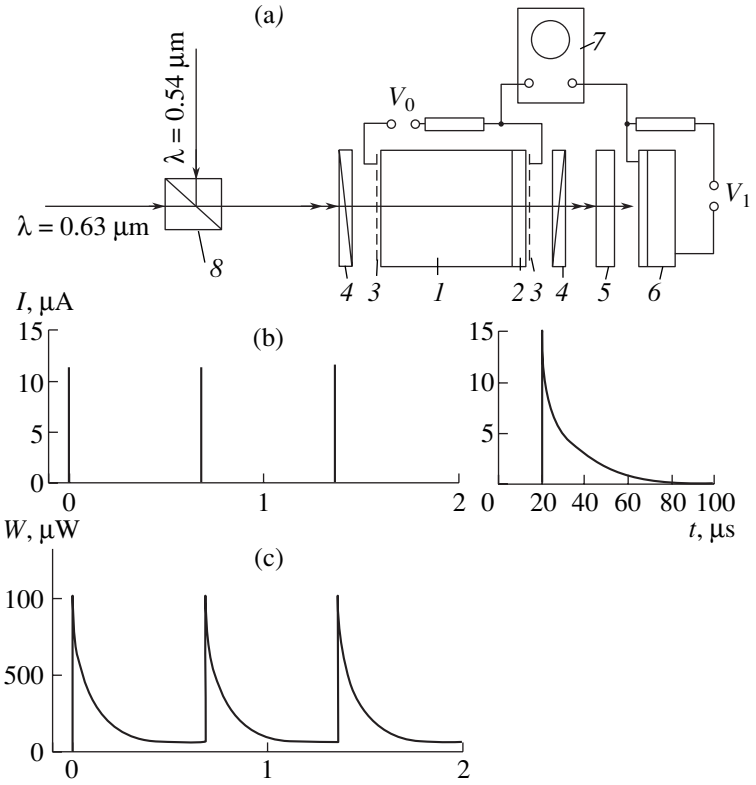

Fig. 1. (a) A schematic diagram illustrating experiments with an optical pulse converter based on a metal–gaseous dielectric–semiconductor structure: (*1*) insulating electrooptical bismuth silicate crystal (d = 0.15 cm); (*2*) gaseous dielectric layer ($d_0 = 10^{-2}$ cm); (*3*) transparent electrodes; (*4*) crossed polarizers; (5) optical filter blocking radiation with λ = 0.54 μm; (*6*) photodetector; (*7*) double-beam oscillograph; (*8*) prism. (b) Discharge current pulses measured in the external circuit of the converter structure illuminated only by the light with λ = 0.63 μm ($W_0 = 9 \times 10^{-4}$ W). (c) Optical pulses measured at the output of the converter under the same conditions. Bias voltage V_0 = 1100 V.

1063-7850/03/2911-0886$24.00 © 2003 MAIK "Nauka/Interperiodica"

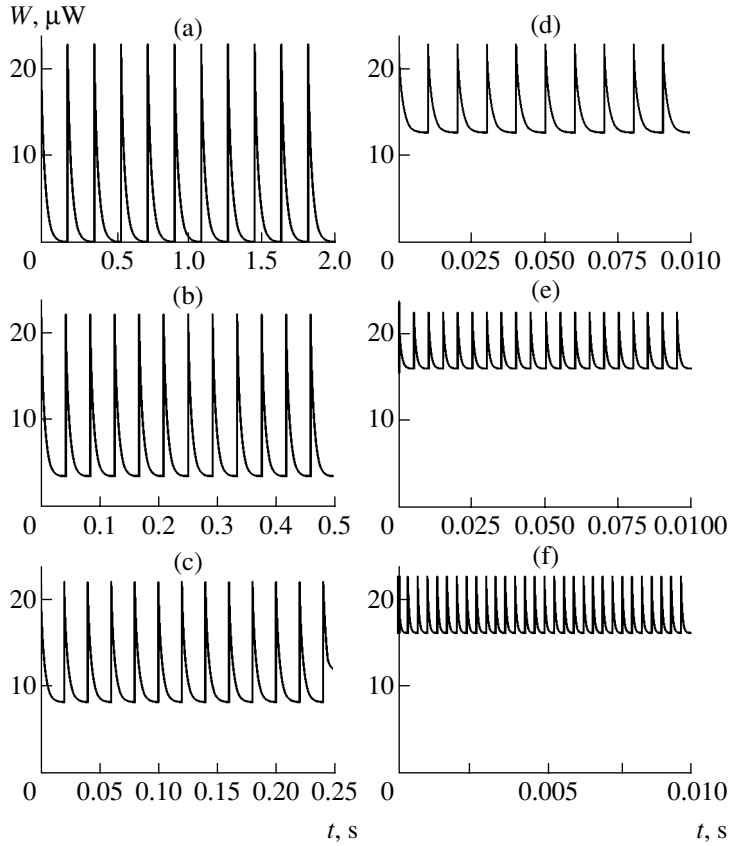

Fig. 2. Optical pulses observed at the output of the bismuth silicate crystal converter simultaneously illuminated by two continuous thin light beams with $\lambda = 0.63$ μm and 0.54 μm. The power of the radiation with $\lambda = 0.54$ μm is varied (mW): (a) 0; (b) 0.05; (c) 0.12; (d) 0.2; (e) 0.4; (f) 2.0. The light beam with $\lambda = 0.63$ μm has a constant power of $W_0 = 0.9$ mW. The structure is biased to $V_0 = 1500$ V.

dielectric layer according to their capacitances. The value of V_0 is selected so that the electric field strength in the gas is somewhat lower than the critical value for the gas discharge (E_{cr}).

The light beam passing through the structure is absorbed in the electrooptical crystal and, as a result, an electric charge is accumulated at the crystal–gas interface. This charging leads to a redistribution of the applied voltage between the crystal and the dielectric gap: as the charge is accumulated, the electric field strength in the gap increases and reaches a critical level (E_{cr}). Then, the conductivity of the gaseous dielectric layer increases by many orders of magnitude and the accumulated charge leaks from the structure. Upon discharge, the electric field strength in the structure restores its initial distribution and the cyclic process is repeated [1–4].

When the structure is irradiated with a thin light beam (with a diameter $d < 5 \times 10^{-2}$ cm), the cyclic redistribution of the electric field strength takes place immediately under the illuminated spot on the surface. As a result, the intensity of the light flux transmitted through the crystal is modulated due to the longitudinal Pockels effect. The output light flux represents a sequence of pulses following one another at a repetition rate determined by the incident flux intensity. If such a converter is illuminated by two collimated beams, one of which (e.g., the infrared) is not absorbed in the electrooptical crystal, the output infrared radiation flux will also be pulsed at a frequency determined by the intensity of the absorbed light beam.

Figure 1a shows a schematic diagram of the converter based on a bismuth silicate crystal illuminated by two continuous, coinciding thin light beams (with $d < 5 \times 10^{-2}$ cm) representing a weakly absorbed radiation with $\lambda = 0.63$ μm and a strongly absorbed radiation with $\lambda = 0.54$ μm, both beams being parallel to the electric field direction.

Figure 1b presents the magnitude and shape of the discharge current pulses measured in the external circuit of the structure illuminated only by the light with $\lambda = 0.63$ μm ($W_0 = 9 \times 10^{-4}$ W). Figure 1c shows the magnitude and shape of the optical pulses measured at the converter output by a photodetector and displayed by a double-beam oscillograph.

As can be seen by comparing Figs. 1b and 1c, the leading fronts of these pulses coincide in time, while the duration of the discharge current pulses (Fig. 1b) is significantly shorter than that of the optical pulses (Fig. 1c). This is explained by the fact that the duration

of the current pulses (appearing when the electric field strength in the gaseous dielectric layer reaches the critical level E_{cr}) is determined by the time of charge leakage from the crystal during the gas discharge. In contrast, the optical pulse duration is determined by the time of electric charge accumulation in the crystal up to a critical level.

Figure 2 shows the pattern of optical pulses observed at the output of the converter simultaneously illuminated by two continuous, coinciding thin light beams with $\lambda = 0.63$ μm and 0.54 μm. At a constant power of the former radiation ($\lambda = 0.63$ μm, $W_0 = 0.9$ mW, $V_0 = 1500$ V), the frequency of optical pulses with $\lambda = 0.63$ μm at the converter output is determined by the power of light flux with $\lambda = 0.54$ μm. As the power of the latter flux ($\lambda = 0.54$ μm) is controlled within $W_0 = 0$–2 mW, the repetition rate of the pulses with $\lambda = 0.63$ μm varies within $f = 6$–300 Hz. The modulation depth decreases with increasing repetition rate, which is related to the delayed charge leakage upon gas discharge. For the constant parameters of light beams, the repetition rate of the optical pulses increases with the voltage V_0 applied to the structure. Using this modulator, it is possible to convert high-power fluxes of continuous IR radiation (not absorbed in the converter) into pulsed IR radiation by using a low-power beam of continuous radiation that is absorbed in the electrooptical crystal.

REFERENCES

1. P. G. Kasherininov and A. N. Lodygin, Pis'ma Zh. Tekh. Fiz. **23** (4), 23 (1997) [Tech. Phys. Lett. **23**, 137 (1997)].
2. P. G. Kasherininov and A. N. Lodygin, Pis'ma Zh. Tekh. Fiz. **24** (22), 64 (1998) [Tech. Phys. Lett. **24**, 893 (1998)].
3. P. G. Kasherininov and A. N. Lodygin, Fiz. Tekh. Poluprovodn. (St. Petersburg) **33**, 1475 (1999) [Semiconductors **33**, 1328 (1999)].
4. A. D. Bondarev, P. G. Kasherininov, A. N. Lodygin, *et al.*, Pis'ma Zh. Tekh. Fiz. **26** (3), 67 (2000) [Tech. Phys. Lett. **26**, 122 (2000)].

Translated by P. Pozdeev

Technical Physics Letters, Vol. 29, No. 11, 2003, pp. 889–891. Translated from Pis'ma v Zhurnal Tekhnicheskoĭ Fiziki, Vol. 29, No. 21, 2003, pp. 22–26.

Mechanochemical Modification of the Phase Diagrams of Hexagonal Oxide Ferrimagnets

E. P. Naĭden, V. I. Itin, and O. G. Terekhova

Siberian Institute of Physics and Technology, Tomsk State University, Tomsk, Russia
Structural Macrokinetics Department, Tomsk Scientific Center, Siberian Division, Russian Academy of Sciences, Tomsk, Russia
e-mail: naiden@elefot.tsu.ru; maks@fisman.tomsk.ru

Received May 15, 2003

Abstract—Mechanical activation and fine comminution of hexagonal oxide ferrimagnets by milling to a nanocrystalline state (ultradisperse powder), followed by sintering, leads to significant changes in the phase diagram, the temperature of synthesis, and the magnetic properties as compared to those of the materials obtained by traditional ceramic technology. The final material structure is formed through "chemical assembly"—sequential consolidation of nanodimensional particles (structure-forming blocks)—rather than through the formation of low-temperature phases and their decomposition with increasing temperature. © *2003 MAIK "Nauka/Interperiodica".*

When a solid is comminuted so that the dimensions of structural elements are reduced to a level on the order of tens of nanometers, the solid passes to a special state called nanocrystalline, with both structure and properties differing from those in the usual macroscopic state of the same material. Since the dimensions of structural elements in this state becomes comparable with the basic geometric characteristics of substances and the characteristic spatial parameters of physical processes (the dimensions of electrical and magnetic domains, electron mean free path, etc.), some quantum-mechanical effects are manifested that significantly change the atomic structure and modify the physical properties of the material.

An effective method for converting solids into the nanocrystalline state is offered by fine comminution (ultradispersion) and mechanical activation of solids in high-energy-density devices such as planetary ball mills. Using this method, it is possible to finely disperse a crystalline substance so as to obtain substructural blocks in the form of nanodimensional particles. We suggest that, by changing external conditions, it is possible to build structures of various types from these blocks by means of "chemical assembly," a process not requiring overcoming high potential barriers (or rupture of strong chemical bonds) encountered in the nucleation of new phases [1]. The synthesis through chemical assembly must be especially clearly manifested in the synthesis of polytype materials differing only by the sequence of structure-forming blocks. Examples of such materials are offered by hexagonal oxide ferrimagnets (hexaferrites) with the structural types and crystal structures presented in the table.

This work was aimed at studying the effect of fine dispersion and mechanical activation on the character of phase diagrams of hexaferrites (I) $BaCo_{0.7}Zn_{1.3}Fe_{16}O_{27}$ (CoZn–W) and (II) $Ba_4Co_2Fe_{36}O_{60}$ (Co_2–U) which can be used as electromagnetic radiation absorbers.

Hexaferrites I and II belong to the class of compounds in which the composition is determined by the phase diagram of the ternary system MeO–BaO–Fe_2O_3. This system features the formation of a series of poly-

Compositions and structures of hexaferrites

Chemical composition	Structural type	Crystal structure	*C*, nm
$BaO \cdot 6Fe_2O_3$	M	RSR'S'	2.32
$BaO \cdot 2MeO \cdot 8Fe_2O_3$	W(MS)	RSSR'S'S'	3.28
$2BaO \cdot 2MeO \cdot 6Fe_2O_3$	Y	TST'S'T"S"	4.35
$3BaO \cdot 2MeO \cdot 12Fe_2O_3$	Z(MY)	RSTSR'S'T'S'	5.23
$2BaO \cdot 2MeO \cdot 14Fe_2O_3$	X(MMS)	RSR'S'S'RSR'S'S'RSR'S'S'	8.43
$4BaO \cdot 2MeO \cdot 18Fe_2O_3$	U(MMY)	(RSR'S'T'S')	11.43

1063-7850/03/2911-0889$24.00 © 2003 MAIK "Nauka/Interperiodica"

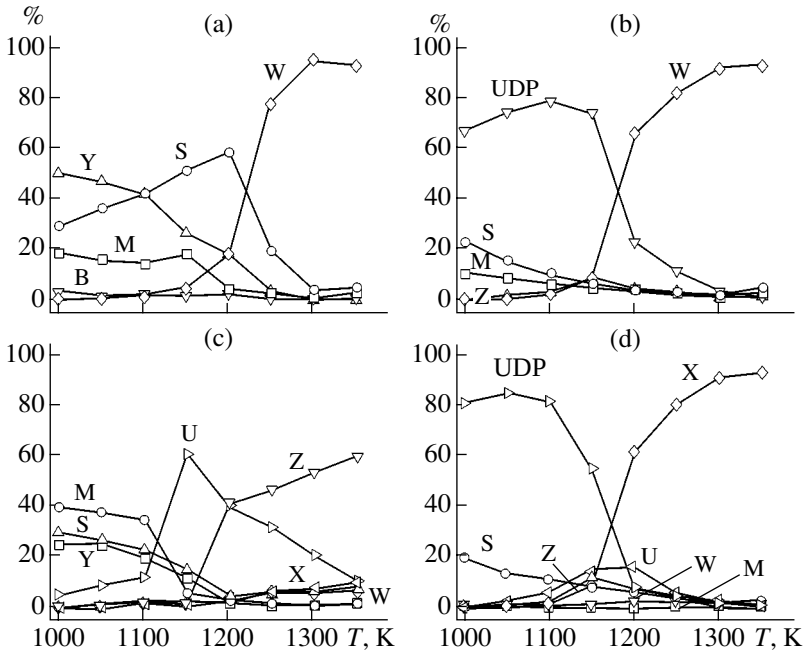

Temperature variation of the phase composition of hexaferrites (a, b) $BaCo_{0.7}Zn_{1.3}Fe_{16}O_{27}$ (CoZn–W) and (c, d) $Ba_4Co_2Fe_{36}O_{60}$ (Co_2–U) synthesized (a, c) according to the traditional ceramic technology and (b, d) after ultradispersion and mechanical activation.

type ternary oxides with the crystal structures representing various combinations of three blocks—the spinel block S (comprising two layers of anions) and two hexagonal blocks, R and T (comprising three and four layers, respectively, of hexagonal close-packed anions partly replaced with large divalent barium cations) (see table).

A special feature of this class of ferrimagnetic materials is the perfect cleavage at the basal planes of crystals grains, whereby individual particles of a powdered material have the shape of a flat hexagonal prism with lateral dimensions significantly exceeding the thickness. As a result, the role of a structurally inhomogeneous surface and a near-surface layer in such a material after fine dispersion and mechanical activation significantly increases in comparison to the role of the volume. This must lead to a considerable change in magnetic properties, primarily in the effective magnetic anisotropy.

The phase composition of the synthesized oxide ferrimagnets was determined by X-ray diffraction using FeK_α radiation. The magnetic properties were studied using an automated complex for measuring characteristics in a pulsed magnetic field. The measurements were performed with the field strength varying from 0.01 to 10 T in the range of temperatures from 80 to 600°C [2].

In the initial state after preliminary sintering for 6 h at 1100°C, ferrite I comprises a mixture of phases W, M, and about 20 vol % of the sum of phase S and barium orthoferrite ($BaFe_3O_4$), while ferrite II consists of phases Y (25 vol %), M (40 vol %), S (30 vol %), and the nuclei of phase U (<5 vol %).

Ultradispersion and mechanical activation of the preliminarily sintered hexaferrites with the compositions indicated above were performed in a planetary ball mill. The weight ratio of balls to powder was 20 : 1 and the processing duration was 20 min. This treatment resulted in the formation of an ultradisperse powder (UDP) consisting of clusters with the characteristic average size of about 0.85 and 0.55 nm.

Figure 1 compares the phase diagrams of hexaferrites with the W and U structures synthesized according to the traditional ceramic technology and using the UDP obtained by ultradispersion and mechanical activation upon preliminary sintering. In contrast to ferrite I with the W structure obtained by sintering at 1320°C after 1-h mixing in a vibration mill (Fig. 1a), the W structure of this ferrite in the latter case forms predominantly from nanodimensional clusters of the UDP (Fig. 1b). In this case, the optimum synthesis temperature is 100–120°C lower than that according to the traditional ceramic technology.

In ferrite II synthesized by the traditional ceramic technology, the U type structure is stable within a rather narrow temperature interval (1150 ± 15°C) and decomposes on further heating with the formation of Z and X phases (Fig. 1c). After mechanical activation and comminution into the UDP state, the main phase formed from ferrite II under the same conditions is a high-temperature phase of the X type not containing hexagonal T blocks (Fig. 1d). Thus, the ultimate dispersion and

mechanical activation significantly reduce the sintering temperature and allow the process of phase formation in hexaferrites to be controlled.

It should be noted that phases with the structure W for ferrite I and U for ferrite II obtained by the traditional technology usually appear through the formation of low-temperature phases and their subsequent decomposition on heating (see Figs. 1a and 1c) [3]. According to the idea of academician Kabanov [4], converting the ferrites into a UDP state consisting of nanodimensional clusters "allows nanoparticles to participate in the thermal motion and provides for the possibility of their self-assembly into superstructures by eventually finding the thermodynamic optimum."

The process of mechanical activation and ultradispersion also significantly modifies the magnetic characteristics of hexaferrites. In particular, the saturation magnetization somewhat lowers, the region of spin-orientational phase transformations smears, and the magnetic anisotropy field in the easy axis state decreases [5].

In conclusion, we have demonstrated for the first time that ultradispersion and mechanical activation of hexagonal oxide ferrimagnets by milling to a nanocrystalline state leads, in the course of subsequent sintering, to significant changes in the phase diagram, the temperature of synthesis, and the magnetic properties as compared to those of the materials obtained by traditional ceramic technology. This opens new possibilities for the creation of novel radioabsorbing materials with desired magnetic properties.

REFERENCES

1. V. B. Aleskovskiĭ, *Stoichiometry and Synthesis of Solids* (Nauka, Moscow, 1976).
2. V. Yu. Kreslin and E. P. Naĭden, Prib. Tekh. Éksp., No. 1, 63 (2002).
3. E. P. Naĭden, Doctoral Dissertation (Tomsk, 1991).
4. I. V. Melikhov, Vest. Ross. Akad. Nauk, No. 10, 907 (2002).
5. E. P. Naĭden, V. I. Itin, O. N. Terekhova, *et al.*, Khim. Interesakh Ustoichivogo Razvitiya, No. 10, 205 (2002).

Translated by P. Pozdeev

Technical Physics Letters, Vol. 29, No. 11, 2003, pp. 892–893. Translated from Pis'ma v Zhurnal Tekhnicheskoĭ Fiziki, Vol. 29, No. 21, 2003, pp. 27–31.

Electrooptical Behavior of Twist Nematic Liquid Crystal Layers in the Regime of Electroconvection: The Role of Defects

G. R. Yakupova and O. A. Skaldin*

Institute of Molecular and Crystal Physics, Russian Academy of Sciences, Ufa, Bashkortostan, Russia

** e-mail: scala@anrb.ru*

Received May 20, 2003

Abstract—We have studied the sequence of orientational phase transitions in twist nematic liquid crystal layers in the regime of electroconvection with allowance of the nucleation of structural defects influencing these transformations. Quantitative characteristics determining the degree of defectness of the modulated structures are established. © *2003 MAIK "Nauka/Interperiodica".*

Investigations of the behavior of defects in liquid crystals (LCs) are mostly restricted to the cases of planar orientation of the LC director **n** [1, 2]. From the standpoint of practical applications, LC systems featuring twist (or supertwist) orientation of the director are much more promising. For example, the slope and contrast of the electrooptical curve in twist nematic liquid crystals (NLCs) significantly depend on the twist angle, reaching maximum values at 90° [3]. Of course, it would be very interesting for both basic science and practical applications to study the modulated NLC structures free of defects. However, real ordered systems are by no means as ideal, which is related to defects that are always present in the roll structures and influence the electrooptical characteristics of NLC layers.

In this context, we have studied the transition from one-dimensional (1D) to 2D domain structure in a $\pi/2$ twist NLC during electroconvection in an alternating electric field and determined the quantitative characteristics reflecting the degree of defectness of the periodic structures under consideration. The influence of defects in the domain structure on the above transitions has been studied and analyzed.

The investigation was performed for a model NLC system based on 4-π-methoxybenzilidene-*n*-butylaniline (MBBA). The MBBA film was placed between glass plates bearing transparent SnO_2 electrodes. The plates were preliminarily rubbed in one direction (in order to induce a homogeneous planar orientation of the NLC director) and then rotated relative to each other by $\pi/2$ to produce a $\pi/2$ twist configuration of the director field. The NLC layer thickness was $d = 20$ μm and the linear cell dimensions were 16×12 mm. The cell was biased by an ac voltage with an amplitude U and a frequency of $f = 30$ Hz. The thresholds of the domain structure formation, the types of defects, and the spatial and temporal characteristics of these defects were determined by optical diffraction and by direct analysis of the video images obtained in a polarization microscope.

As the amplitude of the applied alternating electric field strength in the twist NLC increases above a threshold level (the corresponding critical voltage being U_c = 5.6 V), the sample exhibits the following sequence of structural transformations (Fig. 1): linear (1D) domains (Williams' domains) ⟶ modulated rolls ⟶ 2D domain structure (in the NLC layer plane) ⟶ turbulent regime (dynamical light scattering mode). The linear domains in twist NLCs are aligned perpendicularly to the director orientation in the middle of the unperturbed layer. When the voltage is increased so that $\varepsilon = (U - U_c)/U_c = 1.8$ (Fig. 1), the system becomes modulated along the axis of rolls. The amplitude of the deformation of rolls increases with the voltage unless a 2D

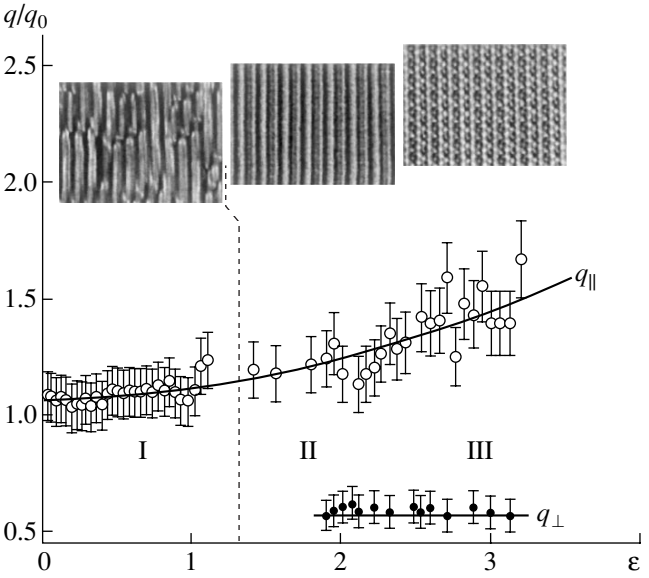

Fig. 1. A plot of the reduced wave vectors versus control parameter ε ($q_0 = 2\pi/d$, d is the NLC layer thickness). The insets show the characteristic patterns of wave instabilities in the corresponding ε regions: (I) linear domains; (II) transition state; (III) 2D grid pattern.

1063-7850/03/2911-0892$24.00 © 2003 MAIK "Nauka/Interperiodica"

grid pattern is formed in the *X*0*Y* plane [4]. In contrast to a planar NLC layer featuring only a tangential component of the convective flow velocity in the rolls, the twist NLCs possess an additional axial velocity component whose direction changes from one roll to another [4].

The results of the Fourier analysis of the microscopic images showed that, upon the transition from linear to 2D domain structure, the perpendicular component of the wave vector $q_\perp$ (perpendicular to the director in the middle of the layer and, hence, parallel to the rolls) exhibits virtually no variation with increasing applied voltage (unlike the component $q_\parallel$ parallel to the director), which is evidence of stability of the transverse spatial mode. The dependence of the wave vectors in the 1D and 2D domain structures on the applied voltage is shown in Fig. 1.

The stability of the 2D structure depends to a considerable extent on the presence of defects. These defects are essentially the edge dislocations of the 1D roll structure (see the inset in Fig. 2). Similar to the case of planar nematics [5], defects in the twist NLCs exhibit two types of motions—climb and glide (parallel and perpendicular to the roll axis, respectively). The rolls on one side of the defect are compressed and those on the other side are stretched in the direction perpendicular to the roll axis. The effective period of rolls on one side is smaller than that on the other, so that the defects move predominantly along the rolls. The glide motion is observed for the interaction of defects possessing opposite signs. As the applied voltage increases, the density of defects remains unchanged until the onset of the 1D–2D transition (Fig. 2a). After the formation of a 2D structure, the density of defects as a function of the applied voltage tends to saturation. This behavior is related to the fact that the density of the elastic distortion energy of the defect becomes comparable with the energy of deformation of the 2D structure ($F \sim q_\perp^2$). Thus, an increase in the number of defects corresponds to the growth of fluctuations, while the saturation of the density of defects reflects the formation of a stationary 1D and 2D domain structure (see the transition region in Fig. 1).

Figure 2b shows the dependence of the average effective defect length on the voltage. The formation of the 1D domain structure is accompanied by large scatter of the effective defect size L ($2\lambda \le L \le 30\lambda$, where $\lambda = 2\pi/q_\parallel$ is the period of the 1D lattice of rolls). At $\varepsilon \sim 1.3$, the defects begin to divide with increasing fluctuations and at $\varepsilon \sim 1.8$, the average defect length decreases to a minimum value of $L = 2\lambda$. This coincides with the region of transition states, determining the appearance of the periodic deformations along the rolls, although the wave vector $q_\perp$ (but not $q_\parallel$) remains virtually unchanged with increasing parameter ε.

In conclusion, we have demonstrated that the symmetry of twist NLCs and the sequence of structural transitions in these LCs are significantly different from those in the case of planar NLC configuration. This is related to the twist of the NLC director field. It is established that the 1D–2D transition is accompanied by an increase in the density of defects in the initial roll structure. The transition is characterized by a certain region ΔU of applied voltages (smeared transition). This is probably related to an additional elastic deformation of the director field in the vicinity of defects; a high density of such defects leads to a decrease in the critical voltage for the transition.

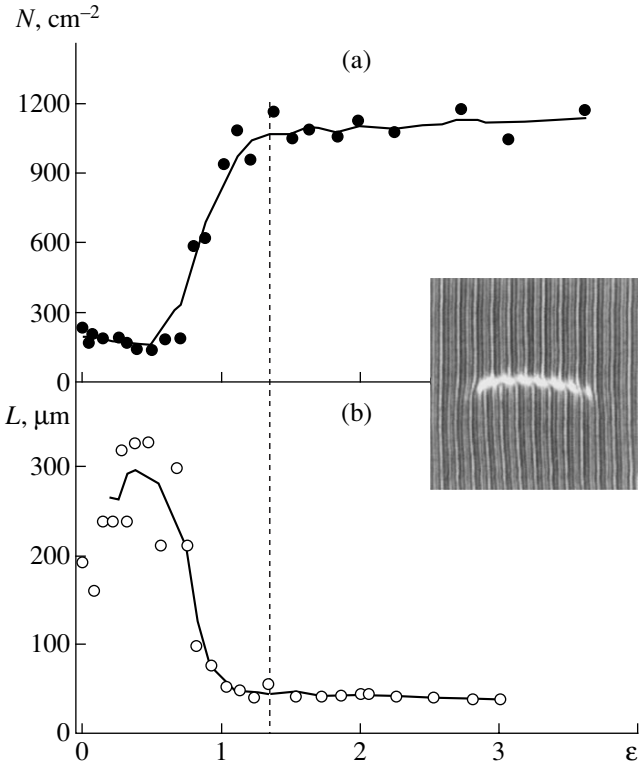

Fig. 2. Plots of the (a) defect density N and (b) average effective defect length L versus the control parameter ε. The inset shows an image of the characteristic structural defect.

Acknowledgments. This study was supported by the Federal Program "Integration" (project no. B0065) and by the Russian Foundation for Basic Research (project no. 02-02-17435).

REFERENCES

1. S. Nasumo, S. Takeuchi, and Y. Sawada, Phys. Rev. A **40**, 3457 (1989).
2. I. Rehberg, S. Rasenat, and V. Steinberg, Phys. Rev. Lett. **62**, 756 (1989).
3. A. P. Krekhov and O. A. Skaldin, Pis'ma Zh. Tekh. Fiz. **18** (20), 24 (1992) [Sov. Tech. Phys. Lett. **18**, 659 (1992)].
4. A. Hertrich, A. P. Krekhov, and O. A. Scaldin, J. Phys. II **4**, 239 (1994).
5. A. Weber, E. Bodenschatz, and L. Kramer, Adv. Mater. **3**, 191 (1991).

Translated by P. Pozdeev

Technical Physics Letters, Vol. 29, No. 11, 2003, pp. 894–896. Translated from Pis'ma v Zhurnal Tekhnicheskoĭ Fiziki, Vol. 29, No. 21, 2003, pp. 32–39.

Acoustooptical Processor Used for Pulsar Radio Emission Observations

N. A. Esepkina*, Yu. P. Ilyasov, A. P. Lavrov, S. A. Molodyakov, and V. V. Oreshko

St. Petersburg State Technical University, St. Petersburg, 195251 Russia

** e-mail: esepkina@cef.spbstu.ru*

Received May 14, 2003

Abstract—A new type of acoustooptical processor (AOP) for the investigation of pulsar radio emission is proposed that provides for the compensation of signal dispersion in a broad frequency range. The AOP is based on an acoustooptical spectrum analyzer with a CCD photodetector operating in a special shift-and-add mode, which allows spectral components of the input signal to be added with a controlled time delay immediately in the CCD photodetector. The proposed AOP was successfully used on an RT-64 radio telescope (Kalyazin Radio Astronomy Observatory) for the observation of pulsars at 1.4 GHz in a bandwidth of 45 MHz. © *2003 MAIK "Nauka/Interperiodica".*

Introduction. Both astrophysics and observational radio astronomy study pulsars, which represent neutron stars with high and very stable rotation velocities. Important information about physical processes in pulsars is provided by investigations of the pulsed radio emission from these objects. This emission is observed in a wide frequency range (from 100 MHz to 10 GHz) with a repetition period T_R from several milliseconds to several seconds.

The radio emission of pulsars has a number of peculiarities, the main one being strong dispersion in interstellar medium [1]. Because of this dispersion, a short pulse of radio emission exhibits frequency drift within a bandwidth Δf around a central frequency f. The drift from high to low frequencies proceeds at a rate of

$$\alpha_{DM} = \frac{f^3}{8.3 \times 10^3 DM} \quad [\text{MHz/s}], \qquad (1)$$

where DM is the pulsar dispersion measure [pk/cm^3] and f is the frequency [MHz]. This leads to a broadening of the pulse at the receiver output and the loss of information about fine temporal structure of the input signal. Therefore, dispersion does not allow the receiver bandwidth to be expanded for gaining sensitivity, limiting it by the value $\delta f_{in} = \alpha_{DM}\delta t$, where δt is the required time resolution. This limitation can be removed by summing a large number of narrowband signals upon compensation for the dispersion delay in each channel, that is, by including a special device—a dispersion compensator—into the receiver of pulsar radiation.

There are several known types of dispersion compensators, the most widely used being the incoherent postdetector dispersion compensator based on a multichannel filter bank. In this device, the output signals s_n in all N channels of the multichannel filter bank are simultaneously detected to form an $s_{n,k}$ data array (where n is the channel number and k is the time count number) and then added according to an algorithm (2) that eliminates the dispersion and increases the signal-to-noise (S/N) ratio by a factor of $\sqrt{N}$:

$$s_\Sigma(k) = \sum_{n=1}^{N} s_{n,k+\Delta n}, \qquad (2)$$

where Δ is the time shift depending on the pulsar dispersion measure.

In order to provide for a significant gain in the S/N ratio with increasing receiver bandwidth, it is necessary to use a filter bank with a large number of channels, which presents a considerable technical problem. As is known, the problem of forming a large number of equivalent frequency channels with a resolution $\delta f \geq 100$ kHz can be rather simply solved with the aid of acoustooptical spectrum analyzers (AOSs) widely used for spectral investigations in radio astronomy [2]. An AOS has been used as a multichannel filter bank for pulsar observations [3].

We propose an AOP of the new type, capable of simply and effectively eliminating the negative effect of dispersion during processing of a wideband signal. In the new device, the spectral components are added with controlled delay immediately in a CCD photodetector [4].

Acoustooptical processor for pulsar signals. Figure 1 shows a scheme of the proposed AOP. This system, while generally corresponds to the conventional AOS scheme, employs a CCD photodetector operating in a special regime. As can be seen from Fig. 1, the input radio signal $s(t)$ to be processed is fed (upon amplification and transformation to an intermediate frequency) into an acoustooptical modulator (AOM). The AOM and a Fourier lens perform Fourier transforma-

tion of the input signal, forming an optical intensity distribution $I(x, t)$ in the output focal plane. The spatial coordinate x is linearly related to the frequency f of the radio signal. The distribution $I(x, t)$ reflects the power spectrum $S(f)$ of the input signal $s(t)$ within a sliding time window of duration T_A (T_A is the time aperture of the AOM). In usual AOSs, the distribution $I(x, t)$ is detected and accumulated with an N-element CCD photodetector. Upon elapse of a preset accumulation time T_I, the distribution is subjected to readout in the form of a sequence of counts $s_n \sim S(f_n)$, digitized, and fed into a digital processor. The time T_I determines temporal resolution of the AOS.

In the proposed AOP, the CCD photodetector operates in a shift-and-add mode, which is ensured by a special controller (control signal generator). Under the action of signals (F_{ph}) generated by the controller, elements of the CCD photodetector are electronically transferred over the aperture from one to another edge like on a conveyor. During this transfer of charge packets, each element simultaneously performs detection and accumulation (adding) of signals from various frequency channels with the corresponding delay δt, by scanning over these channels one by one. Thus, the addition according to (2) is performed on a real time scale inside the CCD photodetector in an analog form (as charged packets) prior to readout. Amplified and digitized, the output signal $U_\Sigma(k)$ is fed to the registration system.

The velocity V of the motion of elements in the photodetector is determined by the control system, $V = lF_{ph}$ (where F_{ph} is the control frequency, and l is the element to element spacing). This velocity can be matched with high precision to the frequency drift (1) in the received radio signal, $V_{DM} = K\alpha_{DM}$, where K is a constant determined by the optical scheme of the processor. The output signal of the CCD photodetector contains a component corresponding with the envelope of the pulsar signal, which is compressed as compared to the output signal of a usual wideband receiver. The dispersion compensation in the AOP is accomplished on the real time scale immediately in the CCD photodetector, so that the AOP performs the function of the dispersion compensator.

The proposed AOP has a number of advantages. The addition according to (2) is performed in the CCD photodetector, which increases the S/N ratio and decreases the rate of readout N times as compared to that in the AOS [3]. Another advantageous distinctive feature of the new AOP is simplicity of readjustment required for the observation of pulsars with various dispersion measures: this readjustment is performed electronically, by simply tuning the control signal frequency F_{ph}.

We have designed and constructed a working prototype of the AOP performing the function of a dispersion compensator. The setup employed a He–Ne laser (LGN-207A), an AOM based on a [110]-cut TeO_2 crystal with a time aperture of $T_A \approx 15$ μs, and a linear CCD

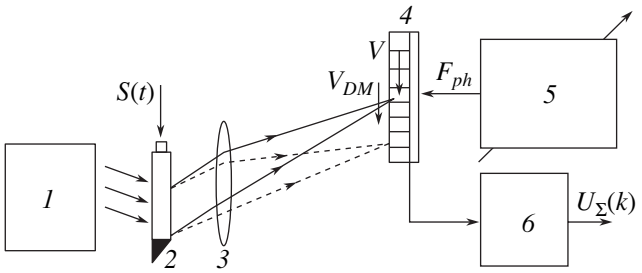

Fig. 1. Schematic diagram of the acoustooptical processor (AOP): (*1*) laser and beam-forming system; (*2*) acoustooptical modulator (AOM); (*3*) Fourier lens; (*4*) CCD photodetector; (*5*) controller (control signal generator); (*6*) video amplifier and analog-to-digital converter.

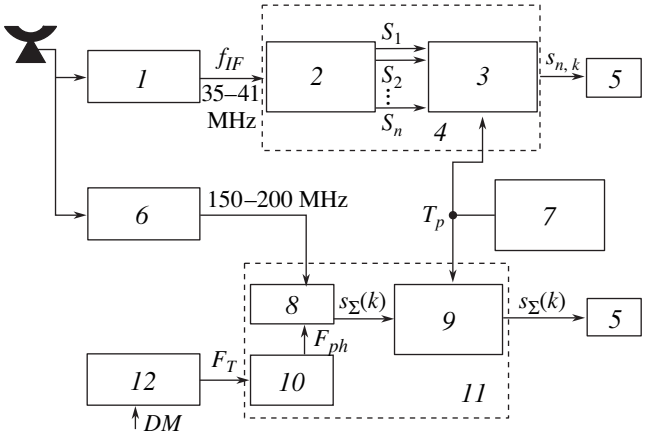

Fig. 2. Schematic diagram of the receiver complex of RT-64 radio telescope for pulsar observations at 0.6 and 1.4 GHz: (*1*) 608–614 MHz receiver; (*2*) 160-channel filter bank; (*3*) buffer digital storage (160 × 256); (*4*) filter dispersion compensator unit; (*5*) computer; (*6*) 1.41–1.76 GHz receiver; (*7*) programmable T_R synthesizer; (*8*) acoustooptical processor (AOP); (*9*) buffer digital storage (4096); (*10*) CCD photodetector; (*11*) AOP–dispersion compensator unit; (*12*) tunable generator.

photodetector (Sony ILX-703A) comprising 2048 elements (14 × 14 μm). The AOP was characterized by a central frequency of f_0 = 150 MHz, a working frequency band Δf_A = 80 MHz, and a frequency channel step of about 82 kHz. Upon changing the master frequency F_T, the CCD photodetector provided readjustment of the AOP for the observation of pulsars with dispersion measures from 15 to 1000 pk/cm^3.

Pulsar observations on a radio telescope with AOP. The AOP prototype was installed in a pulsar receiver complex of an RT-64 radio telescope with an antenna diameter of 64 m (Kalyazin Radio Astronomy Observatory, Lebedev Physical Institute of the Russian Academy of Sciences). Pulsar observations were performed with two receivers operating in the frequency ranges of 600 MHz and 1.4 GHz.

The structure of the receiver complex is schematically depicted in Fig. 2. The 600 MHz tract included a

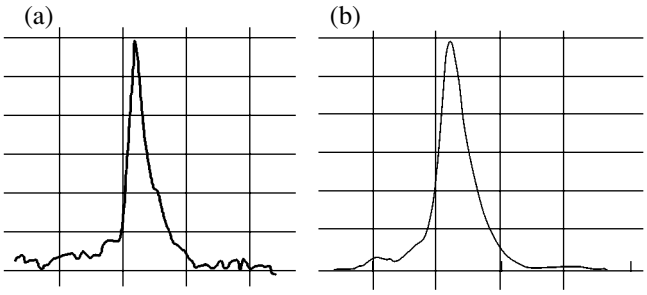

Fig. 3. PSR 1713+07 pulsar signal profiles at 1.4 GHz obtained using (a) 64-m radio telescope (RT-64, Kalyazin) and (b) 300-m radio telescope (Aresibo) [6].

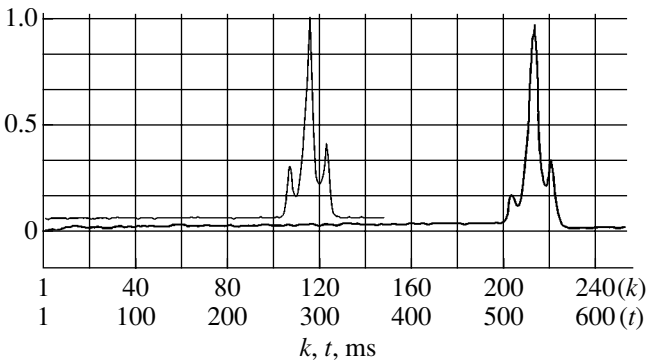

Fig. 4. Dispersion delay of PSR 0329+54 pulsar signals measured simultaneously at two frequencies on an RT-64 radio telescope (Kalyazin).

standard 160-filter postdetector dispersion compensator (FIAN AS-600/160) containing 2 × 80 channels (40-kHz filters) with a total bandwidth of 6.4 MHz [5]. The 1.4 GHz tract incorporated the proposed dispersion compensator with the parameters described above. The input signal was fed to the AOP after being converted into an intermediate frequency of f_{IF} = 175 MHz. Because of a difference between the central AOP frequency (f_0 = 150 MHz) and the intermediate frequency f_{IF}, the bandwidth of the 1.4 GHz tract was 45 MHz.

Most pulsars are characterized by small power flux densities at 1.4 GHz (on the order of 10^{-28} W/(m^2 Hz)), which requires additional signal accumulation over large numbers (up to 10^5 and above) of periods in order to provide for S/N > 1. For this reason, dispersion compensators in both tracts included digital buffer storage performing preliminary accumulation of the $s_{n,k}$ and $s_\Sigma(k)$ signals (subsequent accumulation is performed by a computer). Operation of the digital buffer storage in both dispersion compensators was synchronized by "Pulsar Period T_P" pulses. A special synchronization system calculated expected moments of the pulsar signal arrival with allowance of the Earth's rotation and other factors.

The proposed dispersion compensator provided for successful observations in the 1.4 GHz range for a number of pulsars in a range of T_R from seconds to milliseconds. Simultaneously and synchronously, the observations were also performed in the 600 MHz tract using a standard 160-channel complex FIAN AS-600/160.

Figure 3a shows the profile of a signal from a millisecond pulsar PSR 1713+07 obtained in the 1.4 GHz range with RT-64. For the comparison, Fig. 3b shows an analogous profile obtained with a 300-m radio telescope in Aresibo [6].

Figure 4 presents the results of synchronous observations of pulsar PSR 0329+54 with DM = 26.8 pk/cm^3 in two frequency ranges with the central frequencies f_1 = 1425 MHz and f_2 = 600 MHz. Note a delay of 254 ms in the signal arrival time, which is related to dispersion in the interstellar medium. The calculated value of delay $\Delta t_{DM} = 4.15 \times 10^3 \left(\frac{1}{f_2^2} - \frac{1}{f_1^2}\right) DM$ amounts to 254.2 ms. Synchronous observations of pulsars at two frequencies on RT-64 open the possibility of studying frequency fluctuations of the dispersion measure. This is important, for example, for timing pulsars in the creation of a global pulsar time scale.

Thus, we have developed a broadband acoustooptical dispersion compensator of the new type for the registration of pulsar radio emission signals with real-time compensation for the signal dispersion and demonstrated possibilities of the prototype system in operation with an RT-64 radio telescope.

Good prospects for the use of acoustooptical methods in pulsar signal processing are related to expansion of the bandwidth and to the use of AOP with a two-channel acoustooptical modulator which makes possible joint Fourier transforms of two radio signals with orthogonal polarizations (received by the radio telescope antenna). This allows phase relations between the two signals to be determined and their polarization characteristics to be studied, which is very important for the physics of pulsars.

Acknowledgments. The authors are grateful to I.I. Saenko and S.K. Kruglov for their participation in development of the acoustooptical processor.

REFERENCES

1. R. N. Manchester and J. H. Taylor, *Pulsars* (Freeman, San Francisco, 1977; Mir, Moscow, 1980).
2. L. Malkamaki, K. Mattila, A. Raisanen, *et al.*, Exp. Astron. **2**, 149 (1991).
3. Y. Hanado, M. Imae, and M. Sekido, IEEE Trans. Instrum. Meas. **44**, 107 (1995).
4. N. A. Esepkina, A. P. Lavrov, and S. A. Molodyakov, Izv. Vyssh. Uchebn. Zaved., Radioélektronika, No. 2, 21 (1998).
5. Yu. P. Ilyasov, V. V. Oreshko, and O. V. Doroshenko, Tr. Fiz. Inst. Ross. Akad. Nauk **229**, 95 (2000).
6. R. S. Foster, A. Wolszczan, and F. Camilo, Astrophys. J. **410**, L91 (1993).

Translated by P. Pozdeev

Technical Physics Letters, Vol. 29, No. 11, 2003, pp. 897–900. Translated from Pis'ma v Zhurnal Tekhnicheskoĭ Fiziki, Vol. 29, No. 21, 2003, pp. 40–47.

Atomic Hydrogen Flux Density Measured Using Thin Metal Films

V. A. Kagadeĭ*, E. V. Nefyodtsev, D. I. Proskurovsky, and S. V. Romanenko

Institute of High-Current Electronics, Siberian Division, Russian Academy of Sciences, Tomsk, Russia

** e-mail: vak@lve.hcei.tsc.ru*

Received May 15, 2003

Abstract—Using one- or two-layer films of transition metals, it is possible to determine the atomic hydrogen flux density under reduced gas pressure conditions (10^{-1}–10^{-3} Pa). The method consists in monitoring a change in the film resistance caused by selective dissolution of atomic hydrogen in the metal during exposure of the film in a mixed atomic-molecular flow, followed by determining a characteristic time τ required for the hydrogen concentration in the film to reach 63% of the maximum possible level. The hydrogen flux density is then calculated within the framework of a simple mathematical model of the film saturation with hydrogen described by a relaxation law. The proposed method is characterized by a high selective sensitivity to atomic hydrogen. The atomic hydrogen flux density in a mixed atomic-molecular flow can be determined in a range from 5×10^{13} to 10^{16} cm^{-2} s^{-1}. © *2003 MAIK "Nauka/Interperiodica".*

The micro- and nanoelectronic technologies extensively implement the methods of treating semiconductors with the flows of neutral chemically active particles, in particular, atomic hydrogen [1, 2]. The fluxes of atomic hydrogen are characterized with the aid of chemical sensors and by physical techniques such as calorimetry, mass spectroscopy, and optical and laser spectroscopy [3–8]. The existing methods and available instruments are still far from being perfect. For this reason, development of new detectors of atomic hydrogen based on alternative physical principles is of considerable interest.

As is known, hydrogen dissolved in transition metals increases resistivity of the material [9–11]. This principle is used in molecular hydrogen sensors based on palladium operating at atmospheric pressure [12, 13]. Taking into account that hydrogen atoms penetrate into transition metals at a much higher probability than do molecules [11], we suggested that an analogous principle can be used for measuring the flux density of atomic hydrogen at a reduced gas pressure (10^{-1}–10^{-3} Pa). Below we report on the first investigation of the possibility of using thin films of transition metals for the measurement of atomic hydrogen flux density.

The experiments were performed on samples deposited onto polished ceramic plates with dimensions 2.5×30 mm. Connecting leads were brazed to the contact areas at the plate ends, formed by sequential deposition of Cr and Ni films. Then, the whole sample surface was covered with a thin vanadium film by thermal deposition in vacuum, after which (without admitting air) the thin-film samples were hydrogenated by exposure to a mixed flow of atomic and molecular hydrogen. The residual gas pressure in the vacuum chamber was $(1-4) \times 10^{-4}$ Pa. The flow of neutral particles was formed by a source of atomic hydrogen based on a low-pressure gas arc discharge phase [14]. The discharge current, voltage, and gas flow rate were 2 A, 180 V, and 10 sccm, respectively. In the course of the experiment, the increment of vanadium film resistance $\Delta R = R - R_0$ was measured as a function of hydrogenation time t.

It was found that the exposure of a vacuum-deposited V film in a flow of molecular hydrogen (flow rate, 10 sccm; hydrogen pressure, 10^{-2} Pa; time, 30 min) does not lead to a change in the sample resistance. However, a different result was observed when an analogous thin-film sample was exposed to a mixed flow of atomic and molecular hydrogen at the same flow rate. Figure 1 (curve *1*) shows the typical curve of $\Delta R(t)/R_0$ obtained in such experiment. As a result of the hydrogenation, the film resistance increases by ≅60%. The same figure (curve *1*) shows the rate of variation of the relative increment, $d[\Delta R(t)/R_0]/dt$, in which a clear minimum is observed at $t_1 = 3$ min. The results of the experiments showed that both the initial growth rate of the resistance and the position of minimum depend on the atomic hydrogen flux density. As the flux density grows, the $d[\Delta R(t)/R_0]/dt$ value at $t \longrightarrow 0$ increases, while t_1 decreases.

Thus, the exposure of thin vanadium films in a mixed atomic-molecular hydrogen flow leads to selective dissolution of atomic hydrogen in the metal, with the time of attaining minimum on the $d[\Delta R(t)/R_0]/dt$ curve depending on the incident atomic flux density. The existence of such regularities allows the density of

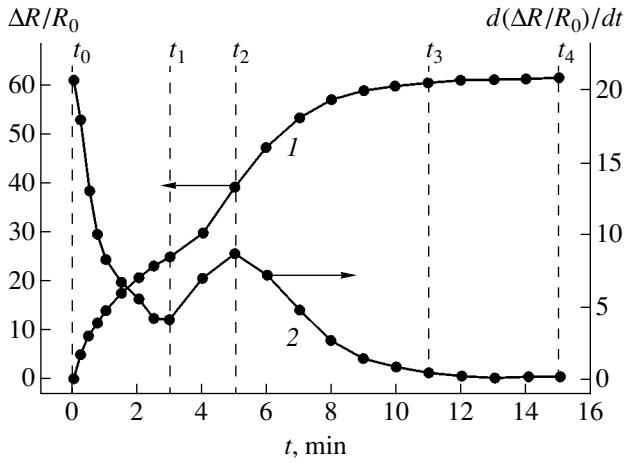

Fig. 1. Plots of (*1*) the relative resistance increment and (*2*) the rate of its variation versus the hydrogenation time *t* for a thin vanadium film.

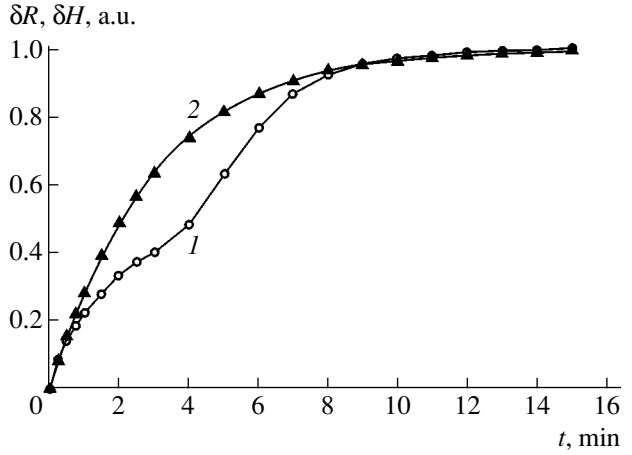

Fig. 2. Plots of (*1*) the normalized resistance increment $\delta R(t)$ and (*2*) the normalized hydrogen concentration $\delta H(t)$ versus the hydrogenation time *t* for a thin vanadium film.

the atomic hydrogen flux incident onto the film surface to be calculated. For this purpose, it is necessary to establish the law governing a change in the hydrogen concentration in the film in the course of hydrogenation and find a relation between the hydrogen concentration in the metal and the $\Delta R(t)/R_0$ value.

As is known from published data [10], a minimum in the dependence of the film resistivity on the hydrogenation time corresponds to the formation of a β-$VH_{0.5}$ phase in the vanadium film. Therefore, we may suggest that the minimum observed in the curve of $d[\Delta R(t)/R_0]/dt = f(t)$ also corresponds to termination of the formation of this vanadium hydride phase in the film. Then, only a monoclinic crystalline β phase of $VH_{0.5}$ with a hydrogen content of 33 at. % is present in the film at $t = t_1$ [9]. This assumption was confirmed by the results of preliminarily experiments involving determination of the content of hydrogen in the vanadium films [15].

Let us consider the kinetics of saturation of a thin metal film with hydrogen. From simple considerations, it is clear that the rate of hydrogen dissolution in the film must decrease as the gas concentration in the metal approaches a certain limiting value N_S. We assume that (i) each hydrogen atom incident onto the vanadium surface penetrates into the film to occupy an interstitial position, (ii) the hydrogen concentration *H* has no gradient across the film thickness *h* (hydrogen is uniformly distributed in the film); (iii) the film contains no sinks and traps for atomic hydrogen; and (iv) the metal film–substrate boundary is impermeable for hydrogen atoms and is not a sink for these atoms.

Under these conditions, the kinetic of hydrogen dissolution can be described by the following relation:

$$dH/dt = J/(hN_P)(N_P - H) - \varphi(J/hN_P)H - \gamma H^2, \quad (1)$$

where *J* is the flux density of atomic hydrogen incident onto the film surface; N_P is the density of interstitial sites in the metal lattice, which can be occupied by hydrogen atoms under given thermodynamic conditions; and φ and γ are coefficients characterizing the rates of processes involved in the hydrogen dissolution. The first term in the right-hand part of Eq. (1) described an increment in the hydrogen concentration *H* per unit time, which is proportional to the incident flux *J* and the number of unoccupied interstitial sites. The second and third terms describe the loss of atomic hydrogen from the film as a result of recombination with the formation of hydrogen molecules. This recombination takes place between hydrogen atoms on the surface and ether incident atoms (Rideal–Eley mechanism, second term) or atoms emerging from the bulk (Langmuir–Hinshelwood mechanism, third term).

Holding the metal samples in vacuum after termination of the hydrogenation cycle showed that the flux of hydrogen escaping from film to vacuum by the Langmuir–Hinshelwood mechanism is insignificant as compared to the incident flux during hydrogenation, so that the former flux can be ignored. Then, a solution to Eq. (1) under the initial condition that $H(0) = 0$ is

$$H(t) = N_S[1 - \exp(-t/\tau)], \quad (2)$$

where $N_S = N_P/(1 + \varphi)$ and $1/\tau = [(1 + \varphi)/(hN_P)]J$. The characteristic time τ has the meaning of a hydrogenation time required for the hydrogen concentration in the film to reach 63% of the maximum possible level.

Figure 2 compares the experimental plot of $\delta R(t)$ (curve *1*) to a theoretical curve of $\delta H(t)$ (curve *2*), where $\delta R(t) = \Delta R(t)/(R_S - R_0)$ is the normalized resistance increment (R_S is the saturation resistance) and $\delta H(t) = H(t)/N_S \cong 1 - \exp(-t/\tau)$ is the normalized hydrogen concentration. As can be seen, the theoretical curve

coincides with the experimental plot in the initial and final portions, that is, in the regions of existence of virtually pure α and β phases for which the increment of resistance is due to an increase in the scattering of conduction electrons on hydrogen atoms. A difference between the two curves in the intermediate region reflects the formation of vanadium hydride $VH_{0.5}$ in the film, which is accompanied by nonmonotonic variation of the resistance.

Assuming that the concentration of hydrogen at the time $t_1 = 3$ min (Fig. 1) reaches 33 at. % (corresponding to the $VH_{0.5}$ phase composition), we readily calculate that the limiting hydrogen concentration attained in the experiment is $N_S \cong 42$ at. % (corresponding to $VH_{0.74}$). At room temperature, this corresponds to a transition from monoclinic β phase to tetragonal β' phase [9]. It should be noted that the same limit was attained in the experiments reported in [16]. This result suggests that the limiting concentration N_S under the given experimental conditions is determined by the complete saturation of interstitial sites, rather than by the balance between incident and escaping hydrogen fluxes. From this it follows that our experiments correspond to $\varphi \ll 1$ and $N_S = N_P$, so that the working relation for determining the atomic hydrogen flux density is

$$J = N_P h/\tau. \quad (3)$$

In the right-hand part of this relation, all quantities are known except the characteristic time τ ($N_P = 5.28 \times 10^{22}$ cm^{-3}). Using relation (2), the characteristic time can be expressed via hydrogen concentration as

$$\tau = -t\ln(1 - H/N_S). \quad (4)$$

An analysis of relations (2) and (4) shows that τ can be determined from the experimentally measured resistance kinetics $\Delta R(t)$ by one of the following methods:

(a) $\tau = 0.902t_1$,

(b) $\tau = 1.6R_0/(dR/dt|_{t\to 0})$,

(c) $\tau = -t/\ln[1 - \delta H(\delta R(t))]$,

where $dR/dt|_{t\to 0}$ is the initial slope of the $\Delta R(t)$ curve, t is an arbitrary current time, and $\delta H(\delta R)$ is the dependence of the normalized hydrogen concentration on the normalized resistance increment constructed using the data measured at every experimental point. The first method is intended for determining fluxes with a density of 5×10^{14} cm^{-2} s^{-1} and above. In this case, the hydrogenation time necessary for determining t_1 does not exceed 10 min (for technologically convenient thicknesses of vanadium films). The second method is recommended for determining hydrogen fluxes of lower density, because the first method would require an unacceptably long period of time. The third method can be used for determining fluxes of any density, provided that the measurements are performed using a series of thin-film sensors with identical parameters (e.g., manufactured in the same batch). In this case, one sensor is used for constructing a calibration plot of $\delta H(\delta R)$ which is employed in what follows for all sensors of the given batch. The duration of measurements t_1 can be arbitrary, falling within the interval of normalized resistance increments $\delta R < 0.9$ (operation in the region of saturation involves large uncertainties).

Using the first method, we determine that the experimental data presented in Fig. 1 correspond to a sample exposed to the atomic hydrogen flux with a density of $J = 3.3 \times 10^{15}$ cm^{-2} s^{-1}.

The main disadvantage of the proposed method of determining the atomic hydrogen flux density is the need to combine the process of hydrogen-sensitive film deposition and the procedure hydrogen flux density measurement in a single vacuum system operation cycle. This is necessary in order to ensure 100% probability for the atomic hydrogen penetration into the metal film, which takes place only for the unoxidized vanadium surface. The results of our additional investigations showed that multilayer compositions based on transition metal films with palladium as the outermost layer can be exposed to air for a long time without losing sensitivity. If the palladium film thickness is significantly smaller than that of vanadium, the hydrogen-absorbing properties of the two-layer system are close to those of a single layer vanadium film and the t_1 point on the $d[\Delta R(t)/R_0]/dt = f(t)$ curve is readily determined.

In conclusion, we have demonstrated that it is possible to measure the atomic hydrogen flux density using thin-film resistive sensors. The results of our experiments show that such sensors are characterized by sufficiently high precision and selectivity, and allow the atomic hydrogen flux densities to be determined in a range from 5×10^{13} to 10^{16} cm^{-2} s^{-1}.

REFERENCES

1. S. Leone, Jpn. J. Appl. Phys. **34**, 2073 (1995).
2. R. S. Goodman, N. Materer, and S. R. Leone, J. Vac. Sci. Technol. B **15**, 971 (1997).
3. G. Bruno, M. Losurdo, and P. Capezzuto, Appl. Phys. Lett. **66**, 3573 (1995).
4. L. V. Serikov, L. N. Shiyan, and A. F. Gorbachev, *et al.*, RF Inventor's Certificate No. 1603257 (1998).
5. V. A. Lavrenko, *Recombination of Hydrogen Atoms on Solid Surfaces* (Naukova Dumka, Kiev, 1973).
6. A. Sutoh, Y. Okada, S. Ohta, *et al.*, Jpn. J. Appl. Phys. **34**, L1379 (1995).

7. B. F. Gordiets, M. J. Pinheiro, E. Tatarova, *et al.*, in *Proceedings of the XXIV International Conference on Phenomena in Ionized Gases, Warsaw, 1999*, Vol. 2, p. 133.
8. A. M. Bruneteau, G. Hollos, M. Bacal, *et al.*, J. Appl. Phys. **67**, 7254 (1990).
9. *Hydrogen in Metals*, Ed. by G. Alefeld (Springer-Verlag, Völkl, 1978).
10. E. Fromm and E. Gebhardt, *Gases and Carbon in Metals* (Springer-Verlag, Berlin, 1976).
11. *Interaction of Hydrogen with Metals*, Ed. by A. P. Zakharov (Nauka, Moscow, 1987).
12. B. S. Hoffheins, L. C. Maxey, W. Holmes, Jr., *et al.*, in *Proceedings of the US Department of Energy Hydrogen Program Review*, pp. 320–328.
13. Y.-T. Cheng, R. Hills, Y. Li, *et al.*, US Patent No. 6670115 (1997).
14. V. A. Kagadei and D. I. Proskurovsky, J. Vac. Sci. Technol. A **16**, 2556 (1998).
15. V. A. Kagadeĭ, E. V. Nefedtsev, D. I. Proskurovskiĭ, *et al.*, Izv. Vyssh. Uchebn. Zaved., Fiz. (2003, in press).
16. D. G. Westlake, S. T. Ockers, and W. R. Gray, Metall. Trans. **1**, 1361 (1970).

Translated by P. Pozdeev

Technical Physics Letters, Vol. 29, No. 11, 2003, pp. 901–903. Translated from Pis'ma v Zhurnal Tekhnicheskoĭ Fiziki, Vol. 29, No. 21, 2003, pp. 48–54.

Optical Characterization of Biological Tissues: Determining Absorption and Scattering Coefficients

K. M. Giraev, N. A. Ashurbekov*, and O. V. Kobzev

Dagestan State University, Makhachkala, Dagestan, Russia

** e-mail: nashurb@phys.dgu.ru*

Received April 29, 2003

Abstract—We have measured the spectra of diffuse reflection and the total and collimated transmission of the mucous membrane of the stomach in the normal state by the methods of integrating spheres and single scattering in a wavelength range from 350 to 750 nm. The optical characteristics of this biological tissue were determined by solving the inverse scattering problem using the Kubelka–Munk three-flux model and the diffusion method. A comparative analysis of the results is presented. © *2003 MAIK "Nauka/Interperiodica".*

Determination of the optical characteristics (absorption coefficient μ_a, scattering coefficient μ_s, and anisotropy factor g) of biological media is a very difficult task. The difficulties are caused by the complex structure of biological tissues and by a complicated process of the photon–medium interaction, since biological tissues represent inhomogeneously absorbing and multiply scattering media [1, 2]. Modern methods developed for determining the optical parameters of biological media are based on the solution of the inverse scattering problem within the framework of various theoretical models describing the propagation of light in such systems, including the Monte Carlo method [2, 3], diffusion approximation [4–6], and the Kubelka–Munk flux models [2, 7–9].

This paper is devoted to determining the optical parameters (μ_a, μ_s, g) of biological tissues using the Kubelka–Munk three-flux model. For this purpose, we have studied the spectra of collimated transmission ($T_C = F_C(z)/F_{C0}$), total transmission ($T_d = F_+(z)/F_{C0}$), and diffuse reflection from the front ($R_{d1} = F_{0-}/F_{C0}$) and rear ($R_{d2} = F_-/F_{C0}$) boundaries of the mucous membrane taken from the antral part of the stomach. Here, F_{C0} is the incident light flux; $F_C(z)$ and $F_+(z)$ are the transmitted collimated and diffuse fluxes, respectively; $F_{0-}(z)$ and $F_-(z)$ are the diffuse fluxes reflected from the front and rear boundaries of the tissue; and z is the tissue sample thickness. The calculated values of T_d, R_{d2}, and T_C were also used to determine the optical characteristics of the material within the framework of the diffusion approximation as described in [5].

The experiments were performed with natural tissue slices cut from the mucous membrane of the antral part of the stomach in the normal state. The samples with an area of ~1 cm^2 and a thickness of ~600 or ~75 μm were prepared using a cryostat microtome. The sections wetted with a drop of physiological solution were placed between object and cover glasses. In order to prevent drying of the sample, the edge gap was sealed with a special glue.

The optical measurements were performed using a halogen lamp (KGM-100) as a light source and a grating monochromator with a reciprocal dispersion of 3.2 nm/mm capable of linearly scanning over the spectrum in a wavelength range from 300 to 800 nm. The incident light beam was intensity-modulated by a chopper at a frequency of ~150 Hz, passed through a collimator and a diaphragm, and struck the sample to make a spot with a diameter of ~2 mm. The measurements of T_d and $R_{d1, 2}$ were performed using an integrating sphere with a diameter of 10 cm and port areas of ~1.5 cm^2. The signal was detected by a photomultiplier and fed via a lock-in amplifier and an interface to a computer. In the measurements of T_C, the integrating sphere was replaced with two diaphragms, one placed immediately behind the sample and the other in front of the photodetector. The error of spectral measurements was ~10%.

The experimental spectra (T_d, $R_{d1, 2}$, T_C) were corrected to allow for the specular reflection at the air–glass–tissue boundary as described in [6]:

$$J_{corr} = \frac{\left[\left(\frac{(1-r)^2}{r^2 J}\right)^2 + \frac{4}{r^2}\right]^{1/2} - \frac{(1-r)^2}{r^2 J}}{2}.$$

Here, J and J_{corr} are the experimentally measured and corrected intensities, respectively, corresponding to the spectra (T_d, $R_{d1, 2}$, T_C); $r = \frac{r_g + r_t - 2r_g r_t}{1 - r_g r_t} \approx 0.0501$ is the coefficient of specular reflection at the air–glass–tissue boundary; and $r_g \sim 0.0465$ and $r_t \sim 0.004$ are the coefficients of specular reflection at the air–glass and glass–

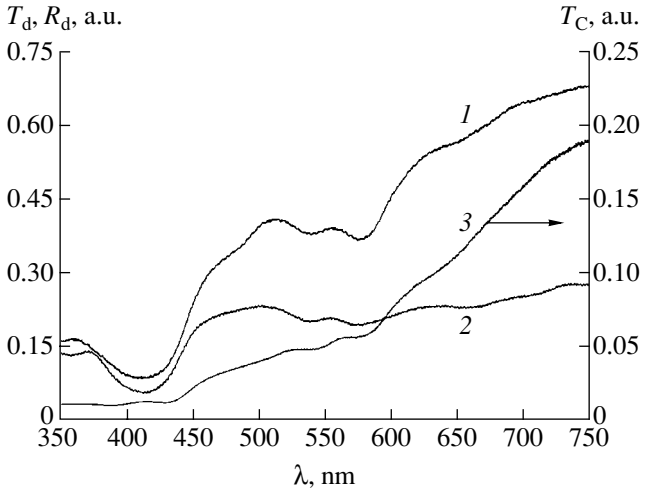

Fig. 1. Optical spectra of the mucous membrane of the antral part of the stomach in the normal state: (*1*) total transmission T_d; (*2*) diffuse reflection R_{d2}; (*3*) collimated transmission T_C.

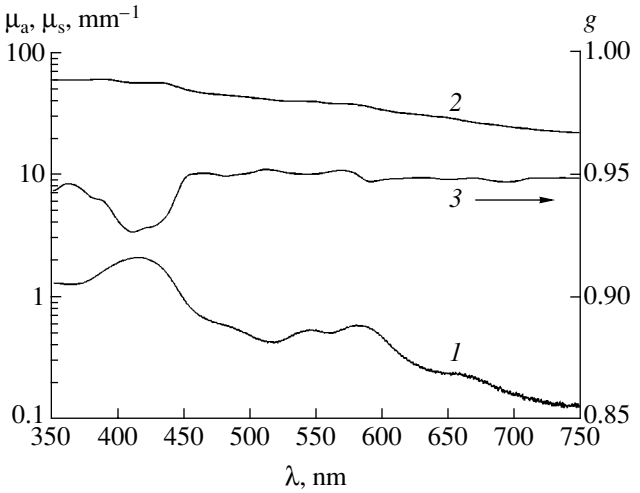

Fig. 2. Optical characteristics of the mucous membrane of the antral part of the stomach calculated using the Kubelka–Munk three-flux model: (*1*) absorption coefficient μ_a; (*2*) scattering coefficient μ_s; (*3*) anisotropy factor g.

tissue interfaces, respectively [6]. The final values of the diffuse reflection and total transmission coefficients were calculated by the formulas [5, 6]

$$R_{d1,2} = \frac{R_{S1,2} - R_0}{R_{100} - R_0}, \quad T_d = \frac{T_S - T_0}{T_{100} - T_0},$$

where $R_{S1,2}$ and T_S are the diffuse reflection and transmission signals from the samples, respectively; R_{100} and T_{100} are the analogous values for the object and cover glasses; and R_0 and T_0 are the signals from the integrating sphere with both ports open (R_0) and with the output port closed (T_0).

The method of determining the optical characteristics of biological tissues within the framework of the Kubelka–Munk three-flux model is described in sufficient detail in [7]. According to this, the distribution of light in the medium is described by difference-differential equations for three fluxes:

$$\frac{dF_C}{dz} = -(\mu_a + \mu_s)F_C(z);$$

$$\frac{dF_+}{dz} = -\left(2\mu_a + \frac{3}{4}(\mu_a + \mu_s(1-g))\right)F_+(z)$$

$$+ \frac{3}{4}(\mu_a + \mu_s(1-g))F_-(z) + \frac{\mu_s}{4}(2+3g)F_C(z); \quad (1)$$

$$\frac{dF_-}{dz} = -\left(2\mu_a + \frac{3}{4}(\mu_a + \mu_s(1-g))\right)F_-(z)$$

$$+ \frac{3}{4}(\mu_a + \mu_s(1-g))F_+(z) + \frac{\mu_s}{4}(2-3g)F_C(z).$$

The boundary conditions for Eqs. (1) are formulated as

$$F_C(0) = (1 - r_{sp,s})F_{C0}; \quad F_+(0) = (1 - r_{sp,c})R_{C0} + r_{id}F_{0-};$$
$$F_+(d) = (1 - r_{sp,c})F_{d+} + r_{id}F_+(d), \quad (2)$$

where F_{d+} is the diffuse flux at the rear boundary of the tissue, $r_{sp.c} \sim 0.004$ is the Fresnel reflection coefficient [6], $r_{id} \approx 0.25$ is the coefficient of internal reflection from both boundaries of the tissue (determined by the formula $r_{id} \approx -1.44n^{-2} + 0.71n^{-1} + 0.668 + 0.0636n$ [4] with $n \approx 1.135$ being the refractive index of the tissue–glass interface [6]).

Solving Eqs. (1) with the boundary conditions (2), we obtain three expressions relating fluxes in the medium at the front and rear boundaries of the object, in which the unknown quantities (μ_a, μ_s, g) are functions of the fluxes. The final solution can be obtained by numerically solving the inverse problem for the system of Eqs. (1)–(2); in this study, this procedure was performed using the Newton method [10].

Figure 1 presents the spectra of total transmission, diffuse reflection, and collimated transmission measured in the spectral range from 350 to 700 nm using a sample of the mucous membrane from the antral part of the stomach. As can be seen, all three quantities show characteristic minima in the regions of 400–425, ~550, and ~580 nm and exhibit an increase in the longwave region. Figure 2 shows the optical characteristics (μ_a, μ_s, g) of the sample tissue calculated using the Kubelka–Munk three-flux model. As can be seen from these curves, μ_s significantly decreases and g varies rather insignificantly with increasing wavelength. This behavior is evidence of an increase in the contribution of μ to the total scattering at a decrease in the Rayleigh

The values of optical characteristics (μ_a, μ_s, g) calculated using the three-flux method and the diffusion model (data in parentheses) for various wavelengths

Wavelength λ, nm	Absorption coefficient μ_a, mm^{-1}	Scattering coefficient μ_s, mm^{-1}	Anisotropy factor g
350	1.27 (1.48)	58.38 (58.16)	0.94 (0.93)
400	1.9 (2.55)	57.11 (56.46)	0.93 (0.93)
450	0.94 (1.28)	49.39 (49.1)	0.95 (0.94)
500	0.47 (0.64)	42.16 (42.0)	0.96 (0.95)
550	0.525 (0.59)	38.98 (38.91)	0.95 (0.95)
600	0.48 (0.51)	33.95 (33.92)	0.95 (0.96)
650	0.23 (0.25)	28.83 (28.81)	0.95 (0.96)
700	0.16 (0.17)	24.3 (24.29)	0.945 (0.96)
750	0.13 (0.14)	21.91 (21.89)	0.95 (0.95)

scattering from cell elements (mitochondria, lysosomes, Golgi apparatus, nucleus, etc.) and submolecular aggregates [1, 2, 5]. The shape of the μ_a contour is determined to considerable extent by the absorption of oxy- and deoxyhemoglobin (~350, 422, 545, and 577 nm) [11] and by the absorption of flavin and porphyrin groups (~390–420 nm) [12].

Using the values of T_d, R_{d2}, and T_C, we have also calculated the optical characteristics (μ_a, μ_s, g) of the tissue within the framework of the diffusion model. The results of calculations by the two models are compared in the table. For some wavelengths (350–550 nm), the value of μ_a calculated using the diffusion model is somewhat overstated as compared to the results of the three-flux model calculation, which can be explained by differences in the model of light propagation in the biological tissue. Determining the optical characteristics within the framework of the three-flux model requires the knowledge of the collimated and diffuse transmission together with the diffuse reflection from the rear and front boundaries of the object, whereas the diffuse model only makes use of the former three coefficients.

To summarize, the results of our investigation show that the optical characteristics of a biological tissue determined using the Kubelka–Munk three-flux model provide a sufficiently adequate description of the object and can be used in biomedical research and spectroscopy—for example, for evaluating the degree of distortions in autofluorescence.

REFERENCES

1. V. V. Tuchin, Usp. Fiz. Nauk **167**, 517 (1997) [Phys. Usp. **40**, 495 (1997)].
2. V. V. Tuchin, S. R. Utz, and I. V. Yaroslavskii, Opt. Eng. **33**, 3178 (1994).
3. J. Qu, C. MacAulay, S. Lam, *et al.*, Opt. Eng. **34**, 3334 (1995).
4. R. A. J. Groenhuis, H. A. Ferverda, and J. J. Ten Bosch, Appl. Opt. **22**, 2456 (1983).
5. J. L. Karagiannes, Z. Zhang, B. Grossweiner, *et al.*, Appl. Opt. **28**, 2311 (1989).
6. D. J. Maitland, J. T. Walsh, and J. B. Prystowsky, Appl. Opt. **32**, 586 (1993).
7. M. J. C. Van Gemert, G. A. C. Schets, M. S. Bishop, *et al.*, Laser Life Sci. **1** (2), 1 (1988).
8. G. Yoon, A. J. Welch, M. Motamedi, *et al.*, IEEE J. Quantum Electron. **QE-23**, 1721 (1987).
9. M. J. C. Van Gemert, S. L. Jacques, H. J. C. M. Sterenborg, *et al.*, IEEE Trans. Biomed. Eng. **36**, 1146 (1989).
10. G. A. Korn and T. M. Korn, *Mathematical Handbook for Scientists and Engineers* (McGraw-Hill, New York, 1968; Nauka, Moscow, 1984).
11. O. S. Wolfbeiss, M. J. Leiner, *et al.*, Anal. Chim. Acta **167**, 203 (1985).
12. S. Udenfriend, *Fluorescence Assay in Biology and Medicine* (Academic, New York, 1962; Mir, Moscow, 1965).

Translated by P. Pozdeev

Technical Physics Letters, Vol. 29, No. 11, 2003, pp. 904–906. Translated from Pis'ma v Zhurnal Tekhnicheskoĭ Fiziki, Vol. 29, No. 21, 2003, pp. 55–61.

IR Radiation Modulator Based on the Effect of Magnetotransmission in Lanthanum Manganite Operating Near Room Temperature

Yu. P. Sukhorukov*, N. N. Loshkareva, A. V. Telegin, E. V. Mostovshchikova, V. L. Kuznetsov, A. R. Kaul', O. Yu. Gorbenko, E. A. Gan'shina, and A. N. Vinogradov

Institute of Metal Physics, Ural Division, Russian Academy of Sciences, Yekaterinburg, Russia

Moscow State University, Moscow, 119899 Russia

** e-mail: suhorukov@imp.uran.ru*

Received May 12, 2003

Abstract—A prototype of the IR radiation modulator operating at $T = 303$ K, using the giant magnetotransmission effect in a $La_{0.82}Na_{0.18}MnO_{3+\delta}$ lanthanum manganite film, has been constructed and the optical characteristics of the setup have been measured. In a wavelength range from 1.4 to 11 μm, the IR modulation depth varies from 3.5 to 6.5%. The possibilities of increasing the modulation depth are considered. © *2003 MAIK "Nauka/Interperiodica".*

The effects of giant magnetotransmission (MT) and significant temperature-induced variation of the intensity of IR radiation transmitted through a manganite crystal near the Curie temperature (T_C), discovered in our recent investigations [1–4], showed that we are dealing with a new group of materials for the IR range whose optical properties can be controlled by the magnetic field and/or temperature. The effects were observed in manganite-based single crystals and epitaxial films of various compositions. The MT magnitude reached several tens of percent, which promised wide applications in optoelectronics, including the creation of magnetic-field-controlled modulators for IR radiation.

Previously, we reported on a strong variation of the IR absorption in a magnetic field (magnetoabsorption) observed in a magnetic semiconducting spinel of the composition $HgCr_2Se_4$ [5]. The magnetoabsorption (or magnetotransmission) in $HgCr_2Se_4$ was explained by peculiarities of the energy band structure related to the interaction of free charge carriers with localized magnetic moments of Cr^{3+} ions. The maximum effect was observed in *n*-$HgCr_2Se_4$ at $T = T_C$ and in *p*-$HgCr_2Se_4$ $T < T_C$. The Curie temperature of $HgCr_2Se_4$ and, hence, the working temperature of the modulator was rather low ($T_C = 115$ K). As is known, the T_C of manganites can vary, depending on the doping, in a temperature range from 80 to 360 K. Therefore, a modulator employing the MT effect can, in principle, operate at room temperature. Below, we describe an IR radiation modulator employing the giant magnetotransmission effect in a $La_{0.82}Na_{0.18}MnO_{3+\delta}$ manganite film, capable of operating in the vicinity of room temperature.

The magnetooptical element of the modulator was made of a 300-nm-thick epitaxial film of $La_{0.82}Na_{0.18}MnO_{3+\delta}$ with a perovskite structure grown by metalorganic chemical vapor deposition (MOCVD) on a single crystal (001)$LaAlO_3$ substrate with a perovskite structure, maintained at a temperature of 750°C. In order to prevent the loss of Na and increase the dopant activity, the synthesis included a stage of annealing for 6 h at 750°C in air in powder with a net composition of $La_{0.3}Na_{0.7}MnO_3$ prepared by chemical homogenization from nitrate solutions. Investigation of the film by the methods of high-resolution transmission electron microscopy, scanning electron microscopy with electron-probe microanalysis, and X-ray diffraction with both φ and ω scanning of the diffraction reflections from film and substrate showed that the material is single-phase and possesses a highly perfect structure. The perovskite structure of the film is characterized by a rhombohedral distortion ($R\bar{3}c$ symmetry group) typical of the bulk materials with compositions $La_{1-x}Na_xMnO_{3+\delta}$ [6]. The surface of the film showed no evidence of foreign phases or other defects.

The choice of the $La_{0.82}Na_{0.18}MnO_{3+\delta}$ film as a material for the magnetooptical element was related to the high Curie temperature of this material, $T_C = 303$ K, which is close to room temperature. The Curie temperature was checked by determining the position of minimum in the first derivative of the temperature dependence of the transverse Kerr effect (TKE, an analog of the temperature dependence of the magnetization). A sharp growth in the TKE signal amplitude in the vicinity of T_C and a large value of TKE in a small field ($H \sim$

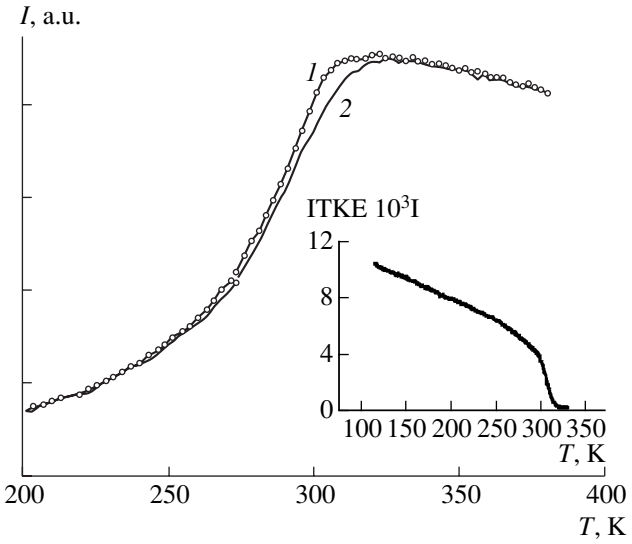

Fig. 1. The temperature dependence of the IR radiation intensity (λ = 8.8 μm) transmitted through a $La_{0.82}Na_{0.18}MnO_{3+\delta}$ film (*1*) without applied magnetic field and (*2*) with a constant magnetic field of 8 kOe. The inset shows the temperature dependence of the transverse Kerr effect measured at an energy of 2.8 eV in a field of 3.5 kOe.

3.5 kOe) at $T \sim 100$ K (see the inset in Fig. 1) are characteristic of ferromagnets. The character of the IR absorption variation in the vicinity of T_C and in an external magnetic field is clearly demonstrated by the temperature dependence of the transmitted radiation intensity measured at a wavelength of λ = 8.8 μm (Fig. 1). A significant increase in the transmission at $T > 200$ K is related to the metal–insulator transition in the film material. The application of a magnetic field (8 kOe) leads to a decrease in the film transmission (Fig. 1, curve *2*). A relative change in the optical transmission under the action of a magnetic field (magnetotransmission) is determined as $MT = (Y_0 - Y_H)/Y_0$, where Y_0 and Y_H are the intensities of radiation transmitted through the magnetooptical element without and with the applied magnetic field, respectively. The absolute value of MT for the film in the vicinity of T_C (T = 303–307 K) reaches ~9% (Fig. 2).

Figure 3 presents the MT spectrum of a $La_{0.82}Na_{0.18}MnO_{3+\delta}$ film measured at $T = T_C$ in a magnetic field of 8 kOe. As can be seen, the film exhibits a large MT in a broad IR wavelength range from 1.4 to 11 μm. The spectral variation of the MT effect, with local maxima at λ ~ 1.7 and 6.5 μm, and the growth at λ > 8 μm are probably related to the magnetic-field-induced changes in the contributions to absorption due to delocalized and localized charge carriers [7].

The main working characteristic of an optical modulator is the modulation depth *m* defined as

$$m = (Y_{max} - Y_{min})/(Y_{max} + Y_{min}) = (Y_H - Y_0)/(Y_H + Y_0),$$

where Y_{max} and Y_{min} are the maximum and minimum intensities of radiation transmitted through the magnetooptical element [8]. The temperature and spectral dependences of *m* for the $La_{0.82}Na_{0.18}MnO_{3+\delta}$ film are similar to the corresponding dependences of MT (cf. Figs. 2 and 3). The modulation depth reaches a maximum of ~4.5% at 303 K, that is, in the vicinity of room temperature. Investigation of the optical properties of

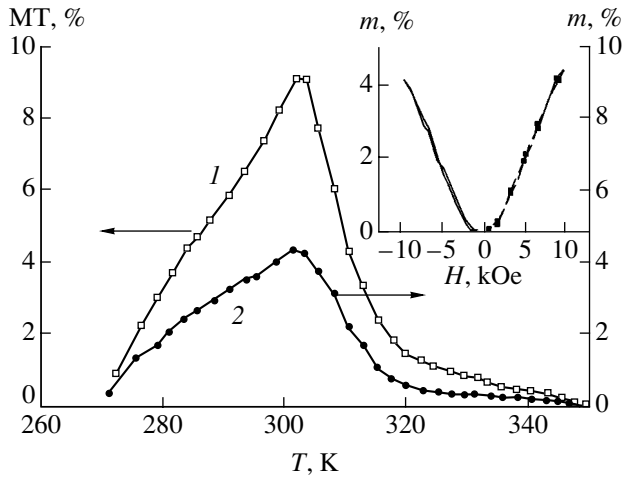

Fig. 2. Temperature dependences of (*1*) magnetotransmission and (*2*) modulation depth for the modulator based on a $La_{0.82}Na_{0.18}MnO_{3+\delta}$ film (H = 8 kOe, λ = 8.8 μm). The inset shows the field dependence of the modulation depth at 303 K in a constant (solid curve) and alternating (points) magnetic field at λ = 8.8 μm.

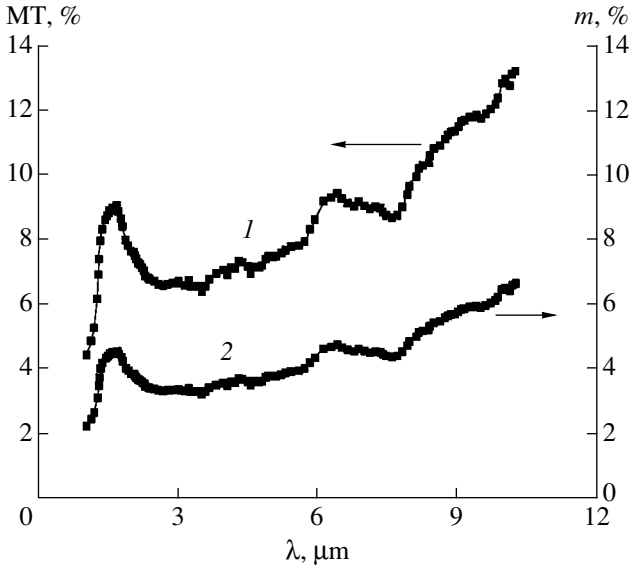

Fig. 3. The spectra of (*1*) magnetotransmission and (*2*) modulation depth for the modulator based on a $La_{0.82}Na_{0.18}MnO_{3+\delta}$ film (H = 8 kOe, T = 303 K).

lanthanum manganites with various compositions showed that it is possible to provide for a significant increase in the modulation depth m of the proposed IR modulator. For example, the m value of a $La_{0.7}Ca_{0.3}MnO_3$ film was ~15% for MT ~ 30% at a temperature close to 0°C [3], while the m value of a $La_{0.35}Pr_{0.35}Ca_{0.3}MnO_3$ film reached ~25% for MT ~ 50% at $T = 175$ K [2].

The MT in manganites is an even effect with respect to the field strength. This is manifested by the fact that the modulated signal frequency is two times that of the source of the alternating magnetic field. The field dependence of m shows that there is a wide interval of magnetic fields in which the modulation depth exhibits linear variation (see the inset in Fig. 2). Since the MT value weakly depends of the magnetic field direction (parallel or perpendicular to the film plane), it is possible to use various geometries of the mutual arrangement of the field source and the magnetooptical element in the modulator.

Measurements of the field dependence of the modulation depth in alternating magnetic fields with a frequency of up to 1 kHz (see points in the inset in Fig. 2) gave the same values of m as those obtained in the constant magnetic field (solid curve in the inset in Fig. 2). The modulation amplitude was measured using a GdHgTe photodetector equipped with an active high-frequency filter with a cutoff frequency of 100 Hz. The operation speed of an optical modulator employing the magnetotransmission effect in lanthanum manganites is determined by rate of magnetization reversal processes. Data on the electromagnetic wave transmission in the manganites $La_{0.67}Pb_{0.33}MnO_3$ (T_C = 347 K) and $La_{0.60}Y_{0.07}Ba_{0.33}MnO_3$ (T_C = 319 K) showed that, at T = 300 K and a constant magnetic field of 3 kOe, an increase in the electromagnetic field frequency up to 10 MHz does not lead to a decrease in magnetoresistance [9]. The rate of manganite remagnetization in an alternating magnetic field is determined by the skin layer thickness $\delta = (2\rho/\omega\mu)^{1/2}$, where ρ is the resistivity of the magnetooptical element, ω is the field frequency, and μ is the magnetic permeability of the magnetooptical element. For $\delta > d$ = 300 nm, the remagnetization frequency of the $La_{0.82}Na_{0.18}MnO_{3+\delta}$ manganite film at T = 303 K can reach ~10^9 Hz for $\mu \le 5$ [9] and $\rho = 10^{-4}\ \Omega$ m. However, there are technical limitations of the modulator operation speed, related to the frequency characteristics of the source of an alternating magnetic field. The source employed in our system allowed the IR radiation to be modulated at frequencies up to several kilohertz.

The proposed IR radiation modulator based on the MT effect in manganites is a very simple optical device comprising a magnetooptical element (manganite film) and a magnetic field source.

Acknowledgments. This study was supported by the Federal Targeted Scientific-Technological Program (project no. 40.012.1.1.1153-7/02), the Russian Foundation for Basic Research (project nos. 02-02-16429, 03-02-06032, and 02-03-33258), and the Russian Academy of Sciences (project "Optical and Magnetotransport Phenomena in Manganites with Colossal Magnetoresistance").

REFERENCES

1. N. N. Loshkareva, Yu. P. Sukhorukov, B. A. Gizhevskii, *et al.*, Phys. Status Solidi A **164**, 863 (1997).
2. Yu. P. Sukhorukov, N. N. Loshkareva, E. A. Gan'shina, *et al.*, Pis'ma Zh. Tekh. Fiz. **25** (14), 6 (1999) [Tech. Phys. Lett. **25**, 551 (1999)].
3. Yu. P. Sukhorukov, E. A. Gan'shina, B. I. Belevtsev, *et al.*, J. Appl. Phys. **91**, 4403 (2002).
4. Yu. P. Sukhorukov, N. N. Loshkareva, E. A. Gan'shina, *et al.*, Zh. Éksp. Teor. Fiz. **123**, 293 (2003) [JETP **96**, 257 (2003)].
5. N. N. Loshkareva, Yu. P. Sukhorukov, B. A. Gizhevskii, *et al.*, Pis'ma Zh. Tekh. Fiz. **15** (17), 83 (1989) [Sov. Tech. Phys. Lett. **15**, 698 (1989)].
6. G. H. Rao, J. R. Sun, K. Barner, *et al.*, J. Phys.: Condens. Matter **11**, 1523 (1999).
7. N. N. Loshkareva, Yu. P. Sukhorukov, E. A. Neifel'd, *et al.*, Zh. Éksp. Teor. Fiz. **117**, 440 (2000) [JETP **90**, 389 (2000)].
8. E. R. Mustel' and V. N. Parygin, *Methods of Light Modulation and Scanning* (Nauka, Moscow, 1970).
9. A. Rinkevich, A. Nossov, V. Ustinov, *et al.*, J. Appl. Phys. **91**, 3693 (2002).

Translated by P. Pozdeev

Technical Physics Letters, Vol. 29, No. 11, 2003, pp. 907–909. Translated from Pis'ma v Zhurnal Tekhnicheskoĭ Fiziki, Vol. 29, No. 21, 2003, pp. 62–67.

Corrugation-Type Instability of the Free Motion of 180° Domain Walls in Uniaxial Ferromagnets

G. E. Khodenkov

Institute of Electronic Control Computers, Moscow, Russia

e-mail: angeline@mtu-net.ru

Received May 7, 2003

Abstract—Investigation of the spectrum of oscillations of a 180° domain wall (DW) freely moving in a uniaxial ferromagnet shows that the one-dimensional structure becomes unstable with respect to surface distortions in the region of negative effective mass (negative differential mobility). The upper critical value of the perturbation wave vector, above which the DW corrugation is not developed and the wave vector of a perturbation mode with the maximum increment are determined. *© 2003 MAIK "Nauka/Interperiodica".*

Development of the information technologies accounts for the interest in investigations of the soliton dynamics in magnetic media. The simplest one-dimensional (1D) object of this kind in uniaxial ferromagnets is a kink representing a 180° domain wall (DW). On the whole, the dynamics of such DWs is rather exhaustively studied (see the Walker solution of 1956 for a DW in an external magnetic field [1] and the Schloemann solution for freely moving DWs [2, 3]). The stability of solutions of the nonlinear Landau–Lifshits equations with respect to development of a corrugation type instability (transverse distortions of the DW surface) has been studied in less detail, although such corrugated DWs are rather frequently observed in experiments. Examples, even restricted to the case of so-called films with a transverse uniaxial magnetic anisotropy, are offered (see [4]) by static distortions of the circular cross section of magnetic bubbles, bending distortions of a plane DW according to Schloemann, dynamic gyrotropic inflection of a DW surface under the action of a moving Bloch line, etc. It should be noted that, judging by these and other experimental data (for plane DWs, see, e.g., [5, 6]), there is no common mechanism responsible for the DW corrugation.

This study addresses the simplest case of corrugation arising on the surface of a one-dimensional 180° DW freely moving in a uniaxial ferromagnet. In other words, we will consider the instability of the Walker solution in the Schloemann form [2, 3]. Doubts concerning the stability of this solution are related to a region with a negative differential mobility of DWs (in terms of [1]) or with a negative effective mass (in terms of [2, 3]). According to the qualitative arguments [7], the 1D motion of DWs in such regions can be unstable with respect to corrugation. This problem was specially studied on a spectral level [8, 9] and it was demonstrated [9] that DWs actually exhibit a corrugation-type instability in the region of negative mobility. Unfortunately, the spectrum presented in [9] is restricted to the case of a linear spatial dispersion with respect to the 2D perturbation wave vector $\mathbf{k}_\parallel$ localized on the DW surface.

In this study, the spectrum of localized oscillations is derived from the spectral equations of stability under not as strong limitations on $\mathbf{k}_\parallel$ as in [9]. This approach will allow us to determine the wavenumber $k_{\parallel M}$ corresponding to a mode with the maximum increment in the region of instability and, hence, determining the period of corrugation. In addition, it will be demonstrated that there is another critical value of $k_\parallel = k_{\parallel b}$ ($>k_{\parallel M}$), above which the DWs remain stable with respect to corrugation.

Consider a 180° DW in the $x0z$ plane, freely moving in a uniaxial ferromagnet in the positive direction of the $0y$ axis (the easy axis is assumed to be collinear with the $0z$ axis). The corresponding 1D problem solution is well known [2, 3] and can be written as

$$\begin{aligned} \sin\theta_0(y) &= 1/\cosh[(y - Vt)/\Delta(\varphi_0)], \\ \Delta(\varphi_0) &= (1 + \sin^2\varphi_0/Q)^{-1/2}, \\ \sin^2\varphi_M &= Q((1 + 1/Q)^{1/2} - 1), \\ V &= \Delta(\varphi_0)\sin\varphi_0\cos\varphi_0/Q. \end{aligned} \tag{1}$$

Here $\theta_0(y)$ and φ_0 = const are the polar and azimuthal angles of the magnetization vector $\mathbf{M}$, respectively, measured from the $0z$ and $0x$ axes (lying in the DW plane); the y coordinate is measured in units of the Bloch DW width $\Delta = (A/K)^{1/2}$, where A is the exchange stiffness and K is the uniaxial anisotropy constant; the time is measured in the units of $(\gamma H_a)^{-1}$, where $H_a = 2K/M$ is the uniaxial anisotropy field; $Q = H_a/4\pi M$ is the so-called quality factor of the material; and $\varphi_M(Q)$ is the value corresponding to the maximum DW veloc-

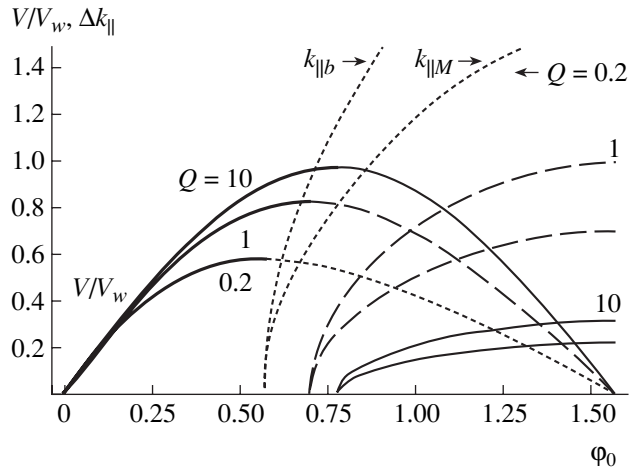

Figure.

ity. Plots of the DW velocity $V(\varphi_0)$ (in the units of $V_w = 2\pi\gamma M\Delta$) for three typical values of Q are presented in the figure, where the regions of stability (see below) are indicated by thick solid lines. The quantity φ_0 has the meaning of the momentum of a DW whose Hamiltonian $H = \Delta(\varphi_0)^{-1}$ is a periodic function of this momentum [10] (in what follows, the consideration can be restricted to the interval $0 < \varphi_0 < \pi/2$). In the descending branches of $V(\varphi_0)$ (see figure), the effective mass m of the DW is negative ($V = \partial H/\partial\varphi_0$ and $1/m = \partial V/\partial\varphi_0 < 0$).

Equations describing the case of small oscillations can be obtained by passing to a local coordinate system moving at the velocity V with the DW along the $0y$ axis. The axes of the new system in the base plane $x0y$ are rotated by the angle φ_0, so that the new $0x$ axis coincides with the plane in which the spins are rotated by 180°. For small amplitudes of magnetization ($\sim\exp(-i\omega t + i\tilde{k}_\parallel\rho)$, where $\rho = (x, z)$ are the coordinates in the DW plane) occurring in the plane of spin rotation ($m_\parallel$) and that perpendicular to this plane ($m_\perp$), we obtain the equations

$$\begin{aligned} i\tilde{\omega}m_\perp + \tilde{V}\hat{L}^+ m_\perp + (\hat{L} + \tilde{k}_\parallel^2)m_\parallel &= 0, \\ -i\tilde{\omega}m_\parallel + \tilde{V}\hat{L}^- m_\parallel + (\hat{L} + \tilde{k}_\parallel^2 + \tilde{\omega}_{ms})m_\perp &= 0, \end{aligned} \tag{2}$$

which coincide to within the notation with the results obtained in [9, 11]. Here, $\hat{L} = \hat{L}^+\hat{L}^- = -d^2/dy^2 + 1 - 2/\cosh^2 y$, $\hat{L}^\pm = \pm d/dy - \tanh y$ are operators, and the local coordinate y implies $(y - V_t)\Delta(\varphi_0)$; $\tilde{\omega} = \omega\Delta(\varphi_0)^2$, $\tilde{k}_\parallel = k_\parallel\Delta(\varphi_0)$, $\tilde{V} = V\Delta(\varphi_0)$, and $\tilde{\omega}_{ms} = Q^{-1}(\varphi_0)\cos 2\varphi_0$ (see formulas in (1)).

The main difficulty encountered in solving Eqs. (2) is related to taking into account the terms proportional to $\sim\tilde{V}$ (the static case of (2) with $\tilde{V} = 0$ is well known, see Winter (1961)). It would be natural to employ the perturbation theory with respect to $\tilde{V}$, expanding Eqs. (2) in terms of the complete orthonormalized basis set of operator $\hat{L}$. The spectrum of this operator consists of two parts: (i) a translation mode $\chi_{tr}(y) = 1/(\sqrt{2}\cosh y)$, $\hat{L}\chi_{tr}(y) = \hat{L}^-\chi_{tr}(y) = 0$ localized on the DW and (ii) a precession mode $\chi_{pr}(y, k) = \hat{L}^+\exp(iky)/\sqrt{2\pi(1 + k^2)}$, $\hat{L}\chi_{pr}(y, k) = (1 + k^2)\chi_{pr}(y, k)$, localized primarily in the domains. According to Eqs. (2), the corresponding resonance frequencies are (i) $\Omega_{tr}^{(0)}(\tilde{k}_\parallel)^2 = \tilde{k}_\parallel^2(\tilde{k}_\parallel^2 + \tilde{\omega}_{ms})$ (translation level) and (ii) $\Omega_{pr}^{(0)}(\tilde{k}_\parallel, k)^2 = (1 + k^2 + \tilde{k}_\parallel^2)(1 + \tilde{k}_\parallel^2 + k^2 + \tilde{\omega}_{ms}) > \Omega_{tr}^{(0)}(\tilde{k}_\parallel)^2$ (precession level).

The corrugation instability is determined on the translation level and the corresponding frequency corrections to $\Omega_{tr}^{(0)}(\tilde{k}_\parallel)$ have to be calculated. The perturbation theory employed here is analogous to the scheme used in [11], where the calculations were restricted to the first order in $\tilde{V}$. Since this approximation corresponds, as demonstrated in [11] and confirmed by our calculations, to the first-order correction $\Omega_{tr}^{(1)}(\tilde{k}_\parallel) = 0$, the refined calculation should include the second-order terms. The contribution of the diagonal term $\tilde{\omega}_{ms}(\varphi_0)$ depending on the DW velocity is taken into account to within the corresponding order of the perturbation theory. The results are as follows:

$$\begin{aligned} m_{\parallel tr}(y) &= \frac{-i\Omega_{tr}^{(0)}(\tilde{k}_\parallel)}{\tilde{k}_\parallel^2} m_{\perp tr}(y) = \chi_{tr}(y) - i\tilde{V}\frac{\tilde{k}_\parallel^2}{\Omega_{tr}^{(0)}(\tilde{k}_\parallel)} \\ &\times \int_{-\infty}^{\infty} dk \frac{(1 + k^2 + \tilde{k}_\parallel^2)\langle\chi_{pr}(y_1, k)|\hat{L}^+|\chi_{tr}(y_1)\rangle}{\Omega_{pr}^{(0)}(\tilde{k}_\parallel, k)^2 - \Omega_{tr}^{(0)}(\tilde{k}_\parallel)^2}\chi_{pr}(y, k); \end{aligned} \tag{3.1}$$

$$\Omega_{tr}(\tilde{k}_\parallel)^2 = \tilde{k}_\parallel^2(\tilde{\omega}_{ms} + \tilde{k}_\parallel^2 - \tilde{V}^2 I(\tilde{k}_\parallel)), \tag{3.2}$$

$$\begin{aligned} I(\tilde{k}_\parallel) &= \int_{-\infty}^{\infty} dk \\ &\times \frac{(1 + k^2 + \tilde{k}_\parallel^2 + \tilde{\omega}_{ms})\left|\langle\chi_{pr}(y_1, k)|\hat{L}^+|\chi_{tr}(y_1)\rangle\right|^2}{\Omega_{pr}^{(0)}(\tilde{k}_\parallel, k)^2 - \Omega_{tr}^{(0)}(\tilde{k}_\parallel)^2} > 0, \end{aligned} \tag{3.3}$$

where $\langle\ldots\rangle$ denotes the operation of determining the matrix element (integrating with respect to y_1 between infinite limits), so that $|\langle\chi_{pr}(y_1, k)|\hat{L}^+|\chi_{tr}(y_1)\rangle|^2 = (\pi/4)(1 + k^2)/\cosh^2(\pi k/2)$.

In the lowest order with respect to $\tilde{k}_\parallel$, Eqs. (3.2) and (3.3) yield (note that $I(0) = 1$ independently of $\tilde{\omega}_{ms}(\varphi_0)$) an expression

$$\begin{aligned}\omega_{tr}(\tilde{k}_\parallel \longrightarrow 0)^2 &= \tilde{k}_\parallel^2(\tilde{\omega}_{ms} - \tilde{V}^2) \\ &= \tilde{k}_\parallel^2 \Delta(\varphi_0)\partial V(\varphi_0)/\partial\varphi_0,\end{aligned} \quad (4)$$

which coincides in the vicinity of the DW velocity maximum (where $\varphi_0 = \varphi_M$) with the results of [9]. This expression shows that, in the region where $\partial V(\varphi_0)/\partial\varphi_0 < 0$ (negative effective mass), the DW becomes unstable with respect to the surface perturbations with $\tilde{k}_\parallel \neq 0$. However, in contrast to [9], the complete expressions (3.2) and (3.3) allow some additional features of the corrugation instability to be determined.

Expansion of the $I(\tilde{k}_\parallel)$ integral into series in $\tilde{k}_\parallel$ shows that the terms on the order of $\tilde{k}_\parallel^4$ in (3.2) are always positive. With allowance for (4), this fact indicates that there exists a certain value $k_\parallel = k_{\parallel M}$ for which the increment of the corrugation instability reaches maximum and, hence, determines the most probable value of the steady-state corrugation period. At the same time, since $\Omega_{tr}(\tilde{k}_\parallel = 0)^2 = 0$ and $\Omega_{tr}(\tilde{k}_\parallel \longrightarrow \infty)^2 \sim \tilde{k}_\parallel^4$ (for $I(\tilde{k}_\parallel \longrightarrow \infty) \longrightarrow$ const), we may conclude that there is another critical value of $k_\parallel = k_{\parallel b}$ (besides $k_\parallel = 0$), at which $\Omega_{tr}(\tilde{k}_{\parallel b})^2 = 0$ and above which $\Omega_{tr}(\tilde{k}_\parallel)^2$ is always positive (i.e., the corrugation disappears). The figure presents three pairs of the $k_{\parallel M}(\varphi_0)$ and $k_{\parallel b}(\varphi_0)$ curves (numerically calculated for $Q = 0.2$, 1, and 10) originating from the points $\varphi_M(Q)$ on the abscissa axis (for a given Q, $k_{\parallel b}(\varphi_0)$ is situated above $k_{\parallel M}(\varphi_0)$).

As for the applicability of the perturbation theory, it is known that this requires the first-order correction in Eq. (3.1) to be small. In the case of $Q \gg 1$, this correction can be shown to always be small ($\sim 1/Q$). The case of $Q \ll 1$ is more problematic: except for separate regions, the smallness of the first-order correction depends on the smallness of $k_\parallel$.

REFERENCES

1. N. L. Schryer and L. R. Walker, J. Appl. Phys. **45**, 5406 (1974).
2. E. Schloemann, Appl. Phys. Lett. **19** (8), 274 (1971).
3. E. Schloemann, J. Appl. Phys. **43**, 3834 (1972).
4. A. P. Malozemoff and J. C. Slonczewski, *Magnetic Domain Walls in Bubble Materials* (Academic, New York, 1979; Mir, Moscow, 1982).
5. V. V. Randoshkin and M. V. Logunov, Fiz. Tverd. Tela (St. Petersburg) **36**, 3498 (1994) [Phys. Solid State **36**, 1858 (1994)]; V. V. Randoshkin, Fiz. Tverd. Tela (St. Petersburg) **37**, 3056 (1995) [Phys. Solid State **37**, 1684 (1995)].
6. A. A. Bokov, V. V. Volkov, and N. A. Petrichenko, Fiz. Tverd. Tela (St. Petersburg) **44**, 2018 (2002) [Phys. Solid State **44**, 2112 (2002)].
7. J. C. Slonczewski, Int. J. Magn. **2** (2), 85 (1972).
8. E. Magyari and H. Thomas, Z. Phys. B: Condens. Matter **57**, 141 (1984).
9. E. Magyari and H. Thomas, Z. Phys. B: Condens. Matter **59**, 167 (1985).
10. A. A. Kosevich, B. A. Ivanov, and A. S. Kovalev, *Nonlinear Magnetization Waves: Dynamical and Topological Solitons* (Naukova Dumka, Kiev, 1988).
11. A. A. Thiele, Phys. Rev. B **7**, 391 (1973).

Translated by P. Pozdeev

Technical Physics Letters, Vol. 29, No. 11, 2003, pp. 910–912. Translated from Pis'ma v Zhurnal Tekhnicheskoĭ Fiziki, Vol. 29, No. 21, 2003, pp. 68–73.

Strain-Induced Magnetization of Amorphous Ferromagnets

A. A. Gavrilyuk, A. L. Petrov, Z. L. Yarycheva, and S. M. Zubritsky*

Irkutsk State University, Irkutsk, Russia

** e-mail: zubr@api.isu.ru*

Received May 7, 2003

Abstract—The magnitude of the strain-induced magnetization (ΔB_σ effect) of a $Fe_{81.5}B_{13.5}Si_3C_2$ amorphous ferromagnetic alloy was studied as a function of the applied magnetic field, the frequency of alternating elastic stress, and the thermomagnetic treatment temperature. It is shown that processes involved in the strain-induced magnetization of the alloy studied are determined by the frequency of alternating elastic stress and the thermomagnetic treatment temperature. *© 2003 MAIK "Nauka/Interperiodica".*

As is known, the application of alternating elastic stresses to iron-based amorphous ferromagnetic alloys leads to the so-called strain-induced magnetization of samples (ΔB_σ effect). The magnitude of this effect depends on the induced uniaxial anisotropy, initial permeability, etc. [1, 2]. From the standpoint of practical applications, one of the most promising amorphous ferromagnetic materials is a high-magnetostriction alloy of the $Fe_{81.5}B_{13.5}Si_3C_2$ type obtained by rapid quenching of the melt [3].

This study was aimed at determining the dependence of the ΔB_σ effect in the $Fe_{81.5}B_{13.5}Si_3C_2$ alloy on the thermomagnetic treatment temperature, the applied magnetic field strength H, and the frequency f of alternating elastic stresses.

Samples in the form of 50-mm-long strips with a width of 1 mm and a thickness of 25 μm were cut from the amorphous alloy ribbons along the rolling direction. Prior to measurements, the samples were subjected to a thermomagnetic treatment (TMT) in order to relieve residual stresses and induce a uniaxial anisotropy. The TMT was performed for 20 min in the temperature range T = 360–450°C in a vacuum of 10^{-6} Torr. A magnetic field of 40 kA/m was applied in the sample plane perpendicular to the long axis. The TMT temperature interval was chosen to correspond to the maximum magnetoelastic characteristics of the $Fe_{81.5}B_{13.5}Si_3C_2$ alloy [4].

A sample with measuring induction coil was fixed with one end in a sample holder, while the other end was connected with a hard filament to a piezoelectric crystal producing alternating elastic stresses with an amplitude of $\sigma \approx 5 \times 10^6$ Pa in a range of frequencies from 5 to 100 kHz. The piezoelectric transducer was powered from a sinusoidal current generator. The sample was placed in a system of Helmholtz coils creating a constant magnetic field with the strength variable from H = 0 to 2250 A/m.

In order to measure the sample response signal, the induction coil was connected to a lock-in amplifier tuned to the same frequency as the master generator. The strain-induced magnetization was measured by a change in the induction determined as [5]

$$\Delta B_\sigma = \frac{U}{4 f \omega S}, \qquad (1)$$

where f is the oscillation frequency of the piezoelectric transducer, ω is the number of turns of the induction coil, S is the area of the sample cross section, and U is the amplitude of the signal measured at the coil output.

The ΔB_σ value is virtually independent of the TMT temperature in the interval from 360–450°C and amounts to $(6–7.5) \times 10^{-2}$ T. In the frequency interval f = 5–25 kHz, the ΔB_σ value decreases with increasing field strength H, this behavior being typical of all samples irrespective of the TMT temperature. In the interval of frequencies from 40 to 60 kHz, the character of the $\Delta B_\sigma(H)$ function changes (Figs. 1 and 2) and the curve exhibits a maximum. As the TMT temperature varies from 380 to 430°C, the maximum on the $\Delta B_\sigma(H)$ curve measured at 40 kHz shifts to higher fields H, while that on the curve corresponding to $f \approx 60$ kHz shifts to lower H. For the samples treated at T = 450°C, the $\Delta B_\sigma(H)$ curve measured at $f \approx 80$ kHz exhibits a maximum for $H \approx 2000$ A/m, in which the ΔB_σ effect reaches $\approx 3.5 \times 10^{-2}$ T.

The TMT of the amorphous alloy samples leads to the appearance of an easy magnetization axis perpendicular to the long axis of the stripe. The magnitude of the ΔB_σ effect under the action of stress σ in the magnetic field H can be expressed as

$$\Delta B_\sigma(H, \sigma) = B(H, \sigma) - B(H, \sigma = 0), \qquad (2)$$

where $B(H, \sigma) = B_S^2 H/(2K - 3\lambda_S\sigma)$, $B(H, \sigma = 0) =$

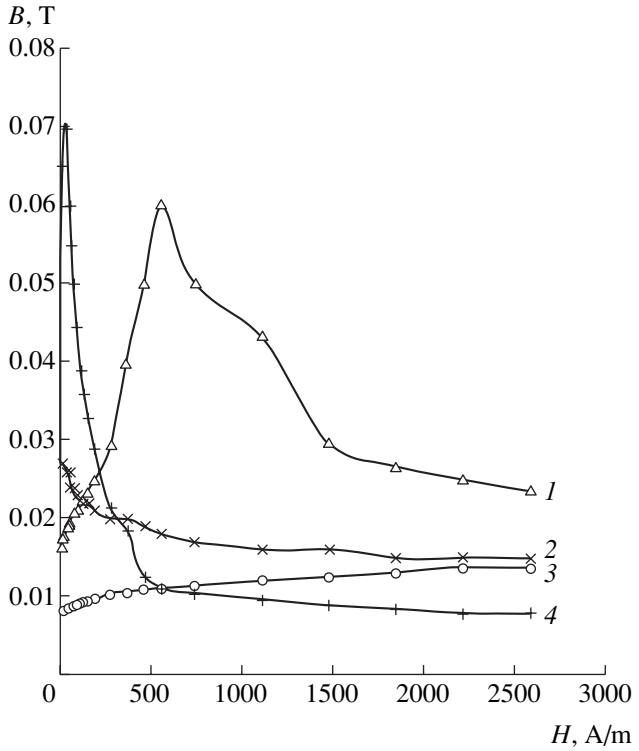

Fig. 1. Plots of the magnetic induction increment ΔB_σ versus magnetic field strength H measured at $f = 60$ (*1*), 10 (*2*), 90 (*3*), and 40 kHz (*4*) for the $Fe_{81.5}B_{13.5}Si_3C_2$ amorphous ferromagnetic alloy after a TMT at $T = 380$°C.

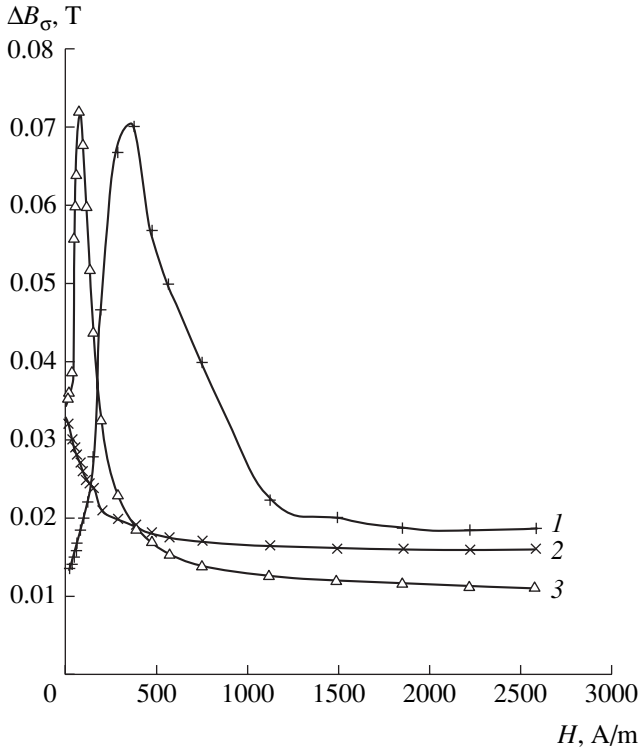

Fig. 2. Plots of the magnetic induction increment ΔB_σ versus magnetic field strength H measured at $f = 60$ (*1*), 10 (*2*), and 40 kHz (*3*) for the $Fe_{81.5}B_{13.5}Si_3C_2$ amorphous ferromagnetic alloy after a TMT at $T = 430$°C.

$B_S^2 H/2K$, B_S is the saturation induction, K is the constant of the induced uniaxial anisotropy, and λ_S is the magnetostriction constant. A change in the magnetic induction under the action of stress σ is

$$\Delta B_\sigma = 3\lambda_S \sigma B_S^2 H/(2K(2K - 3\lambda_S\sigma)). \quad (3)$$

According to formula (3), the ΔB_σ value monotonically increases with the field strength H. It should be noted that Eq. (2) is valid under the condition $2K > 3\lambda_S\sigma$. For $\sigma > 2K/3\lambda$, Eq. (2) becomes inapplicable because even a small field H (below the induced anisotropy field) leads to saturation of the sample. Here, the ΔB_σ effect obeys the relation

$$\Delta B_\sigma = B_S - (B_S^2 H/(3\lambda_S\sigma - 2K)). \quad (4)$$

According to formula (4), the value of ΔB_σ must exhibit a monotonic decrease with increasing H. For the stress applied during our measurements ($\sigma \approx 5 \times 10^6$ Pa) and $\lambda_S \approx 3 \times 10^{-5}$, we obtain $3\lambda_S\sigma/2 \approx 225$ J/m^3, which is close to the value of $K \sim 170$–250 J/m^3. Therefore, the rotation of magnetization in the presence of such stresses terminates even in small fields H, while further increase of the applied field strength will lead to a decrease in ΔB_σ.

Let us consider the factors that may account for the appearance of maxima in $\Delta B_\sigma(H)$ measured at $f \approx 40$–60 kHz. The strain-induced magnetization in high-magnetostriction ferromagnets involves, besides the magnetization rotation, the motion of non-180° domain walls [1, 6]. In the iron-based amorphous ferromagnetic alloys with induced uniaxial anisotropy, there are two possible types of non-180° domain walls [7]. The first type is related to the formation of terminal domains with reverse magnetization in the main band domains. Upon application of the stress σ and a magnetic field with strength H above the coercive force of the domain walls, the terminal domains begin to grow by mechanism of displacement. We may suggest that the displacement of such domain walls is the main factor contributing to the ΔB_σ value at $f = 40$–50 kHz.

At higher frequencies f, the domain boundaries cannot timely change their positions because of inertia and the contribution to ΔB_σ related to the aforementioned wall displacement decreases. Non-180° domain walls of another type occur in the regions of internal compressive stresses, where a local anisotropy caused by the applied stress is higher than the anisotropy induced by the TMT. This accounts for a high natural oscillation frequency in these regions. The maximum of $\Delta B_\sigma(H)$, observed in the fields greater than the induced uniaxial anisotropy field at $f \approx 60$ kHz, can be related to the dis-

placement of such domain walls. This assumption is confirmed by a shift of the ΔB_σ maximum at $f \approx 60$ kHz toward lower H when the TMT temperature is increased from 360 to 430°C. This behavior can be explained by relaxation of the internal compressive stresses in the amorphous alloy. It can be also suggested [8] that, when the frequency f increases above 60–70 kHz, the inertial domain walls occurring in the regions of compressive stresses cannot rearrange in response to σ and their contribution to the ΔB_σ value decreases.

In conclusion, various mechanisms of the strain-induced magnetization differently depend on the applied magnetic field strength, the frequency of alternating elastic stresses, and the TMT temperature of the iron-based amorphous ferromagnetic alloy studied. When the applied elastic stress is close to or greater than $\sigma = 2K/3\lambda_S$, the main mechanisms contributing to the ΔB_σ effect are related to the displacement of non-180° domain walls.

REFERENCES

1. I. B. Kekalo, O. Yu. Nemova, and V. E. Taranichev, Izv. Ross. Akad. Nauk, Ser. Fiz. **57** (11), 188 (1993).
2. V. E. Taranichev and M. N. Alenov, Metallofizika (Kiev) **13** (10), 84 (1991).
3. A. A. Gavrilyuk, A. V. Gavrilyuk, and N. P. Kovaleva, Zh. Tekh. Fiz. **69** (6), 50 (1999) [Tech. Phys. **44**, 653 (1999)].
4. V. I. Boldyrev, A. S. Veksler, A. A. Gavrilyuk, *et al.*, Izv. Vyssh. Uchebn. Zaved., Fiz., No. 9, 46 (1999).
5. *Electrical Measurements*, Ed. by A. V. Fremke (Énergiya, Moscow, 1980).
6. V. E. Taranichev and O. Yu. Nemova, Fiz. Tverd. Tela (St. Petersburg) **38**, 2083 (1996) [Phys. Solid State **38**, 1149 (1996)].
7. J. D. Livingston and G. Morris, J. Appl. Phys. **57**, 3555 (1985).
8. H. Kronmuller and W. Fernengel, Phys. Status Solidi A **64**, 593 (1981).

Translated by P. Pozdeev

Technical Physics Letters, Vol. 29, No. 11, 2003, pp. 913–916. Translated from Pis'ma v Zhurnal Tekhnicheskoĭ Fiziki, Vol. 29, No. 21, 2003, pp. 74–81.

Current–Voltage Characteristics of Nanodimensional Normal Metal–Superconductor Point Diffusion Junctions

I. N. Askerzade

Institute of Physics, National Academy of Sciences of Azerbaijan, Baku, Azerbaijan
Department of Physics, Ankara University, 06100 Tangodan, Ankara, Turkey
e-mail: solstphs@physics.ab.az; iasker@science.ankara.edu.tr
Received April 2, 2003; in final form, June 4, 2003

Abstract—The differential conductivity of nanodimensional normal metal–superconductor (NS) point diffusion junctions has been calculated with allowance for partial breakage of the superconducting state by the intrinsic current in the superconducting electrode and for the Andreev reflection at the adaptive N'S interface. Dependence of the excess current and the differential conductivity on the applied voltage are considered. © *2003 MAIK "Nauka/Interperiodica".*

The point junction spectroscopy employing the Andreev reflection [1] is based on the transformation of quasiparticles into Cooper pairs that takes place over a distance on the order of the coherence length ξ at the boundary between a normal metal (N) and a superconductor (S) [2]. The NS junction is characterized by the direct (nontunneling) conductivity and is considered as a point contact if its radius r_0 is much smaller than the coherence length ξ in the superconductor and the electron mean free path l_N in the metal ($r_0 \ll \xi, l_N$). The electron transfer phenomena in the NS junctions were originally described by Artemenko *et al.* [3], Zaitsev [4], and by the Blonder–Tinkham–Klapwjik (BTK) theory [5].

The condition that $r_0 \ll \xi, l_N$ implies applicability of the ballistic approach. The conductivity of the NS junction was originally calculated by Sharvin [6]. The theory of diffusion NS junctions with $r_0 \le l_N$ was developed in [3], where it was demonstrated for the first time that $G_{NS} = G_{NN}$. In contrast, the ratio of conductivities inside and outside the gap is $G_{NS}/G_{NN} = 2$ [5]. The results of microjunction investigations for the materials with small mean free paths l_N give a smaller value for the G_{NS}/G_{NN} conductivity ratio [7]. According to the results of recent measurements, the typical dimensions of diffusion contacts are estimated at $r_0 =$ 5–60 nm [8, 9]. In connection with development of the technology of reproducible nanodimensional point contacts [10], it is important to elaborate a theory for the materials with small mean free path lengths l_N (diffusion regime).

As soon as the contact radius becomes comparable with the coherence length ξ, nonequilibrium phenomena arise in the NS junctions. This leads to suppression of the order parameter as a result of (i) nonequilibrium distribution of the high-energy electrons and phonons, (ii) penetration of the magnetic vortices, generated by the intrinsic current, into the junction, and (iii) heating of the contact region. A number of interesting peculiarities in the current–voltage characteristics of Ag/Ta junctions were reported by Hahn [11]. In order to explain these experimental results, a nonequilibrium theory of point junctions of the NcN'S type was developed in [12]. According to this theory, phonons appearing in the junctions featuring the injection of high-energy quasiparticles lead to the formation of a nonequilibrium region. The radius of this region increases with the applied voltage. However, this theory did not provide an explicit expression for the excess current. Another variant of a model for the NcN'S junctions in cuprate superconductors with allowance for the different order parameters in the junction region and in the superconductor volume was proposed in [13]. The possible heating of the junction region at high applied voltages was considered in [14].

Let us consider a model of the NS junction representing a contact between two metal electrodes separated by an impermeable screen with a circular contact region of radius r_0 and an area of $4\pi r_0^2$ (Fig. 1). The right-hand part of the junction represents a superconductor with isotopic pairing. It is natural to expect for nanodimensional contacts that (even at a moderate applied voltage) the superconducting state in the right-hand electrode will be broken by the intrinsic current (which exceeds the depairing current j_0). Let us assume that the front of superconductivity violation in the right-hand electrode propagates as a sphere with the

1063-7850/03/2911-0913$24.00 © 2003 MAIK "Nauka/Interperiodica"

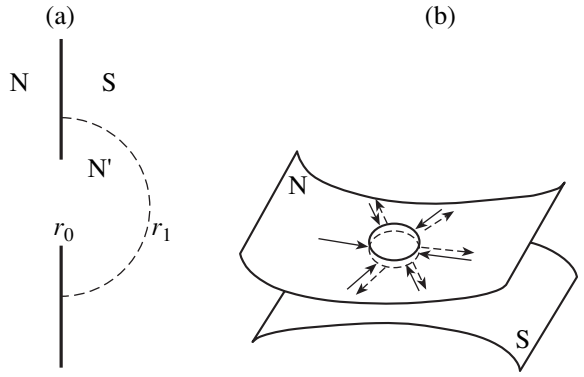

Fig. 1. (a) A schematic diagram of the normal metal–superconductor (NS) contact (hyperbolic bridge; dashed curve shows the propagating N'S interface); (b) a 2D diagram of the spherical spreading model.

radius r_1 (adaptive N'S interface) and is determined by the current I passing through the junction (Fig. 1). Analogous model for the Josephson point contact developed in [15] is commonly referred to as the spherical spreading model. This variant represents a limiting case of the hyperbolic contact for $\Delta z \longrightarrow 0$ [16].

For small applied voltages, $V < V_c = \Delta/e$ (where Δ is the energy gap of the superconductor), the voltage drop in the left-hand part of the junction is $V_1 = R_1 I$, where R_1 is the resistance calculated as described below. When the current density in the junction reaches the depairing threshold j_0 [17], the total current is $I_0 = 4\pi r_0^2 j_0$ and the radius of the adaptive interface for $I > I_0$ is determined as $r = (I/4\pi j_0)^{1/2}$. In the right-hand part, the voltage drop is calculated as $V_2 = R_2 I$, where R_2 is the resistance of this part upon a partial loss of superconductivity. According to the Ohm law,

$$V_2 = \int_{r_0}^{r_1} E dr = \frac{I\rho_2}{2\pi}\int_{r_0}^{r_1}\frac{dr}{r^2} = \frac{I\rho_2}{2\pi}(r_0^{-1} - r_1^{-1}), \qquad (1)$$

where ρ_2 is the resistivity of the right-hand electrode in the normal state. An analogous expression for the left-hand electrode with $r_1 \longrightarrow \infty$ yields $R_1 = \frac{\rho_1}{2\pi} r_0^{-1}$. For the total voltage drop $V = V_1 + V_2$, we obtain

$$V = R_M I - \frac{\rho_2 (4\pi j_0 I)^{1/2}}{2\pi}, \qquad (2)$$

where $R_M = (\rho_1 + \rho_2)(1 + Z^2)/2\pi r_0$ is the so-called Maxwell resistance (Z is a dimensionless parameter characterizing the amplitude of the δ-like potential at the interface). Equation (2) can be rewritten as

$$i = \frac{\rho_1 v}{\rho_1 + \rho_2} + \left(\frac{\rho_2}{\rho_1 + \rho_2}\right)^2 \times \left\{1 + \left[1 + 2\left(\left(\frac{\rho_1}{\rho_2}\right)^2 + \frac{\rho_1}{\rho_2}\right)v\right]^{1/2}\right\}, \qquad (3)$$

where $i = I/I_0$, $v = V/V_c$, and $V_c = R_1 I_0 (1 + Z^2)$. As can be seen from formula (3), an excess current related to the superconductivity breakage in the right-hand part exists even in the absence of the Andreev reflection. Accordingly, the differential conductivity is

$$\frac{G_{NS}}{G_{NN}} = \frac{di}{dv} = \frac{\rho_1}{\rho_1 + \rho_2}\left[1 + \frac{1}{\left(1 + 2\left(\frac{\rho_1^2}{\rho_2^2} + \frac{\rho_1}{\rho_2}\right)v\right)^{1/2}}\right]. \qquad (4)$$

With allowance of the Andreev reflection at the N'S interface [5], formula (4) can be rewritten as follows (assuming that the barrier height at this interface is zero):

$$\frac{G_{NS}}{G_{NN}} = \begin{cases} 2, & v < 1 \\ \dfrac{\rho_1}{\rho_1 + \rho_2}\left[1 + \dfrac{1}{\left(1 + 2\left(\dfrac{\rho_1^2}{\rho_2^2} + \dfrac{\rho_1}{\rho_2}\right)v\right)^{1/2}}\right. & \\ \left. + \dfrac{1 - (1 - v^{-2})^{1/2}}{1 + (1 - v^{-2})^{1/2}}\right], & v > 1. \end{cases} \qquad (5)$$

Here, the last term in square brackets reflects the Andreev reflection [5]. As can be seen from formula (5), the Andreev term decays for $v \gg 1$ as v^{-2} and the conductivity is determined by the non-Andreev contribution. Therefore, the differential conductivity for $v \gg 1$ depends primarily on the ratio of resistivities $\kappa = \rho_1/\rho_2$.

It was shown [5] that the excess current on the N'S interface for $Z = 0$ is given by the formula

$$I_{exc} = \frac{1}{eR_M}\int_0^\infty A(E) dE = \frac{\pi\Delta}{2eR_M},$$

where $A(E)$ is the probability of the Andreev reflection. In the general case, an expression for the excess current is as follows:

$$I_{\text{exc}} = \frac{\pi\Delta}{2eR_{\text{M}}} + I_0\left(\frac{\rho_2}{\rho_1+\rho_2}\right)^2 \times\left\{1+\left[1+2\left(\left(\frac{\rho_1}{\rho_2}\right)^2+\frac{\rho_1}{\rho_2}\right)v\right]^{1/2}\right\}. \quad (6)$$

Figure 2 shows the current–voltage characteristics calculated for various barrier heights Z at $\kappa \approx 1$. As can be seen, the dependence of current on the voltage in the tunneling junctions with $Z = 50$ rapidly acquires an ohmic character, while the contacts with direct conductivity (small Z) are characterized by a linear relationship of the type $I(V) = G_{\text{NN}}V + I_{\text{exc}}(V)$. As the barrier height grows, the excess current drops and completely vanishes for the tunneling junction. The latter fact is related to the Andreev reflection, which is present in the junctions with direct conductivity but is absent in tunneling junctions. Experimental data confirming the absence of excess current in the tunneling NS and SNS junctions can be found in [10, 18].

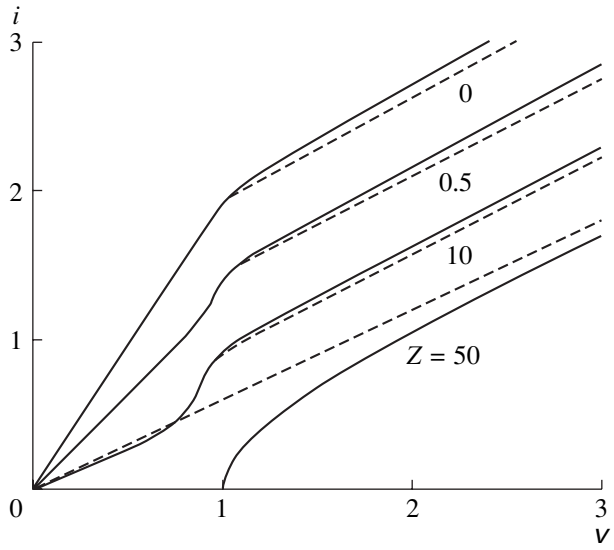

Fig. 2. Current–voltage characteristics of point NS junctions calculated for various values of the barrier height Z at $\kappa \approx 1$ and a zero temperature. Dashed curves show the results of calculations within the framework of the Blonder–Tinkham–Klapwjik theory; the bottom dashed line corresponds to the NN' junction.

In principle, the problem of description of the conductivity in a contact of two metals with different masses and free paths of the charge carriers and other physical properties has not yet been solved. In the general case, the conductivity of a microcontact of different metals should be considered using the scheme of Landauer or within the framework of the Boltzmann approximation [19]. An attempt to calculate the excess current in a periodic system with NS interfaces was made in [20]. The theory is consistent with the experiments reported in [21]. However, the question as to how the conductivity of metals influences the current–voltage characteristic and the differential conductivity still remains open. From this standpoint, it is of interest to study a nonballistic NS junction with different electrodes. In the proposed phenomenological model, the difference between metals is characterized by the parameter κ. This parameter strongly influences the non-Andreev excess current. In the limiting case of $\kappa \longrightarrow \infty$, only a contribution due to the Andreev reflection is retained, while for $\kappa \longrightarrow 0$, the non-Andreev excess current (in units of I_0) is constant and approximately equal to 1. When $\kappa \longrightarrow 1$, the excess current exhibits a twofold increase only for very large voltages ($v \approx 14$). As can be seen from formula (5) for $\kappa \longrightarrow \infty$, the ratio of conductivities inside and outside the gap is 2, which is in agreement with predictions of the BTK theory [5]; for $\kappa \approx 1$, this ratio is below 2. Further increase in the parameter κ leads to an increase in the ratio of conductivities inside and outside the gap of the nonballistic junction.

In conclusion, the current–voltage characteristic of small-size NS junctions was calculated and it was demonstrated that the excess current consists of two contributions: the Andreev contribution due to the adaptive N'S interface and the non-Andreev contribution related to breakage of the superconductivity by the intrinsic current in the superconducting electrode. Generalized formulas for the excess current and the differential conductivity as functions of the applied voltage are derived. It is shown that the ratio of conductivities inside and outside the gap, $G_{\text{NS}}/G_{\text{NN}}$, is determined by the parameter κ and can be either equal to 2 (in agreement with the BTK theory) or smaller than 2.

Acknowledgments. The author is grateful to Prof. I.O. Kulik for fruitful discussion of results.

REFERENCES

1. I. K. Yanson, Fiz. Nizk. Temp. **9**, 676 (1983) [Sov. J. Low Temp. Phys. **9**, 343 (1983)].
2. A. F. Andreev, Zh. Éksp. Teor. Fiz. **46**, 1823 (1964) [Sov. Phys. JETP **19**, 1228 (1964)].
3. S. N. Artemenko, A. F. Volkov, and A. V. Zaitsev, Solid State Commun. **30**, 771 (1979).
4. A. V. Zaĭtsev, Zh. Éksp. Teor. Fiz. **78**, 221 (1980) [Sov. Phys. JETP **51**, 111 (1980)].
5. G. E. Blonder, M. Tinkham, and T. M. Klapwjik, Phys. Rev. B **25**, 4515 (1982).
6. Yu. V. Sharvin, Zh. Éksp. Teor. Fiz. **48**, 984 (1965) [Sov. Phys. JETP **21**, 655 (1965)].
7. I. K. Yanson, Fiz. Nizk. Temp. **9**, 676 (1983) [Sov. J. Low Temp. Phys. **9**, 343 (1983)].
8. L. F. Rybaltchenko, A. G. M. Jansen, P. Wider, *et al.*, Physica C **319**, 189 (1999).

9. F. Laube, G. Goll, H. von Lohneyesen, and F. Lichtenberg, J. Low Temp. Phys. **117**, 1575 (1999).
10. I. K. Yanson, in *Quantum Mesoscopic Phenomena and Mesoscopic Devices in Microelectronics*, Ed. by I. O. Kulik and R. Ellialtioglu (Kluwer, Dordrecht, 2000), pp. 61–77.
11. A. Hahn, Phys. Rev. B **31**, 2816 (1985).
12. A. Hahn and K. Humpfner, Phys. Rev. B **51**, 3660 (1995).
13. M. Belogolovski, M. Grajcar, P. Kus, *et al.*, Phys. Rev. B **59**, 9617 (1999).
14. V. A. Khlus and A. N. Omelyanchuk, Fiz. Nizk. Temp. **9**, 373 (1983) [Sov. J. Low Temp. Phys. **9**, 189 (1983)].
15. I. O. Kulik and A. N. Omelyanchuk, Zh. Éksp. Teor. Fiz. **68**, 2139 (1975) [Sov. Phys. JETP **41**, 1071 (1975)].
16. E. N. Bogachek, A. G. Sherbakov, and U. Landman, Phys. Rev. B **56**, 14917 (1997).
17. A. A. Abrikosov, *Fundamentals of the Theory of Metals* (Nauka, Moscow, 1987; North-Holland, Amsterdam, 1988).
18. K. K. Likharev, *Introduction to the Dynamics of Josephson Junctions* (Nauka, Moscow, 1985).
19. I. O. Kulik, in *Quantum Mesoscopic Phenomena and Mesoscopic Devices in Microelectronics*, Ed. by I. O. Kulik and R. Ellialtioglu (Kluwer, Dordrecht, 2000), pp. 3–22.
20. S. N. Artemenko, A. F. Volkov, and A. V. Sergeev, J. Low Temp. Phys. **44**, 405 (1981).
21. Yu. G. Bevza and A. V. Lukashenko, Fiz. Nizk. Temp. **9**, 368 (1983) [Sov. J. Low Temp. Phys. **9**, 186 (1983)].

Translated by P. Pozdeev

Technical Physics Letters, Vol. 29, No. 11, 2003, pp. 917–919. Translated from Pis'ma v Zhurnal Tekhnicheskoĭ Fiziki, Vol. 29, No. 21, 2003, pp. 82–87.

The Effect of γ Radiation on the Properties of *p–n–p* Structures Based on Polycrystalline Cadmium Telluride

Zh. Zhanabergenov, Sh. A. Mirsagatov, S. Zh. Karazhanov, and S. Muzaffarova

Physicotechnical Institute, Academy of Sciences of the Republic of Uzbekistan, Tashkent, Uzbekistan

e-mail: Smag@physic.uzsci.net

Received May 5, 2003

Abstract—The parameters of *p–n–p* structures based on polycrystalline cadmium telluride films exhibit nonmonotonic variation with increasing doses of γ radiation. It is established that this behavior is related to an increase in the base thickness and to a nonmonotonic dose dependence of the minority carrier lifetime, which is accompanied by recharge of the surface states and a by a change in the potential barrier height at the grain boundaries. © *2003 MAIK "Nauka/Interperiodica".*

Investigations of the radiation-induced phenomena in semiconductor devices are of considerable basic and applied interest, including elucidation of the mechanisms, determination of the results (as manifested by modified electrical properties), and the search for methods to decrease the response to such a perturbative action. The radiation-induced phenomena are frequently related to the appearance of deep defects in semiconductors.

Baruch [1] reported on a nonmonotonic variation of the short-circuit current (J_{sc}) in Si- and Ge-based solar cells irradiated to increasing doses D. Later, analogous dependence of the current on the radiation dose (called anomalous degradation) was observed by Yamaguchi *et al.* [2–4] in silicon-based n^+–p–p^+ solar cell structures. The decrease and subsequent increase of J_{sc} depending on D were referred to as the normal and anomalous degradation processes, respectively. The anomalous degradation was explained in terms of expansion of the space charge region.

It should be noted that similar nonmonotonic dependence of J_{sc} on the concentration of deep traps (N_t) was revealed by theoretical investigation of a contribution of the impurity photovoltaic effect to the efficiency of solar energy conversion [5]. The increase in J_{sc} with N_t was attributed to a growth in the rate of charge carrier photoemission from the impurity level. Recently, it was shown [6] that both phenomena are of the same nature, being related to an increase in the minority carrier lifetime with a growing degree of compensation in the semiconductor that can take place even in the absence of the photoexcitation of impurities. Below we report on the analogous phenomenon in the *p–n–p* structures based on polycrystalline cadmium telluride, irradiated by γ quanta.

The experiments were performed on CdTe-based *p–n–p* structures of two types prepared as described in [7] with the base resistivities $\rho = 10^4$ and 10^5 Ω cm. The emitter region contains 90% of gold and 10% of antimony. The *n*-type conductivity of the high-ohmic CdTe base is due to the presence of excess Cd atoms. The samples were irradiated at $T = 50$°C with γ quanta of $E \approx 1.2$ MeV energy from a Co^{60} source at a rate of 1700 rad/s in a range of doses $\leq 1.6 \times 10^{18}$ cm^{-2}. The initial CdTe films possessed a columnar polycrystalline structure with a grain size not smaller that the film thickness.

Figure 1a shows the ratio of the collector currents of irradiated (J_r) and unirradiated (J_0) semiconductor structures as a function of dose D. As can be seen, J_r/J_0 decreases with increasing D in the region of small doses. Then, the current ratio begins to increase, passes through a maximum, and decreases again. The J_r value in the structure possessing a higher resistivity of the base exhibits the minimum at a lower dose than does the sample with a smaller resistivity. This fact indicates that dopants determining the conductivity type are involved in the formation of deep recombination levels.

In order to elucidate the nature of the observed nonmonotonic variation, we have studied the dose dependence of the minority carrier lifetime τ_p in the base. Figure 1b shows the plots of $\tau_p(D)$ determined from the results of measurements of the limiting frequency $f = 2.43D_p/(2\pi W^2)$ and the gain $\beta = 2D_p\tau_p/W^2$ in the scheme with common emitter (D_p is the hole diffusion coefficient in the base region, W is the base thickness). As can be seen, the dose dependences of J_r and τ_p are correlated, which is consistent with the explanation proposed in [6]. Therefore, the minority carrier lifetime τ_p is a factor determining the nonmonotonic character of the collector current variation with the dose of γ radiation in the region of small and medium doses. The values of τ_p in the samples with different resistivities are different as well. These results confirm the above

1063-7850/03/2911-0917$24.00 © 2003 MAIK "Nauka/Interperiodica"

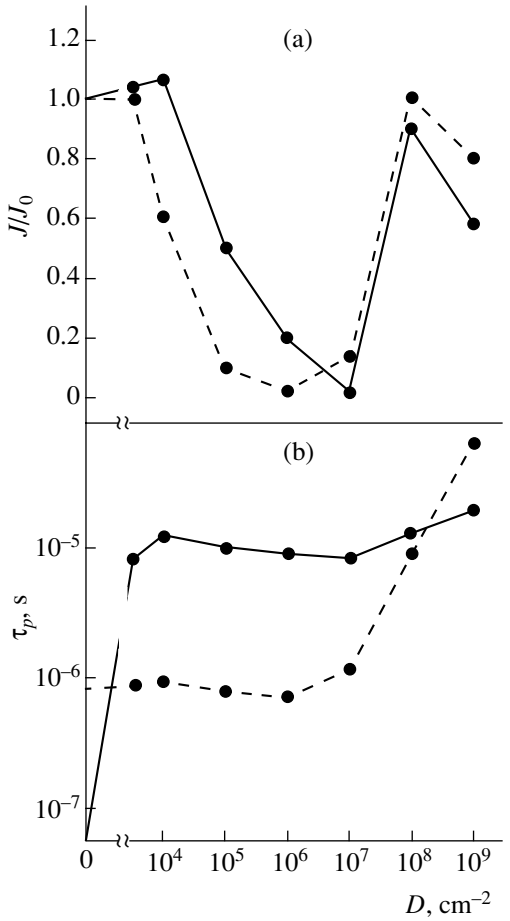

Fig. 1. Plots of (a) the ratio of the collector currents of irradiated (J_r) and unirradiated (J_0) CdTe-based *p–n–p* structures and (b) the minority carrier lifetime τ_p in the base versus the dose D of γ quanta for the samples with resistivities $\rho = 10^4$ Ω cm (solid curve) and 10^5 Ω cm (dashed curve).

assumption concerning the participation of defects in determining the conductivity type in the formation of deep recombination levels.

It should be noted that an increase in the resistivity of the *p*-type region on the irradiated side of the *p–n–p* structure may lead to conversion of the conductivity type from *p* to *n*, as reported for Si-based solar cells [4], resulting in expansion of the base region. Therefore, a decrease in J_r observed in the region of large doses despite the increase in τ_p with monotonic increase of the dose D can be related to the increase in base thickness.

The decrease of τ_p with an increase of D in the region of small doses is probably related to the generation of radiation defects, which serve as effective recombination centers. There are several reasons for the subsequent growth in τ_p with increasing density of defects: a growth of the degree of compensation in a homogeneous semiconductor [6, 8], an increase in the degree of inhomogeneity [9–11], a decrease in the concentration of recombination centers related to the recombination-stimulated transformation [12, 13], and the reactions of defects [14]. The structure under consideration is known to be saturated with various defects and strongly inhomogeneous. The irradiation with γ quanta leads to an increase both in the density of defects and in the degree of inhomogeneity. From this standpoint, it is difficult to give preference to any of the aforementioned mechanisms leading to the increase in τ_p. However, investigation of the dose dependence of the resistivity ρ shows that $\rho(D)$ is also a nonmonotonic function. Therefore, it can be suggested that the increase in the minority carrier lifetime is related to a growth in the degree of compensation of the material.

In order to check for the possible base thickness variation, we have studied the effect of γ radiation on the capacitance–voltage characteristics $C(V)$ of MOS structures based on large-block *p*-CdTe films grown using the technology described in [15]. The results of these measurements showed that the $C(V)$ curves of the samples irradiated with γ quanta to a dose of $D = 1.6 \times 10^{16}$ and 1.6×10^{17} cm^{-2} exhibit descending regions (negative slope) for a negative bias voltage applied to the upper metal electrode. By plotting the $C(V)$ characteristics in these regions as C^{-2} versus V, we obtained straight lines and determined the concentrations of ionized donor centers in *n*-CdTe as $N_d^+ = 3.8 \times 10^{13}$ cm^{-3}. Extrapolated to the voltage axis, these plots determined the contact potential difference $V_k = 0.34$ V between *n*-CdTe and the ITO electrode. The base thickness estimated from these experimental data for the samples irradiated to $D = 1.6 \times 10^{16}$ and 1.6×10^{17} cm^{-2} was 1.3 and 2.9 μm, respectively. These results confirm the hypothesis concerning expansion of the base region.

It should be noted that the $C(V)$ characteristics constructed by the results of mathematical modeling for the absorbed radiation doses $D = 1.6 \times 10^{16}$ and 1.6×10^{17} cm^{-2} are shifted to the right from the experimental curves, while the theoretical plot for $D = 8 \times 10^{17}$ cm^{-2} is on the left from the corresponding experimental $C(V)$ curve. These results indicate that the surface states of a donor type predominate at the ITO–*p*-CdTe interface in the former case, while the states of an acceptor type are dominating in the latter case [16]. This result confirms the assumption about the role of the growing degree of compensation of the material, accompanied by recharge of the surface states and a by a change in the potential barrier height at the grain boundaries, as a factor responsible for an increase in the minority carrier lifetime in irradiated samples.

As is known, γ radiation generates structural defects of the Frenkel type capable of forming local levels. The cation vacancies (V_{Cd}) and interstitial anions (Te_i) can form the acceptor levels, while the anion vacancies (V_{Te}) and interstitial cations (Cd_i) form the donor levels [17]. Since the base of the *p–n–p* structure under consideration is of the *n*-type, we can suggest that radiation

defects responsible for the increase in τ_p, ρ, and J_r are deep donors and can be represented by V_{Te}.

It should be emphasized that a nonmonotonic dependence of the collector current on the absorbed radiation dose takes place only if the minority carrier diffusion length L_p in the base region is shorter than the base thickness W in the initial unirradiated sample and $L_p/W \sim 1$ upon irradiation.

Thus, our investigation of the dose dependence of the collector current J_r in CdTe-based *p–n–p* structures irradiated with γ quanta showed that J_r exhibits a nonmonotonic variation with increasing dose D. It is established that this behavior is caused by expansion of the base region and by a nonmonotonic dose dependence of the minority carrier lifetime, which is accompanied by recharge of the surface states and a change in the potential barrier height at the grain boundaries.

REFERENCES

1. P. Baruch, J. Phys. Chem. Solids **8**, 153 (1959).
2. M. Yamaguchi, S. J. Taylor, M.-Ju. Yang, *et al.*, Jpn. J. Appl. Phys. **35**, 3918 (1996).
3. T. Yamaguchi, S. J. Taylor, S. Watanade, *et al.*, Appl. Phys. Lett. **72**, 1226 (1998).
4. M. Imaizumi, S. J. Taylor, M. Yamaguchi, *et al.*, J. Appl. Phys. **85**, 1916 (1999).
5. M. J. Keevers and M. A. Green, J. Appl. Phys. **75**, 4022 (1994).
6. S. Zh. Karazhanov, J. Appl. Phys. **89**, 4030 (2001).
7. Sh. A. Mirsagatov, A. I. Sultanov, and S. A. Muzaffarova, Geliotekhnika, No. 2, 5 (1986).
8. A. A. Drugova and V. A. Kholodnov, Pis'ma Zh. Tekh. Fiz. **18** (1), 23 (1992) [Sov. Tech. Phys. Lett. **18**, 8 (1992)].
9. A. Rose, *Concepts in Photoconductivity and Allied Problems* (Interscience, New York, 1963; Mir, Moscow, 1966).
10. M. K. Sheĭnkman and A. Ya. Shik, Fiz. Tekh. Poluprovodn. (Leningrad) **10** (2), 209 (1976) [Sov. Phys. Semicond. **10**, 128 (1976)].
11. M. Karimov and A. Karakhodzhaev, Izv. Vyssh. Uchebn. Zaved., Fiz., No. 7, 3 (2000).
12. P. M. Karageorgy-Alkalaev and A. Yu. Leiderman, Phys. Status Solidi B **100**, 221 (1987).
13. S. Zh. Karazhanov, Pis'ma Zh. Tekh. Fiz. **24** (10), 65 (1998) [Tech. Phys. Lett. **24**, 398 (1998)].
14. M. S. Yunusov, S. M. Abdurakhmanova, M. A. Zaĭkovskaya, *et al.*, *Subthreshold Radiation Effects in Semiconductors* (Fan, Tashkent, 1989).
15. Sh. A. Mirsagatov and S. A. Muzaffarova, Geliotekhnika, No. 2, 18 (1983).
16. S. Sze, *Physics of Semiconductor Devices* (Wiley, New York, 1981; Mir, Moscow, 1984), Vol. 1.
17. Chadi, Mater. Sci. Forum, Part 3, 1321 (1997).

Translated by P. Pozdeev

Technical Physics Letters, Vol. 29, No. 11, 2003, pp. 920–922. Translated from Pis'ma v Zhurnal Tekhnicheskoĭ Fiziki, Vol. 29, No. 21, 2003, pp. 88–94.

The Influence of Moving Domain Walls on the Appearance of the Second Harmonic in the Magnetoimpedance Spectrum of a Cobalt-Based Amorphous Microwire

N. A. Buznikov*, A. S. Antonov, and A. L. Rakhmanov

Institute of Theoretical and Applied Electrodynamics, Russian Academy of Sciences, Moscow, Russia

** e-mail: n_buznikov@mail.ru*

Received May 13, 2003

Abstract—We have studied the influence of moving domain walls (DWs) on the magnetoimpedance of a cobalt-based amorphous microwire. A model describing the DW motion in the electric field of an alternating current in the absence of a skin effect is proposed. When the current amplitude exceeds a certain threshold value, the DW motion leads to the appearance of a second harmonic component in the frequency spectrum of the sample response voltage. The second harmonic amplitude has been studied as a function of the external longitudinal magnetic field, the current frequency, and the angle of deviation of the microwire anisotropy axis from the circular direction. The sensitivity of the second harmonic to the external magnetic field can be significantly higher than that of the first harmonic. *© 2003 MAIK "Nauka/Interperiodica".*

The interest in cobalt-based magnetically soft amorphous microwires is related to the unusual physical properties of these materials and their promising applications. In particular, these wires exhibit the so-called giant magnetoimpedance effect, whereby the impedance of a sample strongly changes in an applied magnetic field (see, e.g., [1–4] and references therein). This effect has attracted much attention in view of the possibility of creating highly effective magnetic sensors capable of detecting weak magnetic fields [1, 5, 6]. The giant magnetoimpedance is observed at a sufficiently small amplitude of the alternating current passing in the sample, whereby the response signal is proportional to the impedance of a microwire sample.

In recent years, the spectrum of harmonics of the response signal was measured for higher amplitudes of the current passing in microwires [7–13], in which case a relation between the sample magnetization and the current amplitude is nonlinear. Under these conditions, the sensitivity of the second-harmonic signal to the external magnetic field turns out to be much higher as compared to the sensitivity of the first harmonic. The behavior of the spectrum of voltage harmonics can be qualitatively described within the framework of a model assuming homogeneous rotation of the sample magnetization vector in the field of the alternating current [8–10, 13]. However, this approximation does not take into account a domain structure of the amorphous microwire that may significantly influence the frequency spectrum of the response signal. Below, we consider another possible mechanism accounting for a nonlinear response, based on the motion of domain boundaries along an amorphous microwire.

The distribution of easy anisotropy axes in microwires is determined by the stresses arising in the material in the course of synthesis. The magnetic properties of cobalt-based amorphous microwires are described within the framework of a model assuming the presence of two regions in the samples: a central region with the anisotropy axis directed along the wire axis and a near-surface region possessing a circular or helicoidal anisotropy [1, 14–18]. In the case of weak longitudinal magnetic fields, the near-surface region can acquire a metastable domain structure comprising a sequence of domains with alternating signs of the circular component of the magnetization vector [14–16, 19–23]. Following [7], we will ignore the contribution to the response signal from the central region with longitudinal anisotropy and assume that the anisotropy axis in the whole sample makes a constant angle ψ with the circular direction.

Consider an amorphous microwire sample with a length l and a diameter d exposed to a constant external magnetic field H_e. Assume that the microwire is divided into domains of equal length a, in which the circular magnetization components have opposite signs. The angles θ_j, describing deviation of the magnetization vectors in the jth domain (j = 1, 2) from the circular direction, are determined from the condition of minimum free energy. This energy can be represented by a sum of the energy of anisotropy and the Zeeman energy in the longitudinal magnetic field [2, 24]:

$$H_a \sin\{2(\theta_j - \psi)\} = 2H_e \cos\theta_j, \qquad (1)$$

where H_a is the anisotropy field.

1063-7850/03/2911-0920$24.00

The influence of the moving domain wall (DW) on the impedance of an amorphous microwire will be considered using the following model. Let us assume that the domain boundaries are immobile for small amplitudes of alternating current. When the current $I(t) = I_0\sin(\omega t)$ exceeds a certain threshold value I_{th}, the domain boundaries start moving along the sample. The motion of a domain boundary with a not too large velocity under the action of the magnetic field of the alternating current can be described by the following equation (see, e.g., [25, 26]):

$$\beta v = M\{\cos\theta_1 - \cos\theta_2\}H_\varphi(t). \quad (2)$$

Here, β is the DW mobility proportional to the losses for vortex currents [25] arising when the DW moves along the sample; v is the DW velocity; M is the saturation magnetization, and $H_\varphi(t)$ is the magnetic field of the current passing in the sample. In the case under consideration, the DW mobility is [22]

$$\beta = 35\sigma d M^2 \sin^2\{(\theta_1 - \theta_2)/2\}/c^2, \quad (3)$$

where σ is the wire conductivity.

Let us restrict the consideration to low frequencies for which the skin effect can be ignored. In this case, H_φ varies linearly in the wire cross section. For an analytical description of the DW motion, we replace H_φ in Eq. (2) by the value averaged over the wire cross section [27]. Then the DW displacement can be expressed as

$$\Delta z(t) = \frac{8cI_0}{105\sigma d^2 M\omega}\frac{\cos\theta_1 - \cos\theta_2}{\sin^2\{(\theta_1 - \theta_2)/2\}} \times [\sqrt{1 - (I_{th}/I_0)^2} - \cos(\omega t)], \quad |I(t)| > I_{th}. \quad (4)$$

A change in the voltage V between the sample ends related to the DW motion is described by the expression

$$V = (4I_0 l^2/cda)[\{a/2 - z(t)\}\mathrm{Re}\{\zeta_1\exp(-i\omega t)\} + \{a/2 + z(t)\}\mathrm{Re}\{\zeta_2\exp(-i\omega t)\}], \quad (5)$$

where $z(t)$ is the DW coordinate (for small current amplitudes, $z(t) \equiv 0$) and ζ_j are the contributions to the surface impedance from the domains with opposite directions of the circular magnetization components.

At low frequencies, the quantities ζ_j are given by the formulas [2]

$$\zeta_j = (c/\pi\sigma d)\{1 - i(\pi\sigma d^2\omega/8c^2)(1 + \mu_j\sin^2\theta_j)\}, \quad (6)$$

$$\mu_j = \omega_m^2/[\omega_m\omega_\alpha[(H_e/H_a)\sin\theta_j + \cos\{2(\theta_j - \psi)\}] - \omega^2 - i\alpha\omega_m\omega], \quad (7)$$

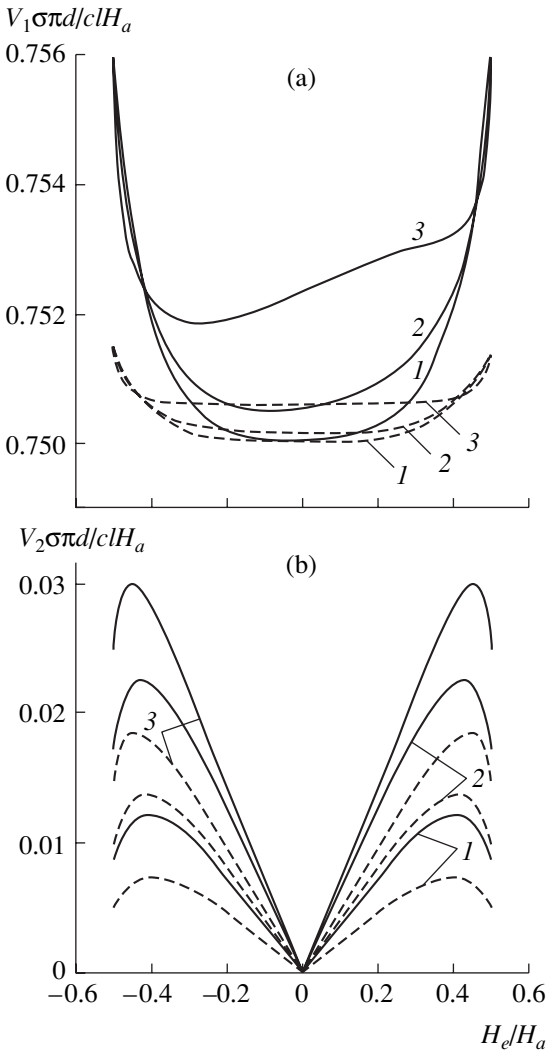

Fig. 1. Plots of the amplitude of (a) the first harmonic V_1 and (b) the second harmonic V_2 versus the longitudinal external magnetic field H_e for $\omega/2\pi = 5 \times 10^4$ s^{-1} (dashed curves) and 10^5 s^{-1} (solid curves) and $\psi = 0.05\pi$ (*1*), 0.1π (*2*), and 0.15π (*3*). The calculations were performed using Eqs. (1), (4)–(7) with the following parameters: $M = 600$ G; $H_a = 2$ Oe; $l = 1$ cm; $d = 60$ μm; $a = 5$ μm; $\sigma = 10^{16}$ s^{-1}; $\alpha = 0.1$; $4I_0/cdH_a = 0.75$; $4I_{th}/cdH_a = 0.05$.

where $\omega_m = 4\pi\gamma M$, $\omega_a = \gamma H_a$, γ is the gyromagnetic ratio, and α is the damping constant in the Landau–Lifshits–Gilbert equation [26].

For small amplitudes of alternating current ($I_0 < I_{th}$), the DWs are immobile, the voltage between the sample ends appears as a result of precession of the magnetic moment about equilibrium position in the domains, and the frequency spectrum of the response voltage contains only the fundamental harmonic ω. When $I_0 > I_{th}$, a part of the wire exhibits remagnetization related to the DW motion and the frequency spectrum acquires harmonics with frequencies that are multiples of ω.

Figure 1 shows the plots of the first and second harmonics as functions of the longitudinal magnetic field H_e calculated using Eqs. (1), (4)–(7) for two frequencies of alternating current and various values of the angle of deviation of the anisotropy axis from the circular direction. As can be seen from Fig. 1a, the first harmonic amplitude V_1 weakly depends on the longitudinal field in the region of small H_e and the curves of $V_1(H_e)$ are non-symmetric with respect to a change of the field sign. The second harmonic amplitude V_2 has a much lower amplitude, but it exhibits a much stronger dependence on H_e and the $V_2(H_e)$ curves are symmetric with respect to a change of the field sign. Figure 1b shows that the second harmonic amplitude increases with the angle of deviation of the anisotropy axis from the circular direction. At small frequencies, the second harmonic amplitude increases with ω. As the frequency grows further, the V_2 value ceases to change because the displacements of the domain boundaries during each half-period are very small and such DW motions weakly influence the response signal.

To summarize, we have considered one of the possible mechanisms accounting for the appearance of the second harmonic in the frequency spectrum of the response voltage measured on an amorphous microwire, which is related to the motion of domain walls. The second harmonic, appearing when the current amplitude exceeds a certain threshold, is related to remagnetization of a part of the sample. In the region of low frequencies, where the skin effect is absent, the sensitivity of the second harmonic to the external magnetic field can be significantly higher than that of the first harmonic. For the typical values of parameters of a microwire used for the calculations, the sensitivity of the second harmonic to the external magnetic field is on the order of 5 mV/Oe. Finally, it should be noted that the motion of domain boundaries is possible when the longitudinal magnetic field is below a certain threshold level. In high longitudinal fields, a nonlinear response is related to homogeneous remagnetization of the sample along the entire length [7–10, 13].

Acknowledgments. This study was supported by the Russian Foundation for Basic Research (project no. 02-02-16707) and the Presidential Program for Support of the Leading Scientific Schools (project NSh-1694.2003.2). One of the authors (N.A.B.) gratefully acknowledges the support from the Foundation for Promotion of Science in Russia.

REFERENCES

1. M. Vazquez and A. Hernando, J. Phys. D: Appl. Phys. **29**, 939 (1996).
2. D. P. Makhnovskiy, L. V. Panina, and D. J. Mapps, Phys. Rev. B **63**, 144424 (2001).
3. M. Vazquez, J. Magn. Magn. Mater. **226–230**, 693 (2001).
4. M. Knobel and K. R. Pirota, J. Magn. Magn. Mater. **242–245**, 33 (2002).
5. K. Mohri, T. Uchiyama, and L. V. Panina, Sens. Actuators A **59** (1), 1 (1997).
6. M. Vazquez, M. Knobel, M. L. Sanchez, *et al.*, Sens. Actuators A **59** (1), 20 (1997).
7. A. S. Antonov, N. A. Buznikov, I. T. Iakubov, *et al.*, J. Phys. D: Appl. Phys. **34**, 752 (2001).
8. C. Gomez-Polo, M. Vazquez, and M. Knobel, J. Magn. Magn. Mater. **226–230**, 712 (2001).
9. C. Gomez-Polo, M. Vazquez, and M. Knobel, Appl. Phys. Lett. **78**, 246 (2001).
10. C. Gomez-Polo, M. Knobel, K. R. Pirota, and M. Vazquez, Physica B **299** (3–4), 322 (2001).
11. G. V. Kurlyandskaya, H. Yakabchuk, E. Kisker, *et al.*, J. Appl. Phys. **90**, 6280 (2001).
12. G. V. Kurlyandskaya, E. Kisker, H. Yakabchuk, and N. G. Bebenin, J. Magn. Magn. Mater. **240** (1–3), 206 (2002).
13. C. Gomez-Polo, K. R. Pirota, and M. Knobel, J. Magn. Magn. Mater. **242–245** (1), 294 (2002).
14. K. Mohri, F. B. Humphrey, K. Kawashima, *et al.*, IEEE Trans. Magn. **26**, 1789 (1990).
15. K. Mohri, T. Kohzawa, K. Kawashima, *et al.*, IEEE Trans. Magn. **28**, 3150 (1992).
16. L. V. Panina, K. Mohri, T. Uchiyama, *et al.*, IEEE Trans. Magn. **31**, 1249 (1995).
17. H. Chiriac, T. A. Ovari, and Gh. Pop, Phys. Rev. B **52**, 10104 (1995).
18. M. Vazquez and A. P. Zhukov, J. Magn. Magn. Mater. **160**, 223 (1996).
19. M. Takajo, J. Yamasaki, and F. B. Humphrey, IEEE Trans. Magn. **29**, 3484 (1993).
20. L. V. Panina, K. Mohri, K. Bushida, and M. Noda, J. Appl. Phys. **76**, 6198 (1994).
21. N. Usov, A. Antonov, A. Dykhne, and A. Lagarkov, J. Magn. Magn. Mater. **174** (1–2), 127 (1997).
22. A. S. Antonov, N. A. Buznikov, A. B. Granovsky, *et al.*, J. Magn. Magn. Mater. **249** (1–2), 95 (2002).
23. E. E. Shalygina, V. V. Molokanov, and M. A. Komarova, Zh. Éksp. Teor. Fiz. **122**, 593 (2002) [JETP **95**, 511 (2002)].
24. A. S. Antonov, I. T. Iakubov, and A. N. Lagarkov, J. Magn. Magn. Mater. **187**, 252 (1998).
25. S. Chikasumi, *The Physics of Ferromagnetism. Magnetic Characteristics and Engineering Applications* (Syokabo, Tokyo, 1984; Mir, Moscow, 1987).
26. A. G. Gurevich and G. A. Melkov, *Magnetic Oscillations and Waves* (Nauka, Moscow, 1994).
27. N. A. Buznikov, A. S. Antonov, and A. L. Rakhmanov, Zh. Tekh. Fiz. **70** (2), 43 (2000) [Tech. Phys. **45**, 184 (2000)].

Translated by P. Pozdeev

Technical Physics Letters, Vol. 29, No. 11, 2003, pp. 923–926. Translated from Pis'ma v Zhurnal Tekhnicheskoĭ Fiziki, Vol. 29, No. 22, 2003, pp. 1–9.

Behavior of Dynamical Systems in the Regime of Transient Chaos

G. B. Astaf'ev*, A. A. Koronovskiĭ, and A. E. Khramov

State Scientific Center "College," Saratov State University, Saratov, Russia

** e-mail: astafyev@cas.ssu.runnet.ru*

Received May 6, 2003

Abstract—The transient chaos regime in a two-dimensional system with discrete time (Eno map) is considered. It is demonstrated that a time series corresponding to this regime differs from a chaotic series constructed for close values of the control parameters by the presence of "nonregular" regions, the number of which increases with the critical parameter. A possible mechanism of this effect is discussed. © *2003 MAIK "Nauka/Interperiodica".*

The phenomenon of transient chaos accompanying the crisis of a strange attractor [1] is rather frequently encountered in dynamical systems of various natures. In particular, such phenomena were observed in hydrodynamic experiments [2], radio circuits [3], chemical reactions [4], optical bistable media [5], distributed systems of the type of an electron flow interacting with a backward wave [6], and standard models of nonlinear dynamics such as logistic maps [7], the Eno map [8], and the Rössler system [9].

The transient chaos is essentially a regime, whereby the distance between a strange attractor and the boundary of its basin of attraction in the phase space decreases until they touch each other at a critical value of the control parameter ($p = p_c$). At this point, the chaotic attractor exhibits a crisis (and ceases to exist at $p > p_c$), converting into an unstable chaotic manifold called a chaotic saddle. Accordingly, the behavior of the given system changes, the initial chaotic dynamics being replaced by the transient chaos. In the initial stage of this regime, the system behavior is virtually indistinguishable from chaotic, but then the system rapidly passes to another stable state (attractor) that can be stationary, periodic, or chaotic as well.

A chaotic saddle replacing the chaotic attractor in the phase space is of considerable basic interest. Some properties of the chaotic saddle can be derived from an analysis of the initial stage reflecting the transient chaos regime in a large number of time series [9, 10]. An alternative approach consists in constructing a long artificial time series by matching the initial and end parts of time series, linking them into one [11]. Finally, trajectories existing for a long time in the vicinity of a chaotic saddle can be constructed using the so-called proper interior maximum (PIM) triple [12] and PIM simplex [13] methods, or the method of step perturbations [14]. The resulting long time series offers a good approximation of the chaotic trajectory belonging to the given unstable chaotic manifold.

The aim of this study was to compare the chaotic trajectories obtained for two close values of the control parameter p, one corresponding to the chaotic attractor ($p < p_c$) and the other, to the chaotic saddle ($p > p_c$).

The study was performed on an Eno map [15] of the type

$$\begin{aligned} x_{n+1} &= \lambda x_n(1 - x_n) + by_n, \\ y_{n+1} &= x_n, \end{aligned} \tag{1}$$

which is a standard model in nonlinear dynamics. For the control parameters $\lambda \approx 4.21934$ and $b = -0.61$, a chaotic attractor based on the cycle of period 3 exhibits a boundary crisis via a series of period doubling bifurcations, loses stability, and transforms into a chaotic saddle. Simultaneously, a stable rest point, representing an attractor, exists in the phase space of this system.

A time series corresponding to the chaotic attractor was constructed for $\lambda = 4.219$ (Fig. 1a). An analogous time series corresponding to the chaotic saddle ($\lambda = 4.22$) was constructed by the method of step perturbations [14]. This procedure reduces to determining, for an arbitrary point $\mathbf{x}$ in the vicinity of a chaotic saddle, a time $T(\mathbf{x})$ for which a phase trajectory starting from this point reaches the attractor [16]. If the time $T(\mathbf{x})$ proves to be greater than a certain threshold value T^*, the point $\mathbf{x}$ is considered as belonging to an unstable chaotic manifold. In order to construct a long time series corresponding to the regime of transient chaos, the initial dynamical system is iterated as follows:

$$\mathbf{x}_{n+1} = \begin{cases} \mathbf{F}(\mathbf{x}_n) & \text{for} \quad T(\mathbf{x}_n) > T^*(\text{step}), \\ \mathbf{F}(\mathbf{x}_n + \mathbf{r}_n) & \text{for} \quad T(\mathbf{x}_n) \le T^*(\mathbf{r}_n \text{ is perturbation}), \end{cases} \tag{2}$$

1063-7850/03/2911-0923$24.00 © 2003 MAIK "Nauka/Interperiodica"

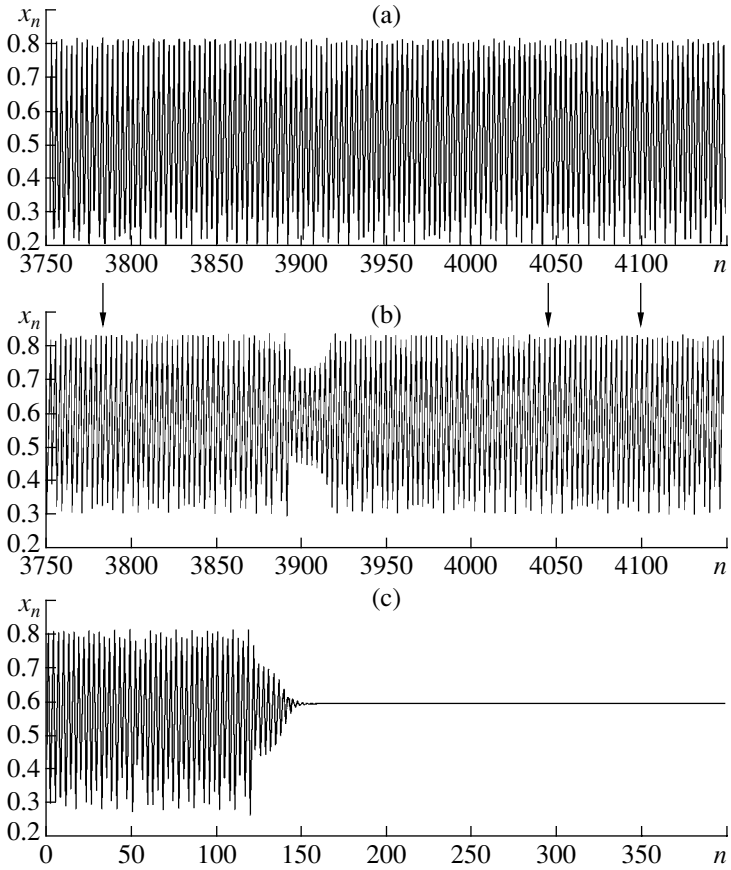

Fig. 1. Fragments of time series for the Eno maps (1) with $b = -0.61$: (a) exhibiting a chaotic attractor ($\lambda = 4.219$); (b) featuring a chaotic saddle ($\lambda = 4.22$); (c) escaping from the transient chaos regime ($\lambda = 4.22$). The time series (b) were constructed by the method of step perturbations (arrows indicate the moments of discrete time n corresponding to the introduction of small perturbations $\mathbf{r}$).

where $\mathbf{F}(\mathbf{x})$ is the operator of evolution of the initial dynamical system, $\mathbf{r}_n$ is a perturbation vector such that $T(\mathbf{x}_n + \mathbf{r}_n) > T^*$, and $|\mathbf{r}_n| < \delta = 10^{-7}$. Here, vector $\mathbf{r}_n$ is a random quantity but, in order to accelerate construction of the time series, the probability density distribution $p(\mathbf{r})$ has to obey certain requirements (see [14]).

Thus, until the time required for an imaging point to attain the attractor exceeds a certain preset (sufficiently large) threshold T^*, the point is considered to occur near the chaotic saddle. The initial dynamical system, representing the Eno map (1), was iterated according to this procedure. As soon as the time of attaining the attractor becomes equal to the threshold value, the point on the trajectory is variously perturbed and the possible perturbation $\mathbf{r}_n$ is selected for which the time $T(\mathbf{x}_n + \mathbf{r}_n)$ required for the perturbed imaging point to attain the attractor would exceed the threshold T^*. Since the perturbation vector $\mathbf{r}$ is small ($|\mathbf{r}_n| < \delta = 10^{-7}$), the sequence of $\mathbf{x}_n$ offers a good approximation of the chaotic saddle.

According to the results of our investigations, a time series corresponding to the regime of transient chaos differs from a chaotic series only by the presence of "outbursts" representing nonregular regions in which the system dynamics differs from typical. The rest of the time, the chaotic time series is virtually identical to that of the transient chaos (Fig. 1). It should be noted that the appearance of nonregular regions in the time series of transient chaos is by no means related to the small perturbations $\mathbf{r}$ introduced into the system dynamics. In Fig. 1b, the moments of discrete time n corresponding to the introduction of perturbations are indicated by the arrows. As can be seen, the system shows typical behavior for a rather long time after the moment of perturbation and then features a nontypical region in the time series. Moreover, by no means each perturbation is followed by such a response.

As the critical parameter $\lambda - \lambda_c$ increases, the number of nonregular regions grows, while regular regions become shorter. This system behavior in the transient chaos regime is much like intermittency [17, 18], whereby a time series exhibits alternating laminar and turbulent parts, or crisis-induced intermittency [19], in which case several regions of a chaotic attractor merge upon a crisis and the imaging point, having spent some time in one region of the attractor, jumps to another region of this attractor. The appearance of such nonreg-

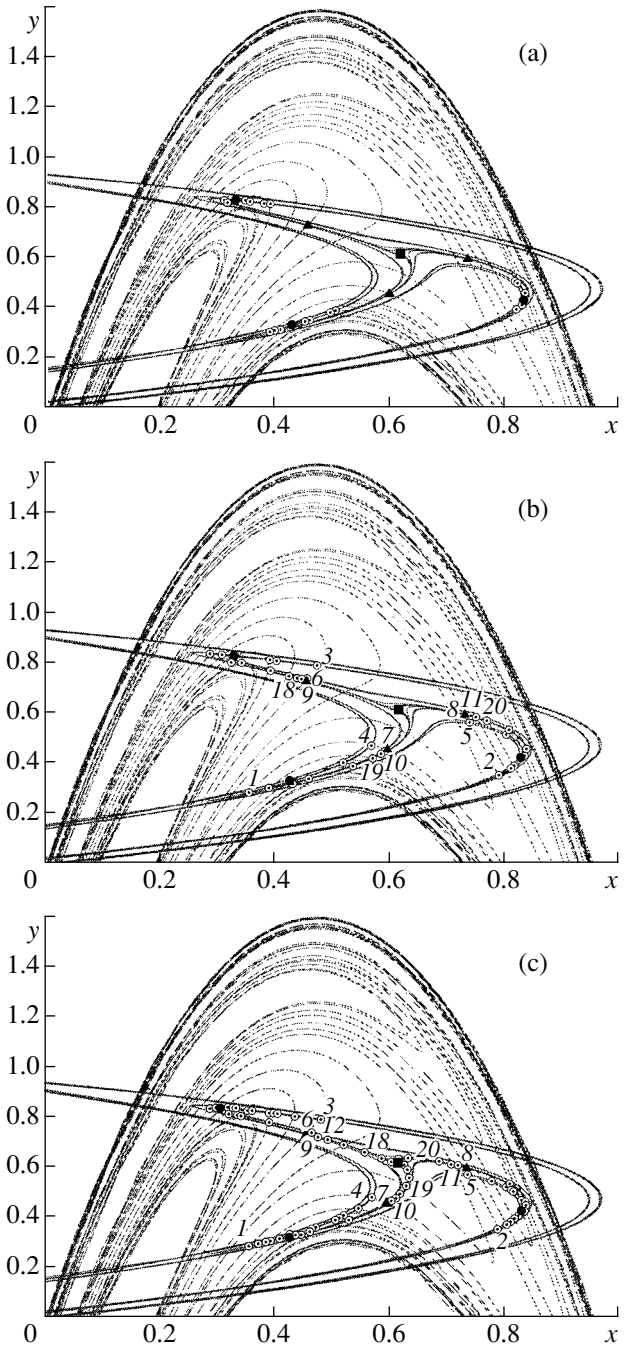

Fig. 2. Schematic diagrams showing the positions of a stable point (■), unstable cycles of period 3 (▲ and ●), and the unstable (solid curves) and stable (dashed curves) manifolds of these cycles for the Eno map (1) with $\lambda = 4.22$ and $b = -0.61$: (a) points (○) in a typical region of the time series corresponding to the transient chaos regime; (b) points in the untypical region (figures indicate the numbers of iteration steps, beginning with the first, in which the imaging point falls in the region of intersection of the stable and unstable manifolds of the period-3 cycle, which accounts for the appearance of the untypical region); (c) points in the region where the system escapes from the transient chaos regime (figures indicate the numbers of iteration steps, beginning with the first, in which the imaging point falls in the region of intersection of the stable and unstable manifolds of the period-3 cycle, which accounts for the escape).

ular regions in the time series corresponding to the transient chaos regime is caused mostly by the same factors as the escape of the imaging point from a chaotic saddle region [20].

Figure 2 shows the structure of manifolds for two unstable cycles of period 3, which coexist in the phase space with an immobile stable point in a system with the control parameters $\lambda = 4.22$ and $b = -0.61$. The manifolds were mapped using the method described in [21–23]. As can be seen, stable and unstable manifolds exhibit a rather complicated structure, intersecting each other an infinite number of times. Figure 2a shows a trajectory of the imaging point for the system exhibiting typical behavior. Here, the points of a chaotic saddle are arranged along unstable manifolds of the unstable cycles of period 3 and are confined within a certain region.

A nontypical region in the time series begins at the moment when the imaging point, moving in the vicinity of the unstable manifold of the unstable cycle of period 3, falls in the vicinity of the region of intersection of the unstable and stable manifolds of this cycle (point *1* in Fig. 2b). Then, the imaging point begins to visit regions in the (x, y) phase plane in which the stable and unstable manifolds intersect, thus approaching the unstable cycle of period 3. After entering the vicinity of this cycle, the imaging point occurs for some time in this region and then returns (along the unstable manifold of the unstable cycle) to the chaotic saddle region (Fig. 2b). The return of the imaging point to this region corresponds to completion of a nontypical region in the time series.

An analogous mechanism accounts for escape of the system from the transient chaos regime (Fig. 2c). The only difference consists in that the imaging point enters the vicinity of the unstable cycle of period 3 from the other side of a relatively stable manifold. Then, moving along an unstable manifold of the unstable cycle for a relatively short period of discrete time, the imaging point reaches an attractor (in this example, an immobile point). In this sense, the stable manifold of the unstable cycle is essentially a boundary separating regions of a fast transient process and transient chaos on the phase plane. This is similar to the case of multistability, where a stable manifold of the unstable cycle is a boundary of the basins of attraction of the attractors [24, 25].

To summarize, we have demonstrated that time series of a dynamical system with discrete time occurring in the transient chaos regime contain regions of nontypical behavior reflecting the approach of the imaging point to an unstable cycle along a stable manifold, followed by a return of the imaging point to the chaotic saddle region.

Acknowledgments. This study was supported by the Russian Foundation for Basic Research (project no. 02-02-16351) and by the Scientific-Education Center “Nonlinear Dynamics and Biophysics” at the Saratov State University (Grant REC-006 from the US

Civilian Research and Development Foundation for the Independent States of the Former Soviet Union).

REFERENCES

1. C. Grebogi, E. Ott, and J. A. Yorke, Phys. Rev. Lett. **48**, 1507 (1982).
2. G. Ahlers and R. W. Walden, Phys. Rev. Lett. **44**, 445 (1980).
3. L. Zhu, A. Raghu, and Y.-C. Lai, Phys. Rev. Lett. **86**, 4017 (2001).
4. M. Dhamala and Y.-C. Lai, Phys. Rev. E **59**, 1646 (1999).
5. H. W. Yin and J.-H. Dai, Phys. Rev. E **54**, 371 (1996).
6. A. A. Koronovskiĭ, I. S. Rempen, D. I. Trubetskov, and A. E. Khramov, Izv. Ross. Akad. Nauk, Ser. Fiz. **66**, 1754 (2002).
7. M. Woltering and M. Markus, Phys. Rev. Lett. **84**, 630 (2000).
8. M. Dhamala and Y.-C. Lai, Phys. Rev. E **60**, 6176 (1999).
9. M. Dhamala, Y.-C. Lai, and E. J. Kostelich, Phys. Rev. E **61**, 6485 (2000).
10. M. Dhamala, Y.-C. Lai, and E. J. Kostelich, Phys. Rev. E **64**, 056207 (2001).
11. I. M. Janosi and T. Tel, Phys. Rev. E **49**, 2756 (1994).
12. H. E. Nusse and J. A. Yorke, Physica D **36**, 137 (1989).
13. P. D. S. Moresco, Physica D **126**, 38 (1999).
14. D. Sweet, H. E. Nusse, and J. A. Yorke, Phys. Rev. Lett. **86**, 2261 (2001).
15. M. Hénon, Commun. Math. Phys. **50**, 69 (1976).
16. A. A. Koronovskiĭ, A. V. Starodubov, and A. E. Khramov, Izv. Vyssh. Uchebn. Zaved. Prikl. Nelineĭnaya Din. **10** (5), 25 (2002).
17. P. Manneville and Y. Pomeau, Physica D **1**, 167 (1980).
18. H. G. Shuster, *Deterministic Chaos* (Physik-Verlag, Weinheim, 1984; Mir, Moscow, 1998).
19. C. Grebogi, E. Ott, F. Romeiras, and J. A. Yorke, Phys. Rev. A **36**, 5365 (1987).
20. C. Grebogi, E. Ott, and J. A. Yorke, Phys. Rev. Lett. **57**, 1284 (1986).
21. T. S. Parker and L. O. Chua, *Practical Numerical Algorithms for Chaotic Systems* (Springer-Verlag, Berlin, 1989).
22. Z. P. You, E. J. Kostelich, and J. A. Yorke, Int. J. Bifurcation Chaos Appl. Sci. Eng. **1**, 605 (1991).
23. E. J. Kostelich, J. A. Yorke, and Z. Yuo, Physica D **93**, 210 (1996).
24. C. Grebogi, E. Ott, and J. A. Yorke, Phys. Rev. Lett. **56**, 1011 (1986).
25. H. E. Nusse, E. Ott, and J. A. Yorke, Phys. Rev. Lett. **75**, 2482 (1995).

Translated by P. Pozdeev

Technical Physics Letters, Vol. 29, No. 11, 2003, pp. 927–929. Translated from Pis'ma v Zhurnal Tekhnicheskoĭ Fiziki, Vol. 29, No. 22, 2003, pp. 10–15.

The Effect of Electron Density on the Kinetics of Fullerene Formation in Carbon Plasma

K. L. Stepanov[a,*], Yu. A. Stankevich[a], L. K. Stanchits[a], G. N. Churilov[b,], A. S. Fedorov[b], and P. V. Novikov[b]**

[a] *Lykov Institute of Heat and Mass Transfer, National Academy of Sciences of Belarus, Minsk, Belarus*

[b] *Kirensky Institute of Physics, Siberian Division, Russian Academy of Sciences, Krasnoyarsk, Russia*

*e-mail: * kls@hmti.ac.by; ** churilov@iph.krasn.ru*

Received May 5, 2003

Abstract—The influence of the carbon cluster charge on their coagulation kinetics has been studied. The equations of kinetics have been solved and it is established that allowance for the cluster charging leads to an increase in the rate of fullerene formation under otherwise equal conditions. In connection with this, the role of minor impurities with a low ionization potential in carbon-containing plasma is discussed. © *2003 MAIK "Nauka/Interperiodica".*

There are many models of fullerene formation [1] which consider various precursor clusters and different transformation pathways. However, most of these models do not take into account that all effective methods of fullerene synthesis employ plasma technologies [2–4]. This implies that carbon clusters bear an electric charge that certainly influences the process of fullerene formation. The effect of cluster charging has been demonstrated experimentally [5] and described theoretically [6]. The signs and values of charges on carbon clusters depend on the plasma parameters, in particular, on the electron density and temperature. In this context, we have studied the effect of electron density on the efficiency of fullerene formation in carbon plasma.

The analysis is performed within the framework of a semiempirical kinetic model of the growth of carbon clusters. The main assumptions of this model are as follows. Every collision of two clusters, C_i and C_k, leads with a certain probability W_{ik} to the formation of a cluster C_{i+k}. The reverse process is ignored, since the rate of such fragmentation in the temperature range of cluster growth is small because the binding energy is sufficiently large [7]. The distribution of charges on clusters at a given temperature and electron density is determined by the Saha equations [6]. The electron density depends primarily on the presence of minor additives of readily ionized metals in the plasma. The rate of collisions between clusters is calculated according to the classical theory. The effect of cluster charging on the coagulation rate reduces to correcting the cross sections for the Coulomb interaction [6].

Equations describing the kinetics of cluster formation in a stationary flow are as follows:

$$\frac{dc_i}{dx} = \sum_{k=1}^{i/2} c_k c_{i-k} I_{k,i-k} - c_i \sum_k c_k I_{ik}, \quad \sum_i i c_i = 1. \quad (1)$$

Here $c_i = n_i/N_C(r)$ is the relative density of clusters of the ith type (C_i), x is the dimensionless spatial coordinate, and I_{ik} is the dimensionless coagulation rate. The latter quantity is given by the expression

$$I_{ik} = W_{ik}\sqrt{\frac{i+k}{ik}}\frac{(R_i+R_k)^2}{D_1^2} \times \sum_{q_i} P_i(q_i)\sum_{q_k} P_k(q_k)\left[1 - \frac{q_i q_k}{(R_i+R_k)3kT/2}\right], \quad (2)$$

where R_i is the effective size of clusters of the ith type, D_1 is the effective "diameter" of a monomer, q_i is the possible charge on the ith cluster, and $P_i(q_i)$ is the probability for the cluster to bear this charge. It is assumed that clusters can be either neutral or singly ionized, or can (in view of a large electron affinity) acquire a single or double negative charge.

The probabilities of various charged states of C_i clusters are given by the relations

$$\frac{P_i(q+1)c_e}{P_i(q)} = \frac{AT^{3/2}}{N_C(r)}\frac{Z_k^{q+1}}{Z_k^q}\exp\left(-\frac{E_i^q}{kT}\right), \quad (3)$$

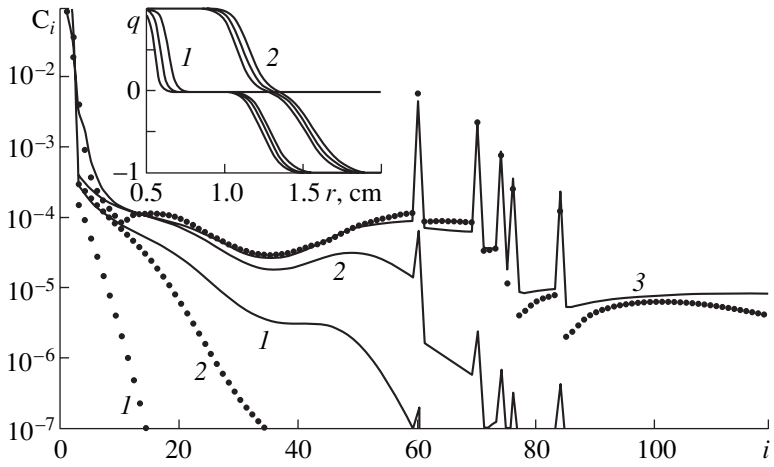

Fig. 1. Evolution of the cluster size distribution with increasing distance from the plasma source (see the text for explanations). The inset shows variation of the average charge profile for small (C_1–C_4, curves *1*) and large (C_{40}, C_{50}, and C_{60}, curves *2*) clusters.

where $c_e = n_e/N_C(r)$, Z_i^q is the electron partition function for clusters with the charge q, and E_i^q is the ionization energy of such clusters. In writing Eq. (3), it is assumed that the ratio of vibrational and rotational partition functions for clusters of the same type possessing various charges is unity. The parameters of energy structure, ionization energies, and electron affinities of clusters necessary for the calculations were calculated using a VASP program package [8].

It should be also noted that, in a quasi-one-dimensional approximation, the dimensionless coordinate x is related to the distance r from the arc source as $dx = N_C(r)v_C(r)\sigma_{11}dr/U(r)$, where v_C is the thermal velocity of carbon atoms, σ_{11} is the gaskinetic cross section for the collision of monomers, and $U(r)$ is the mass flow rate. Assuming the motion of a gas–plasma mixture to be nearly adiabatic ($T \sim \rho^{\gamma-1}$) and representing a change in the carbon concentration and flow velocity as $N_C(r) = N_{C0}(r_0/r)^\delta$ and $U(r) = U_0(r_0/r)^\beta$, respectively (N_{C0} and U_0 being the carbon concentration and jet velocity at the exit from the discharge zone, respectively, and r_0 the electrode radius), we can write the relation between r and x as

$$r = r_0 \times \begin{cases} (1 + \alpha Lx/r_0)^{1/\alpha}, & \alpha \neq 0, \\ \exp(Lx/r_0), & \alpha = 0. \end{cases} \quad (4)$$

Here, $L = U_0/(N_{C0}v_{C0}\sigma_{11})$ is the particle pathlength between two monomer collisions in the mass flow for the initial plasma parameters and $\alpha = \beta + 1 - \delta(\gamma + 1)/2$. For $\beta = \delta = 1$ and $\gamma = 2$, the distribution of gasdynamic characteristics corresponds to that of a flat turbulent jet [7, 9]. In this case, $\alpha = 1/2$ and the quantities N_C, U, and T decrease in inverse proportion to the distance: $(N_C, U, T) = (N_{C0}, U_0, T_0)(r_0/r)$.

The relative densities of electrons (c_e), impurity atoms (c_M), and impurity ions (c_M^+) are described by relations

$$\frac{dc_e}{dx} = \frac{N_C V_R}{v_C \sigma_{11}} c_e \left[c_M \frac{AT^{3/2}}{N_C} \frac{Z_M^+}{Z_M} \exp\left(-\frac{J_M}{kT}\right) - c_M^+ c_e \right], \quad (5)$$

$$\frac{dc_M}{dx} = -\frac{dc_e}{dx} = -\frac{dc_M^+}{dx},$$

where V_R is the impurity recombination rate [10]. It should be noted that the balance for electrons does not take into account cluster charging. Use of the equilibrium approximation is related to the absence of reliable information concerning the rates of ionization and recombination processes in the system studied. Nevertheless, even this (not quite self-consistent) formulation allows the effect of electric charge on the cluster coagulation dynamics to be evaluated.

In numerically solving the equations of kinetics, the dependence of R_i on the number of carbon atoms was empirically set taking into account experimental data on the cluster dimensions. This distribution function is nonmonotonic, reflecting an increase in R_i in the region of existence of chains and both flat and double rings ($10 \le i \le 40$). The probability of coagulation was calculated according to the model [9], whereby $W_{ik} \sim N_{He}a^3$ for small ($i, k \le 2$) clusters ($a = 1.4$ Å is the bond length and N_{He} is the buffer gas (helium) concentration) and $W_{ik} \approx \exp(-5800/kT)$ for the large ones. Following [7], we reduced the probability of coagulation for selected fullerenes ($i = 60$, 70, 74, etc.) and some other species so as to reflect their stability.

Here, we present the results of solving Eqs. (1)–(5) for the following values of flow parameters in a flat turbulent jet: $N_{C0} = 10^{16}$ cm^{-3}; $U_0 = 10^4$ cm/s; $T_0 = 5000$ K; $r_0 = 0.5$ cm. The initial system was composed of carbon

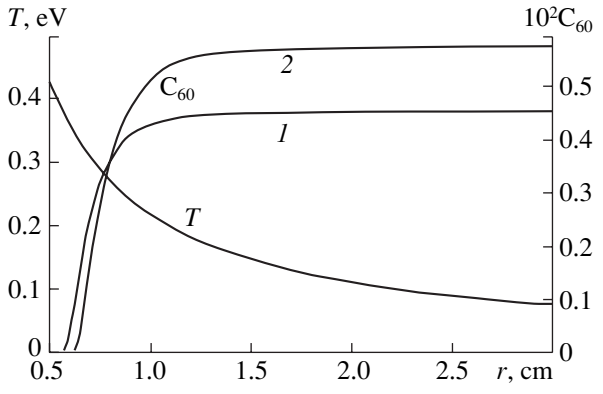

Fig. 2. Profiles of the jet temperature T and the fullerene C_{60} yield calculated (*1*) without and (*2*) with allowance for cluster charging.

monomers and approximately corresponds to an equilibrium composition at the given initial temperature. Note that, for $r \geq 3$ cm, the flow parameters are considered constant, their values decreasing to 1/6 of the initial values. The impurity metal was scandium, known to possess a low ionization potential. Scandium additives provided for the electron density N_e in the range from 10^8 to 10^{15} cm^{-3}, depending on the molar fraction and temperature.

Figure 1 shows evolution of the cluster size distribution for $x = 8.9$ (*1*), 14.1 (*2*), and 891 (*3*), corresponding to the distances $r = 0.54$, 0.57, and 9.2 cm, respectively. Solid curves represent the distributions calculated with neglect of the charges on clusters, while dotted curves are constructed with allowance for the effect of cluster charging. In the initial stage, the rate of coagulation is markedly higher for uncharged clusters, but eventually the trend changes to the opposite. This behavior is related to the dynamics of cluster charging. As can be seen from the inset in Fig. 1, small clusters predominantly bear a positive charge (due to ionization). In the course of jet expansion, the small clusters exhibit recharging to acquire a negative charge at $r > 0.75$ cm. The greater the cluster size, the later the moment of the charge sign reversal. For this reason, the growth rate of charged clusters exhibits a sharp increase within the interval of $r \approx 0.8$–1.25 cm.

Figure 2 illustrates the dynamics of variation of the concentration of fullerene C_{60} in the two cases under consideration and shows the jet temperature profile. This analysis confirms the previous conclusion [6] that there exists an optimum density of free electrons that provides for the maximum yield of fullerenes (in this example, ~10^9 cm^{-3}). At the same time, these results only outline general trends in the processes studied, detailed description requiring a knowledge of cluster charging kinetics. In conclusion, it should also be noted that the absolute values of fullerene yield strongly depend on the reactivity of clusters (W_{ik}) and the profiles of hydrodynamic parameters of the gas–plasma flow.

Acknowledgments. This study was supported by the INTAS Foundation, grant no. 2399.

REFERENCES

1. Yu. E. Lozovik and A. M. Popov, Usp. Fiz. Nauk **167**, 751 (1997) [Phys. Usp. **40**, 717 (1997)].
2. W. Kratschmer, K. Fostiropoulos, and D. R. Huffman, Chem. Phys. Lett. **170**, 167 (1990).
3. H. W. Kroto, J. R. Heath, S. C. O'Brien, *et al.*, Nature **318**, 162 (1985).
4. G. N. Churilov, Prib. Tekh. Éksp., No. 1, 1 (2000).
5. D. V. Afanas'ev, G. A. Dyuzhev, and V. I. Karataev, Pis'ma Zh. Tekh. Fiz. **25** (5), 35 (1999) [Tech. Phys. Lett. **25**, 182 (1999)].
6. G. N. Churilov, A. S. Fedorov, and P. V. Novikov, Carbon **41**, 173 (2003).
7. O. A. Nerushev and G. I. Sukhinin, Zh. Tekh. Fiz. **67** (2), 41 (1997) [Tech. Phys. **42**, 160 (1997)].
8. G. Kresse and J. Furthmuller, Comput. Mater. Sci. **6**, 15 (1996).
9. N. I. Alekseev and G. A. Dyuzhev, Zh. Tekh. Fiz. **72** (5), 121 (2002) [Tech. Phys. **47**, 634 (2002)].
10. G. S. Romanov, K. L. Stepanov, and L. K. Stanchits, Zh. Prikl. Spektrosk. **62**, 181 (1995).

Translated by P. Pozdeev

Technical Physics Letters, Vol. 29, No. 11, 2003, pp. 930–932. Translated from Pis'ma v Zhurnal Tekhnicheskoĭ Fiziki, Vol. 29, No. 22, 2003, pp. 16–22.

The Spectra of Electrons Scattered on Metastable Magnesium and Strontium (…$nsnp^3P_{0.2}$) Atoms

I. I. Shafranyosh* and V. I. Marushka

Uzhgorod National University, Uzhgorod, Ukraine

** e-mail: shafr@iss.univ.uzhgorod.ua*

Received May 6, 2003

Abstract—Elastic and inelastic electron scattering on magnesium and strontium atoms occurring in the ground and metastable states was studied by electron spectroscopy in crossed beams. The electron energy loss peaks due to the superelastic scattering on metastable magnesium and strontium (…$nsnp^3P_{0.2}$) atoms were observed for the first time. This result is indicative of a high efficiency of the scattering process under consideration, comparable with the efficiency of elastic scattering and excitation of the lower atomic levels. © *2003 MAIK "Nauka/Interperiodica".*

Introduction. The interaction of electrons with atoms in metastable states differs in many respects from the interaction with atoms in the ground state, which is related to differences in the initial properties (excitation energy, polarizability, dimensions) of atomic targets in the two cases. In particular, it was established [1, 2] that cross sections for excitation of the spectral transitions from metastable states in magnesium and strontium atoms are greater by at least two orders of magnitude than the analogous values for transitions from the ground state.

In this context, it was of interest to compare the energy spectra of electrons scattered from atoms in the ground and metastable states in the same experiment, since the results would provide illustrative data on the relative probability of excitation of the lower atomic energy levels. In addition, there is still an open question concerning the possible de-excitation (second order collisions) of metastable states by electron impact.

Experimental setup. The investigation was performed in the geometry of crossed electron and atomic beams. The experimental setup comprised a collision chamber with pumping facilities, the sources of electrons and atoms, and an electron spectrometer including the electron energy analyzer and a system measuring the current of scattered electrons. In the experiments with magnesium, the electron beam was generated by a five-electrode electron gun, while the beam scattered from strontium atoms was obtained using a 90° cylindrical monochromator. Figure 1 presents a scheme used for recording the electron energy loss spectra. The primary electron beam parameters were as follows: electron energy, 10–15 eV; beam current in the collision zone, ~25 and 2 μA; and the electron energy scatter, ~0.4 and 0.2 eV (for the electron gun and monochromator, respectively).

The beams of atoms in the ground state were obtained using a thermal source of the effusion cell type. The beams of metastable atoms were obtained using a discharge technique described in detail (together with the method for determining the density of metastable atoms) elsewhere [3, 4].

The scattered electron energy analyzer is based on a 127° cylindrical capacitor with molybdenum electrodes, the inner and outer radii being 32.7 and 37.5 cm, respectively. The interelectrode potential was varied

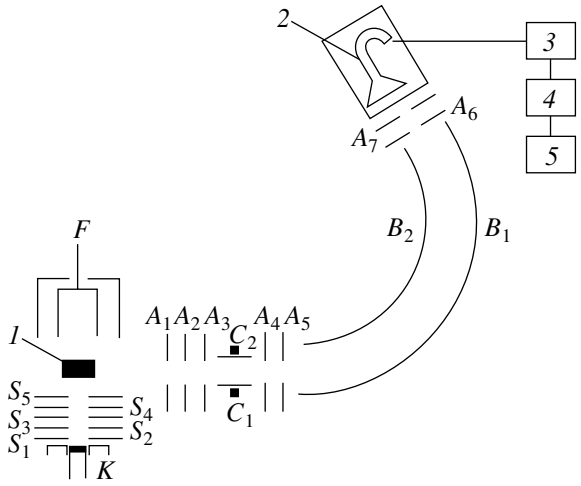

Fig. 1. Schematic diagram of the experimental arrangement for measuring the energy loss spectra of electrons scattered in crossed beam geometry: (*K*) cathode; (S_1–S_5) electron gun electrodes; (*F*) electron detector; (A_1–A_7) electrodes of 127° cylindrical analyzer; (C_1, C_2) plates of correcting capacitor; (B_1, B_2) plates of 127° cylindrical capacitor; (*1*) atomic beam; (*2*) channeltron; (*3*) preamplifier and broadband amplifier; (*4*) pulse count rate meter; (*5*) *X*–*Y* recorder.

within 2–5 V, while the correcting capacitor voltage was 0–1 V.

The system for detecting scattered electrons operates in a pulse mode with continuous sweep and signal recording in the analog form. This system included an electron detector, a signal amplifier, a sweep generator, and an *X*–*Y* recorder. Electrons were detected by a channeltron of the VEU-6 type.

The electron spectrometer with parts of the detection scheme was mounted on a flange inside the collision chamber. Prior to measurements, the surface of electrodes in the electron gun and energy analyzer was subjected to prolonged heating and cleaning under high vacuum conditions. The crossed beam experiments were performed in a vacuum of $\sim 3 \times 10^{-7}$ Torr.

Method of investigation. A beam of species of the element studied, containing atoms in the ground and metastable states, intersected in the zone of collisions at right angle to a primary electron beam. The scattered electrons were detected by the channeltron (VEU-6) at 90° relative to the electron and atomic beams. The measurements were performed in the energy loss mode, whereby the incident electron energy is fixed and the analyzer is sequentially tuned so as to transmit the groups of electrons scattered with various energies. The detection system operated as follows. Single electron pulses from the output of VEU-6, amplified by a preamplifier and a broadband amplifier, were transferred to the pulse count rate meter. The analog signal proportional to the count rate was fed to the *Y* input of the recorder. A sweep generator (based on a digit-to-analog converter of the F4810/1 type) provided linear scanning over the energy spectrum. The scan potential (varied from 0 to 10 V) was applied simultaneously to the entrance gap (A_5) of the analyzer and the *X* input of the recorder.

Using this technique, it is possible to record the energy spectra of electrons scattered from atoms in both the ground and metastable states. The primary electron beam energy was calibrated to within ±0.1 eV using the current–voltage characteristic. The energy scale in the loss spectrum was calibrated (to within ±0.15 eV) relative to the peak of elastically scattered electrons.

The proposed method was verified and the optimum regime of spectrometer operation was selected in control experiments, whereby the energy loss spectra of electrons scattered on magnesium and strontium atoms in the ground state were compared with the published data [5, 6] to show satisfactory agreement. The energy resolution level achieved with the given spectrometer (~0.4 eV for the electron gun and ~0.2 eV for the monochromator) was sufficient to separate the deepest excited levels of magnesium and strontium atoms. Below we present the spectra measured using a primary electron beam energy of 15 eV, which provided for the best signal to noise ratio.

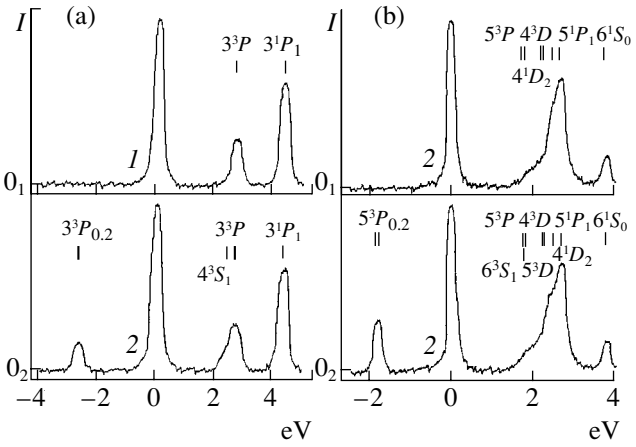

Fig. 2. Energy loss spectra of electrons scattered on a beam of (a) magnesium and (b) strontium atoms (*1*) in the ground state and (*2*) in both ground and metastable states (primary electron beam energy, 15 eV; scattering angle, 90°).

Results and discussion. Figure 2 shows the energy spectra of electrons scattered from (a) magnesium and (b) strontium atoms in the ground state and in metastable ($n^3P_{0.2}$) states, plotted as the current of scattered electrons (in arbitrary units) versus the electron energy loss (in electronvolts). Let us consider first the scattering on magnesium atoms in the ground state (Fig. 2a, curve *1*). The dominating zero-energy peak characterized the process of elastic scattering on atoms in the ground 3^1S_0 state. The region of positive losses contains two peaks (~2.7 and ~4.3 eV) corresponding to excitation of the lower triplet 3^3P and singlet 3^1P states, respectively. Since the triplet structure of the 3^3P term is very narrow ($\Delta E \approx 0.01$ eV), peaks corresponding to excitation of the triplet components are unresolved. In the region of negative losses, the spectrum exhibits only statistical variations of the background signal.

A different pattern is observed when the atomic beam contains species in the metastable states (Fig. 2a, curve *2*). In the region of positive energy losses, the difference is manifested by broadening of the first peak (~2.7 eV) caused by the contribution due to excitation of the 4^3S_1 level from metastable $3^3P_{0,2}$ states, in agreement with the optical data [1]. No differences were revealed between the peaks of elastic scattering in spectra *1* and *2*. In the region of negative losses, a well manifested peak appeared at ~2.7 eV (having no analog in spectrum *1*). We attribute this feature to the process of de-excitation of the metastable $3^3P_{0.2}$ states in magnesium atoms, leading to the formation of a fast electron and an atom in the ground state (in literature, this process is referred to as superelastic electron scattering).

Let us proceed to the results for strontium. It should be noted that the useful signal for the scattering on strontium is much higher compared to that for magnesium. The presence of a singlet metastable 4^1D_2 state required the energy resolution of the spectrometer to be

increased, which was achieved using a 90° monochromator as the electron beam source. Similar to the case of magnesium, there are significant differences between the spectra of electrons scattered on strontium atoms in the ground and metastable states. The former spectrum (Fig. 2b, curve *1*) displays a dominating zero-energy peak of elastic scattering on the ground 5^1S_0 state. In the region of positive losses, the spectrum exhibits an intense broad line peaked at ~2.5 eV. This line corresponds to the excitation of several levels (4^3D, 4^1D, and 5^1P_1, with the energy losses of ~2.2, 2.5, and ~2.7 eV, respectively). The resolution of our spectrometer was insufficient to resolve these components. In the region of ~3.8 eV, there is a well-manifested peak corresponding to excitation of the first singlet 6^1S_0 level. A peak due to excitation of the metastable triplet 5^3P levels (with an energy loss of ~1.8 eV) is manifested only by a weakly pronounced feature at a threshold of the total loss contour.

The spectrum of electrons scattered on metastable strontium atoms (Fig. 2b, curve *2*) is qualitatively similar to, but more complicated than the spectrum described above for metastable magnesium atoms. For the positive energy losses of ~1.8 and ~2.4 eV, the total contour exhibits broadening reflecting the contributions due to excitation of the 6^3S_1 and 5^3D levels from metastable 5^3P states. In the region of negative losses, a new feature is observed at ~1.8 eV that was absent in spectrum *1*. We assign this peak to the process of superelastic scattering on metastable triplet $5^3P_{0.2}$ states of strontium. The absence of a peak corresponding to the superelastic scattering of electrons on the 4^1D_2 state is explained by a small density of such atoms in the collision zone. Our experiments showed that the fraction of metastable singlet 4^1D_2 states in the atomic beam of strontium is 40–50 times smaller than the fraction of metastable triplet $5^3P_{0.2}$ states.

Conclusion. The energy spectra of electrons scattered on metastable magnesium and strontium atoms were obtained for the first time and compared to the spectra of scattering on atoms in the ground state. The comparative analysis revealed differences in the process of excitation of the 4^3S_1 magnesium and the 6^3S_1 and 5^3D strontium levels for atoms in the ground and metastable states. The effective superelastic scattering of electrons on the metastable triplet states of magnesium and strontium atoms was observed for the first time.

REFERENCES

1. I. I. Shafranyosh, T. A. Snegurskaya, and I. S. Aleksakhin, Opt. Spektrosk. **76**, 23 (1994) [Opt. Spectrosc. **76**, 20 (1994)].
2. I. S. Aleksakhin, F. I. Nebesnyĭ, Ya. N. Semenyuk, *et al.*, Opt. Spektrosk. **64**, 431 (1988) [Opt. Spectrosc. **64**, 256 (1988)].
3. I. I. Shafranyosh and M. O. Margitich, Z. Phys. D **37** (2), 97 (1996).
4. N. A. Margitich and I. I. Shafranyosh, Ukr. Fiz. Zh. **45** (1), 31 (2000).
5. S. M. Kazakov and O. V. Khristoforov, in *Interinstitute Collection of Works "Metastable States of Atoms and Molecules and Methods of Their Study"* (Chuvashskiĭ Gos. Univ. Press, Cheboksary, 1981), pp. 148–170.
6. S. M. Kazakov, N. I. Romanyuk, O. V. Khristoforov, and O. B. Shpenik, Opt. Spektrosk. **59**, 38 (1985) [Opt. Spectrosc. **59**, 22 (1985)].

Translated by P. Pozdeev

Technical Physics Letters, Vol. 29, No. 11, 2003, pp. 933–935. Translated from Pis'ma v Zhurnal Tekhnicheskoĭ Fiziki, Vol. 29, No. 22, 2003, pp. 23–28.

Synthesis and Properties of Plasma-Deposited Carbon Condensates

G. A. Glushchenko[a], N. V. Bulina[a], P. V. Novikov[b], G. N. Bondarenko[c], and G. N. Churilov[a,*]

[a] *Kirensky Institute of Physics, Siberian Division, Russian Academy of Sciences, Krasnoyarsk, Russia*
** e-mail: churilov@iph.krasn.ru*
[b] *Krasnoyarsk State Technical University, Krasnoyarsk, Russia*
[c] *Institute of Chemistry and Chemical Technology, Siberian Division, Russian Academy of Sciences, Krasnoyarsk, Russia*

Received March 20, 2003; in final form, June 2, 2003

Abstract—Structural data, thermal characteristics, and theoretically calculated binding energies are reported for a graphite condensate obtained by carbon deposition from plasma. It is demonstrated that this condensate can be effectively used in self-propagating high-temperature synthesis processes. © *2003 MAIK "Nauka/Interperiodica".*

Elementary carbon is available in a variety of forms exhibiting different, sometimes opposite characteristics. On the one hand, this material is extremely active, being capable of forming ten times more compounds than all other elements together, while, on the other hand, carbon is absolutely inert with respect to some of the most aggressive reactants.

It is a peculiarity of graphite that samples can significantly differ in their structure and properties, depending on the conditions of synthesis [1–5]. In the course of thermal treatment, graphite exhibits an increase up to 3.44 Å in the spacing between layers, which are parallel to each other but possess no mutual azimuthal orientation. This type of graphite is well known and called turbostrate [5].

This paper reports on the results of our investigation of a product of this kind that was synthesized as reported previously and called thermolysis residue (TR) [6]. The TR was obtained in a plasmachemical reactor described in detail elsewhere [7]. In this setup, a carbon–helium plasma is generated by sputtering spectral-purity carbon rods made of the graphite referred to below as initial, possessing a hexagonal structure with the crystal lattice parameters $a = 2.462$ Å and $c = 6.732$ Å. A TR deposit was formed in the course of rapid cooling and crystallization from carbon–helium plasma and deposited on a relatively cold external ring electrode of the reactor.

The results of our investigation showed that the structure of this graphite condensate is determined by the conditions of cooling of the ring electrode on which deposition takes place. At an average temperature of this electrode not exceeding 400°C, a deposit is formed with the same lattice parameters as those of the initial graphite. At higher temperatures, a carbon condensate formed on the electrode contains both the initial graph-

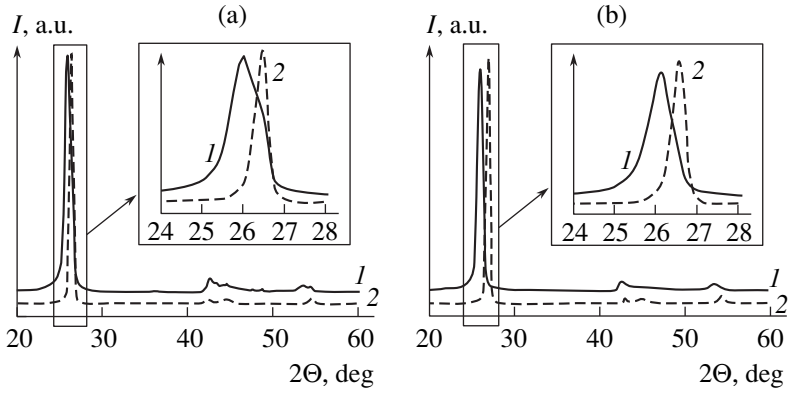

Fig. 1. X-ray diffraction patterns of (a) initial graphite with TR and (b) pure TR condensate showing sample peak (solid curves *1*) in comparison to the diffraction peak (dashed curve *2*) of the initial graphite.

1063-7850/03/2911-0933$24.00 © 2003 MAIK "Nauka/Interperiodica"

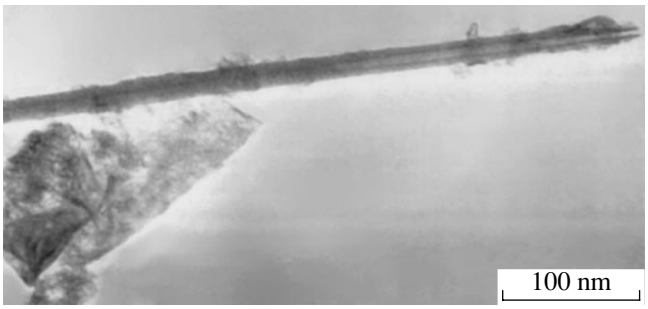

Fig. 2. Electron-microscopic image of a carbon condense, showing a multiwall nanotube and a turbostrate graphite particle.

ite and TR phases (Fig. 1). When the electrode temperature is increased up to 800°C or above, the condensate consists entirely of TR. In this material, the spacing between graphite layers is increased by 0.06 Å (a = 2.462 Å and c = 6.852 Å) as compared to that in the initial graphite. These conclusions are based on the results of X-ray diffraction measurements performed for powder samples on a DRON-4 diffractometer. An increase in the interlayer distance is usually explained by random packing of graphite layers in the course of rapid condensation of carbon from the plasma [5].

Electron-microscopic investigations performed using a scanning electron microscope (SEM) of the REMMA-202 type (Russia; magnification, ×300) showed that the TR phase consists of sintered spheroidal species with dimensions ranging from 0.3 to 10 μm. We have finely comminuted a TR sample by grinding and studied the material in a transmission electron microscope (TEM) of the JEM-100C type (JEOL, Japan). It was found that the TR phase contains, besides graphite species, multiwall carbon nanotubes (Fig. 2). Most of these nanotubes have lengths ranging from several dozen up to several hundred and even thousands of nanometers, with internal diameters from a few to several dozen nanometers. The electron diffraction patterns obtained from TR species and nanotubes coincide, from which it follows that the spacing of graphite layers in both TR graphite species and nanotubes is the same (about 3.42 Å). Quantitative estimates showed that the fraction of nanotubes is usually small, within 1–2%.

Experimental data on the particle size and combustion front velocity in powdered titanium–carbon mixtures

Mixture composition	Carbon particle size, μm	Combustion front velocity, mm/s
Titanium–graphite	10	8
Titanium–soot	10^{-2}	10
Titanium–TR	10	18

The binding energies of carbon for the TR and usual graphite structures were calculated within the framework of the density functional formalism using a VASP program package [8]. The results showed that a difference between the energy per mole of carbon in the TR phase and initial graphite amounts to 5.8 kJ, which implies that 5.8 kJ/mol would be liberated upon the transition from TR to the initial graphite. Therefore, TR can be expected to exhibit a higher chemical activity related to the greater potential energy stored in the TR structure. This has to be manifested in a greater efficiency of chemical reactions involving carbon in the TR form.

We have studied the samples of initial graphite and TR by means of differential thermal analysis on a Q-1000 (MOM, Hungary) derivatograph, whereby the samples were heated from 24 to 1000°C. It was established that the initial graphite burns in the temperature interval from 660 to 890°C, while the TR burns in the interval from 570 to 850°C, the process being exothermal. The fact that the TR burns at lower temperatures is evidence that the TR phase is actually more chemically active than the initial graphite, in agreement with theoretical estimates.

The next check for chemical activity of the TR phase was a practically important reaction of the formation of titanium carbide by method of self-propagating high-temperature synthesis (SHS). The initial components were titanium and TR powders (see table). For comparison, the SHS process was also performed with the carbon component in the form of initial graphite and X-ray amorphous soot. The average size of titanium particles was 100 μm. The initial mixture contained titanium and carbon taken in a stoichiometric ratio, and the initial charge was pressed to a density of about 0.5 g/cm^3. The samples were placed into an SHS reactor chamber evacuated to a residual pressure of 10^{-3} Pa. The SHS reaction was initiated by heating the sample end (occurring at an initial temperature of 24°C) through contact with a red-hot graphite rod.

The SHS synthesis of titanium carbide using carbon in the form of graphite and soot proceeded at a combustion wave front propagation velocity corresponding to the published data [9]. In the case of a reaction involving the TR, the combustion front velocity was about twice as large as that for graphite and soot (see table).

In summary, the results of our investigations showed that the thermolysis residue consists of spheroidal carbon species including turbostrate carbon and multiwall carbon nanotubes. The distance between graphite planes in both turbostrate graphite and nanotubes is 3.42 Å. Quantum-chemical estimates showed that the energy difference per mole of carbon in the TR and initial graphite is 5.8 kJ, so that this amount of energy had to be liberated upon the TR–graphite conversion. It was demonstrated that the energy saturation of TR can be effectively used, for example, in the SHS synthesis of refractory carbides.

Work on the synthesis and investigation of TR condensates with variable content of nanotubes is in progress. We will also study the possibility of using such materials in various applications, for example, as sorbents for chromatography.

Acknowledgments. This study was supported by the INTAS Foundation (grant no. 01-2399), the Russian Foundation for Basic Research (project no. 03-03-32326), and the Federal Targeted Scientific-Technological Program "R&D in Selected Science and Technology Directions."

REFERENCES

1. E. Breval, M. Klimkiewicz, D. K. Agrawal, *et al.*, Carbon **40**, 1017 (2002).
2. Y. M. Hoi and D. D. L. Chung, Carbon **40**, 1134 (2002).
3. Y. Kuga, M. Shirahige, and Y. Ohira, Carbon **40**, 695 (2002).
4. *Abstracts of the 1st International Conference "Carbon: Basic Problems in Materials Science and Technology"* (Moscow, 2002).
5. S. E. Vyatkin, A. N. Deev, V. G. Nagornyĭ, V. S. Ostrovskiĭ, A. M. Sigarev, and G. A. Sokker, *Nuclear Graphite* (Atomizdat, Moscow, 1967).
6. G. N. Churilov, L. A. Soloviev, Ya. N. Churilova, *et al.*, Carbon **37**, 427 (1999).
7. G. N. Churilov, Prib. Tekh. Éksp., No. 1, 5 (2000).
8. G. Kresse and J. Furthmuller, Phys. Rev. B **54**, 11169 (1996).
9. A. G. Merzhanov, *Self-Propagating High-Temperature Synthesis: Current Problems*, Ed. by Yu. M. Kolotukin (Khimiya, Moscow, 1983), pp. 5–45.

Translated by P. Pozdeev

Technical Physics Letters, Vol. 29, No. 11, 2003, pp. 936–937. Translated from Pis'ma v Zhurnal Tekhnicheskoĭ Fiziki, Vol. 29, No. 22, 2003, pp. 29–32.

Conductivity and Dielectric Properties of Iron-Containing Nanocomposites

N. M. Ushakov*, K. V. Zapsis, and I. D. Kosobudskiĭ

Saratov Branch, Institute of Radio Engineering and Electronics, Russian Academy of Sciences, Saratov, Russia

** e-mail: nmu@mail.saratov.ru*

Saratov State Technical University, Saratov

Received April 21, 2003; in final form, June 4, 2003

Abstract—We have studied the electric conductivity and dielectric properties of composites comprising iron nanoparticles dispersed in a low-density polyethylene matrix. The specific conductivity and dielectric constant as functions of the differential mass fraction of iron nanoparticles in such composites occurring in the semiconductor state are described by power relations with the average exponents (critical indices) $t = s = 1.5 \pm 0.3$. The regions of applicability, in which the percolation model provides adequate description of the electric conductivity and dielectric properties of the nanocomposites, are determined. © *2003 MAIK "Nauka/Interperiodica".*

It is known that the properties of disordered (randomly inhomogeneous) media representing composites containing metal nanoparticles (nanocomposites) depend in a critical manner on the so-called percolation concentration (volume fraction of a metal in the matrix) or mass fraction p of the metal [1, 2]. According to this, a volume cluster formed in the nanocomposite when the percolation concentration p exceeds a certain critical value p_c renders the polymer conducting. For small metal concentrations ($p < p_c$), the metal clusters are spatially separated and the electric properties of the nanocomposite possess a semiconductor or dielectric character.

Among the transition metals employed in nanocomposites, an important position is occupied by iron. However, the electric and dielectric properties of iron-containing nanocomposites with $p < p_c$ are still insufficiently studied. This is related to the fact that the percolation theory adequately describes the properties of such disordered media only in the vicinity of the critical percolation concentration p_c [3]. Therefore, investigation of the electric and dielectric properties of iron-containing nanocomposites in the entire range of $p < p_c$ is of importance.

Below we present the results of an experimental study of the electric conductivity and dielectric properties of composites comprising iron nanoparticles dispersed in a low-density polyethylene (LDPE) matrix. These characteristics were determined as functions of the differential mass fraction of iron in these composites. The regions of applicability, in which the percolation model provides adequate description of the observed experimental behavior of the conductivity and the dielectric constant of the nanocomposites are determined.

The iron-containing nanocomposites were synthesized by thermal decomposition of unstable metalorganic compounds such as iron pentacarbonyl, as described in detail elsewhere [4]. The resulting Fe–LDPE nanocomposites were in the form of powders possessing gray or black color, depending on the metal content. The samples of required geometry for the electrical measurements were prepared by pressing powders in a mechanical press with an appropriate mold. In addition, the nanocomposites can be obtained in the form of 10- to 30-μm-thick films deposited onto any (e.g., glass) substrate.

The size of metal nanoparticles in the composite, as determined from the data of small-angle X-ray scattering, ranged within 4–15 nm. The electric conductivity and dielectric constant were measured using a measuring bridge of the E7-12 type at a frequency of 1 MHz. It was assumed that the properties of nanocomposites could be described using an equivalent scheme comprising ohmic conductivity and capacitive reactivity connected in parallel. As is known, the results of dc and ac measurements coincide in the case of a purely ohmic sample resistance [5]. In the general case, the mechanisms of dc and ac conductivity can be absolutely different.

The resistivity (conductivity) and dielectric constant were determined using standard techniques, by measuring the $G_0(p)$ and $C_0(p)$ and using the formula of a plane capacitor. The distance between the capacitor plates was varied from 0.4 to 1 mm. The capacitor plate area was ~10 mm^2. The mass fraction of iron in the samples was varied from 0.01 to 0.3. As the mass fraction p increases in this interval, the conductivity grows from 8×10^{-7} to 6×10^{-6} S/m, while the dielectric constant (relative permittivity) increases from 2.5 to 5.5. The loss tangent of the nanocomposite was within $\tan\delta \simeq$

1063-7850/03/2911-0936$24.00

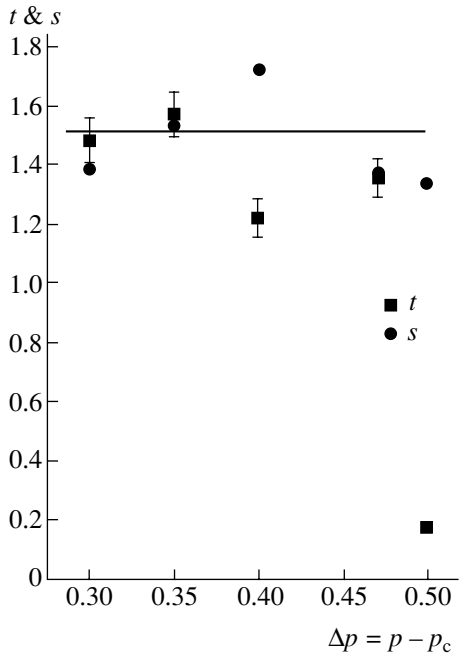

A plot of the critical indices t and s (for the conductivity and the dielectric constant, respectively) versus the differential mass fraction of iron $\Delta p = p - p_c$ in Fe–LDPE nanocomposites.

10^{-2}–10^{-1}. For comparison, the conductivity, dielectric constant, and loss tangent of pure LDPE are 10^{-15}–10^{-14} S/m, 2.5–2.8, and ~10^{-4}, respectively [6].

According to the percolation theory, the macroscopic conductivity and dielectric constant of a composite material obey the relations

$$G_0(p) \sim G_m(\Delta p)^t, \quad \varepsilon(p) \sim |\Delta p|^{-s}, \quad \Delta p = p - p_c, \quad (1)$$

where G_m is the conductivity of the metal component. The exponents (critical indices) t and s are universal parameters that allow one to determine the dispersion of conductivity and dielectric constant of the given nanocomposite [7].

The values of critical indices t and s in various regions of the differential mass fraction of iron in the nanocomposite $\Delta p = p - p_c$ are plotted in the figure. These data were obtained through mathematical transformation of the measured values of $G_0(p)$ and $\varepsilon(p)$. For a three-dimensional conductivity lattice ($d = 3$), the experimental average values of the critical indices for the conductivity and dielectric constant are equal (to within an experimental uncertainty of 5%), $t = s \simeq 1.5$, and virtually coincide with results obtained by other researchers [3, 7], except for the conductivity of nanocomposites with $\Delta p \longrightarrow 0.5$ ("dielectric" phase).

The results of our experimental investigation of the electric conductivity and dielectric properties of iron-containing nanocomposites based on an LDPE matrix show the possibility of creating artificial media with controlled electrical and dielectric properties and confirmed validity of the percolation theory.

REFERENCES

1. S. P. Gubin, Colloids Surf. A **202**, 155 (2002).
2. I. D. Kosobudskiĭ, Izv. Vyssh. Uchebn. Zaved., Khim. & Khim. Tekhnol. **43** (4), 3 (2000).
3. B. I. Shklovskiĭ and A. L. Efros, *Electronic Properties of Doped Semiconductors* (Nauka, Moscow, 1979; Springer-Verlag, New York, 1984).
4. I. D. Kosobudskiĭ, V. P. Sevost'yanov, and G. Yu. Yurkov, Izv. Vyssh. Uchebn. Zaved., Khim. & Khim. Tekhnol. **43** (1), 135 (2000).
5. F. Gutmann and L. E. Lyons, *Organic Semiconductors* (Wiley, New York, 1967; Mir, Moscow, 1970).
6. D. M. Kazarnovskiĭ and S. A. Yamanov, *Radio-Engineering Materials* (Vyssh. Shkola, Moscow, 1972).
7. A. K. Sarychev and F. Brouers, Phys. Rev. Lett. **73**, 2895 (1994).

Translated by P. Pozdeev

Technical Physics Letters, Vol. 29, No. 11, 2003, pp. 938–940. Translated from Pis'ma v Zhurnal Tekhnicheskoĭ Fiziki, Vol. 29, No. 22, 2003, pp. 33–38.

Simulation of Ion Sputtering of Copper Clusters from Single Crystal Graphite Surface

G. V. Kornich*, G. Betz, V. I. Zaporojtchenko, and A. I. Bazhin

Zaporozhye National Technical University, 69063 Zaporozhye, Ukraine
** e-mail: gkornich@zntu.edu.ua*
Institut für Allgemeine Physik, Technische Universität Wien, A-1040 Wien, Austria
Technische Fakultät, Christian Albrechts Universität, 24143 Kiel, Germany
Donetsk National University, 83114 Donetsk, Ukraine

Received May 21, 2003

Abstract—The sputtering of clusters consisting of 13 and 75 copper atoms from a (0001) graphite surface bombarded by normally incident 200-eV Ar^+ ions was studied by molecular dynamics method. The angular distribution of sputtered copper atoms, their energies, and the sputtering yields are discussed. © *2003 MAIK "Nauka/Interperiodica".*

We have simulated the sputtering of copper clusters from a (0001) single crystal graphite surface bombarded by 200-eV Ar^+ ions at normal incidence by molecular dynamics method [1]. The targets comprised two clusters consisting of 13 (13Cu) and 75 (75Cu) copper atoms on single crystal substrates representing four atomic layers, each containing 792 and 1500 carbon atoms, respectively. Both cluster–substrate systems were created via relaxation of the initially lone, energy-minimized copper clusters [2] on the free (0001) graphite surface. After a 10-ps relaxation, the maximum kinetic energy of Cu atoms in the clusters on the substrate did not exceed 0.02 eV per atom.

Copper atoms were assumed to interact via the many-body potential [3] directly matched at high interaction energies to the Born–Mayer potential [4]. The interaction between carbon atoms was described by the Tersoff potential [5] matched to the Ziegler–Biersack–Littmark potential via a function defined in the interval $x_0 < x < x_1$ in the form of a fifth-order polynomial,

$$\Phi(x) = a_0 + \sum_{i=1}^{5} a_i (x - x_0)^i,$$

with a_0 = 119.909 eV, a_1 = –619.745 eV/Å, a_2 = 1988.96 eV/Å^2, a_3 = –4918.48 eV/Å^3, a_4 = 6931.1 eV/Å^4, a_5 = –3873.41 eV/Å^5, x_0 = 0.5 Å, and x_1 = 0.98 Å. A minimum distance between carbon atoms in the (0001) plane was 1.46 Å, and the interplanar spacing was 3.35 Å. The interaction between (0001) atomic planes in the initial substrate was absent, since the cutoff radius of the Tersoff potential is 2.1 Å [5]. The interaction in Cu–C pairs was described by the Lennard-Jones potential [6] with a truncation radius of 3.75 Å. The periodic boundary conditions [1] and a dissipative layer [7] with neglect of thermal oscillations were set at the perimeter of graphite layers.

The equations of motion were solved by the Verlet method [4]. The maximum integration step did not exceed 4 fs. The development of each collision cascade was followed for 2 ps. The energy conservation law in each cascade simulated by molecular dynamics was obeyed to within 1%. The total number of simulations for each cluster was 500, with every new test run for the initial cluster–substrate system. The initial coordinates of Ar^+ ions were selected by a random number generator, so that their maximum energy of interaction with at least one Cu atom would be not less than 37 eV. In order to determine a contribution from the cluster boundary to the sputtering yield, additional series of 500 Ar^+ ions striking around both clusters were simulated, for which the maximum energy of interaction with each Cu atom did not exceed 37 eV, while not being less than 3.7 eV with at least one of these atoms. Copper atoms sputtered from the cluster at a polar angle greater than 90° (see below), but not reaching the model substrate by the end of the simulated collision cascade, were considered as particles mirror-reflected from the substrate surface.

The energy-minimized copper cluster on the free graphite surface represented a multilayer atomic system with virtually equal spacings between atomic layers parallel to the (0001) substrate plane. The chains of Cu atoms forming most open directions in the atomic structure of the 75Cu cluster were oriented along the $\langle 1\bar{1}00 \rangle$ type substrate directions every 60° around the normal to the surface.

Figure 1 shows the azimuthal distribution of the probability of sputtering single Cu atoms from the 75Cu cluster on the graphite surface. The azimuthal angle was measured from the [1000] direction counter-

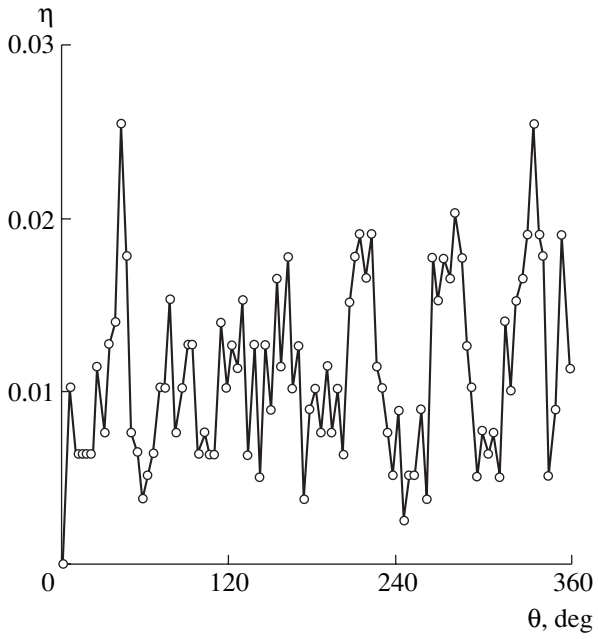

Fig. 1. The azimuthal distribution of the probability of sputtering single Cu atoms from the 75Cu cluster on the (0001) graphite surface.

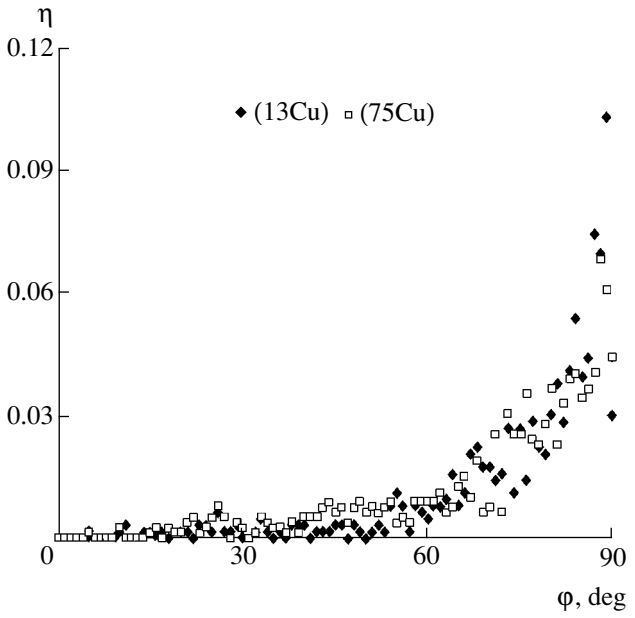

Fig. 2. The polar angular distribution of the probability of sputtering single Cu atoms from 75Cu and 13Cu clusters on the (0001) graphite surface.

clockwise in the (0001) plane on the graphite surface. The sectors near 30°, 210°, 270°, and 330° exhibit characteristic peaks in the sputtering probability. Mechanisms responsible for these peaks are related to similarly oriented atomic chains in the 75Cu cluster. The peaks in the sputtering probability anticipated in the vicinity of 90° and 150° were absent (Fig. 1), which is related to a broken order in the atomic structure of the model cluster surface in the corresponding regions. Still somewhat unclear is the azimuthal shift by ~10° of the main sputtering yield peaks relative to directions of the $\langle 1\bar{1}00 \rangle$ type. Azimuthal distribution of the copper dimer sputtering was not studied. No preferred azimuthal distribution of sputtered copper atoms, analogous to that for the 75Cu cluster, was observed for the 13Cu cluster.

The results of molecular dynamics simulations suggest that ion bombardment of copper clusters on the (0001) single crystal graphite surface may lead, under certain conditions, to the appearance of preferred azimuthal sputtering directions close to $\langle 1\bar{1}00 \rangle$. This phenomenon is apparently related to similar spatial orientations of the atomic structures of the surface copper clusters (this situation probably takes place in some other materials as well).

It was found that sputtered Cu–Cu dimers account for no more than 18% (75Cu) and 6% (13Cu) of the total sputtering yield from copper clusters under the conditions studied. The sputtering yields of copper in the form of both single Cu atoms and Cu–Cu dimers from 75Cu and 13Cu clusters amount to 1.92 and 1.35 atoms per ion, respectively. The average relative Ar^+ ion energy losses in the clusters were 61% (75Cu) and 50% (13Cu), which is consistent with a growth in the sputtering yield observed with increasing linear size of the clusters. An alternative calculation of the sputtering yield of Cu clusters, taking into account only backscattered Ar^+ ions and all sputtered Cu species, gives the yields of 2.72 and 2.27 atoms per ion for 75Cu and 13Cu, respectively. For Cu atoms sputtered only via cascades with backscattering of Ar^+ ions, the corresponding values are 2.5 and 1.9 atoms per ion.

Thus, calculation of the sputtering yield with neglect of the Ar^+ ions penetrating into the substrate, but with allowance of the corresponding copper species, leads to an uncertainty below 20%. Therefore, the average sputtering yield from the clusters of copper (or other heavy metals) on a graphite surface can be estimated taking into account only the degree of surface coverage of the bombarded surface and the intensity of backscattered Ar^+ ions. According to the results of simulations, the sputtering of graphite was insignificant despite average ion energy losses in the substrate reaching 25 and 40% of the initial energy (in the presence of 75Cu and 13Cu clusters, respectively).

Figure 2 shows the results of simulation of the polar angular distribution of the probability of sputtering single Cu atoms from copper clusters on the graphite surface. The polar angle was measured relative to normal to the substrate surface. As can be seen, the sputtering yield from both clusters sharply increases for angles above 60°, which is related to the fact that the side faces of clusters are open for the cascade Cu atoms leaving

the target. This is consistent with a sharp increase in the average energy of sputtered Cu atoms emitted at polar angles above 60°, suggesting that there are at least two possible mechanisms of sputtering. The first is the typical cascade-recoil mechanism leading to the preferential sputtering of atoms with low and medium energies (below 8 eV). Another, high-energy mechanism, is responsible for the yield of atoms with energies up to 30 eV at large polar angles. A significant factor in this process is the interaction of sputtered Cu atoms with atoms of the substrate surface.

REFERENCES

1. J. M. Haile, *Molecular Dynamics Simulation—Elementary Methods* (Wiley, New York, 1992).
2. G. Betz and W. Husinsky, Nucl. Instrum. Methods Phys. Res. B **122**, 311 (1997).
3. G. Betz, R. Kirchner, W. Husinsky, *et al.*, Radiat. Eff. Defects Solids **130**–**131**, 251 (1994).
4. W. Eckstein, *Computer Simulation of Ion–Solid Interactions* (Springer-Verlag, Berlin, 1991; Mir, Moscow, 1995).
5. J. Tersoff, Phys. Rev. B **39**, 5566 (1989).
6. S. Dorfman, K. C. Mundim, D. Fuks, *et al.*, Mater. Sci. Eng. C **15**, 191 (2001).
7. H. J. Berendsen, J. P. M. Postma, W. F. V. Gunsteren, *et al.*, J. Chem. Phys. **81**, 3684 (1984).

Translated by P. Pozdeev

Technical Physics Letters, Vol. 29, No. 11, 2003, pp. 941–943. Translated from Pis'ma v Zhurnal Tekhnicheskoĭ Fiziki, Vol. 29, No. 22, 2003, pp. 39–45.

Taking into Account the Radiation Pattern of a Practical Feed for a Luneberg Lens

D. V. Shannikov* and S. V. Kuzmin**

St. Petersburg State Polytechnic University, St. Petersburg, 195251 Russia

*e-mail: * shandv@pochtamt.ru; ** kuzminsv@pochtamt.ru*

Received May 28, 2003

Abstract—A method of taking into account the real feed radiation pattern for a Luneberg lens is proposed. According to this, the field of a feed with the given radiation pattern is expanded into series in spherical harmonics. Using this approach, it is possible to introduce the radiation patterns of real feeds into strict electrodynamic solution for a Luneberg lens, thus significantly refining a mathematical model of the antenna. © *2003 MAIK "Nauka/Interperiodica".*

Microwave radio systems employ various antennas, including those of the lens type. The Luneberg lens is an antenna of this type, representing a spherical lens with a graded radial index profile. Like any lens, this antenna allows a special field distribution to be readily created so as to ensure the radiation pattern with small side lobes, the possibility of operating in a broad frequency range without readjustment, and the absence of radiation screening by the feed. The Luneberg lens possesses a central symmetry, which facilitates mechanical scanning and (in case of several feeds) allows various independent radiation patterns to be obtained. The main application fields of such antennas are satellite communications and remote sounding.

The Luneberg lens is a rather complicated system difficult to manufacture. For this reason, it is a common practice to pass from continuous to stepped index profile, that is, from the Luneberg lens to a multilayer spherically stratified lens composed of homogeneous dielectric layers. It has been established that a relatively small number of layers is sufficient, provided that the characteristics of the multilayer spherical lens are identical to those of the Luneberg lens [1, 2]. The required number of layers is given by the relation [2]

$$N \geq \mathrm{int}\left(4.34\log_2\left(\frac{D}{\lambda}\right) - 8.74\right),$$

where D is the antenna diameter.

Using presently available computational facilities, it is possible to calculate the field generated by a multilayer spherical lens-antenna proceeding from the rigorous electrodynamic solution of the problem. Solutions of such problems, approaches to these solutions, and numerous results of numerical and physical experiments can be found in extensive literature (see, e.g., [1–5]. However, in all these cases the lens is excited by electric or magnetic dipoles, by the Huygens source, or by a combination of these. As is known, the radiation pattern of the whole antenna is determined to a considerable extent by the feed radiation pattern [2].

Previously [2], we have used a feed in the form of a spherical surface with a given current distribution. This system has a radiation pattern close to that of a real feed such as, for example, a spherical horn. In this paper, we propose a method of taking into account the radiation pattern of any real feed. Detailed description of the problem solution for a multilayer spherical lens with homogeneous dielectric layers is quite lengthy. In view of the short Letter format, we present only the main features of this solution.

First, we expand the source field into a series in spherical harmonics [6],

$$E_r = \frac{1}{r}\sum_{n=0}^{\infty}\sum_{m=-n}^{+n} n(n+1)U^e_{rnm},$$

where

$$U^e_{rnm} = P^m_n(\cos\vartheta)e^{-im\varphi}\begin{cases} h^{(2)}_n(kr)F^{2e}_{nm}, & r > r', \\ j_n(kr)F^{1e}_{nm}, & r < r' \end{cases}$$

$$F^{se}_{nm} = -\frac{2n+1}{n(n+1)}\frac{(n-m)!}{(n+m)!}\frac{k}{4\pi\omega\varepsilon_a}$$

$$\times\int_V\left\{ j^e_r\frac{n(n+1)}{r'}R^s_n(kr')P^m_n(\cos\vartheta')\right.$$

$$+ j^e_\vartheta\frac{1}{r'}\frac{\partial}{\partial r'}(r'R^s_n(kr'))\frac{\partial P^m_n(\cos\vartheta')}{\partial\vartheta'}$$

$$\left.+ j^e_\varphi\frac{im}{\sin\vartheta'}\frac{1}{r'}\frac{\partial}{\partial r'}(r'R^s_n(kr'))P^m_n(\cos\vartheta')\right.$$

1063-7850/03/2911-0941$24.00 © 2003 MAIK "Nauka/Interperiodica"

$$+ j_\vartheta^m \frac{\omega\varepsilon_a m}{\sin\vartheta'} R_n^s(kr') P_n^m(\cos\vartheta') + j_\varphi^m i\omega\varepsilon_a R_n^s(kr') \frac{\partial P_n^m(\cos\vartheta')}{\partial\vartheta'}\Bigg\}$$

$$\times e^{im\varphi'} r'^2 \sin\vartheta' d\vartheta' dr' d\varphi'.$$

Here, $(r', \vartheta', \varphi')$ are the external current coordinates, $R_n^1(kr') = j_n(kr')$ are the spherical Bessel functions, and $R_n^2(kr') = h_n^{(2)}(kr')$ are the spherical Hankel functions. Analogous relations are valid for the radial components of the magnetic field.

Upon writing all relations and performing simple but cumbersome transformations, we arrive at an expression for the longitudinal component E_r of the electric field of a spherical radiating surface with a radius of R (angle ϑ is measured from the axis passing through the origin and the center of the sphere spaced from the origin by a distance b):

$$E_r = j_0 \frac{e^{-ikr}}{r^2} \sum_{n=1}^{\infty} (2n+1) I_n e^{in\frac{\pi}{2}}$$

$$\times \left(\frac{i}{4\pi\omega\varepsilon_a b} \frac{\partial(b j_n(kb))}{\partial b} + \frac{120\pi}{4\pi} j_n(kb) \right) P_n^1(\cos\vartheta)\cos\varphi,$$

where

$$I_n = -\frac{2\pi}{n(n+1)} \int_0^{\vartheta_0} ((1-\cos\vartheta) P_n^1(\cos\vartheta)$$

$$- n(n+1) P_n^0(\cos\vartheta)) f(\vartheta) d\vartheta.$$

The currents on the surface are given by the relations

$$j_\vartheta^e = j_0 \frac{1}{r^2} f(\vartheta)\cos\varphi\delta(r-b),$$

$$j_\varphi^e = -j_0 \frac{1}{r^2} f(\vartheta)\sin\varphi\delta(r-b),$$

where $f(\vartheta)$ is the amplitude-phase distribution of currents on the surface. Excluding I_n from the above formula for the field, we obtain an expression for the radial field component of the Huygens source field. The radial field component for any other feed is described by the same formula with the corresponding I_n.

The transverse field component for a feed spaced a distance b from the origin and possessing the radiation pattern $F(\vartheta)$ is given by the relation

$$E_\vartheta = C \frac{e^{-ikr}}{r} \frac{F(\theta)}{(1-\cos\vartheta)} (1-\cos\vartheta) e^{ikb\cos\vartheta} \cos\varphi$$

and the longitudinal (axial) component is

$$E_r = C \frac{e^{-ikr}}{r^2} \frac{F(\vartheta)}{(1-\cos\vartheta)}$$

$$\times \sin\vartheta \sqrt{1 + \left(\frac{kb}{2}(1-\cos\vartheta)\right)^2} e^{ikb\cos\vartheta} \cos\varphi.$$

Expanding E_r into series in spherical harmonics [7],

$$E_r = C \frac{e^{-ikr}}{r^2} \sum_{n=1}^{\infty} \frac{2n+1}{n(n+1)} \int_0^{\pi} e^{ikb\cos\vartheta} \frac{F(\vartheta)}{(1-\cos\vartheta)} \sin^2\vartheta$$

$$\times \sqrt{1 + \left(\frac{kb}{2}(1-\cos\vartheta)\right)^2} P_n^1(\cos\vartheta) d\vartheta \cos\varphi$$

and equating the formula for E_r of the emitting surface to E_r of an arbitrary feed, we obtain the desired expression for I_n:

$$I_n = \frac{C \int_0^{\pi} e^{ikb\cos\vartheta} \frac{F(\vartheta)}{(1-\cos\vartheta)} \sin^2\vartheta \sqrt{1 + \left(\frac{kb}{2}(1-\cos\vartheta)\right)^2} P_n^1(\cos\vartheta) d\vartheta}{n(n+1) j_0 \left(\frac{i}{4\pi\omega\varepsilon_a b} \frac{\partial(b j_n(kb))}{\partial b} + \frac{120\pi}{4\pi} j_n(kb) \right)}.$$

Now it is necessary to satisfy the boundary conditions for all spherical harmonics and express the transverse field components via the longitudinal ones. The transverse electric field component E_ϑ of a multilayer spherical lens-antenna composed of homogeneous dielectric layers is given by the expression

$$E_\vartheta = \frac{j_0 k}{8\pi} \frac{e^{-ikr}}{r} \Bigg[\frac{1}{\omega\varepsilon_a b} \Bigg(\sum_{n=1}^{\infty} C_n^{ee} \{ P_n^2(\cos\vartheta)$$

$$- n(m+1) P_n^0(\cos\vartheta) + 2kb \frac{i}{\sin\vartheta} \sum_{n=1}^{\infty} C_n^{me} P_n^1(\cos\vartheta) \Bigg)$$

$$-120\pi i\left(\sum_{n=1}^{\infty} C_n^{mm}\{P_n^2(\cos\vartheta) - n(n+1)P_n^0(\cos\vartheta)\}\right.$$
$$\left. - \frac{2i}{kb\sin\vartheta}\sum_{n=1}^{\infty} C_n^{em} P_n^1(\cos\vartheta)\right)\Bigg]\cos\varphi,$$

where

$$C_n^{ee} = \frac{2n+1}{n(n+1)}\left(\frac{\partial(bj_n(kb))}{\partial b} + \frac{\partial(bh_n^{(2)}(kb))}{\partial b}a_n^e\right)e^{in\frac{\pi}{2}}I_n,$$

and a_n^e are coefficients determined from the boundary conditions. Expressions for the other C_n values are written similarly.

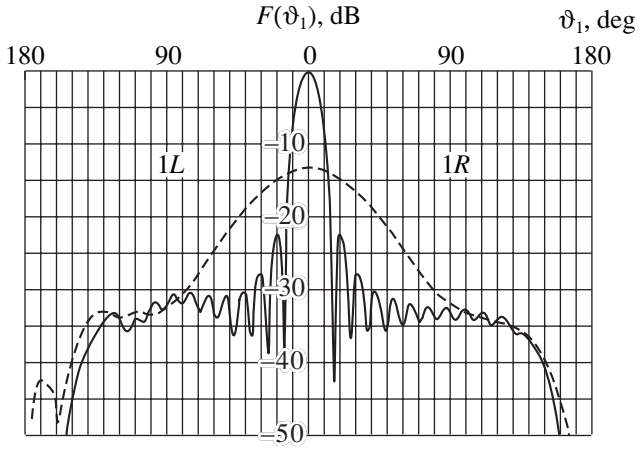

Fig. 1. Comparison of the radiation patterns of the Luneberg lens calculated for (1*R*) a feed in the form of an in-phase emitting surface and (1*L*) according to the proposed method. Dashed curves show the corresponding feed radiation patterns.

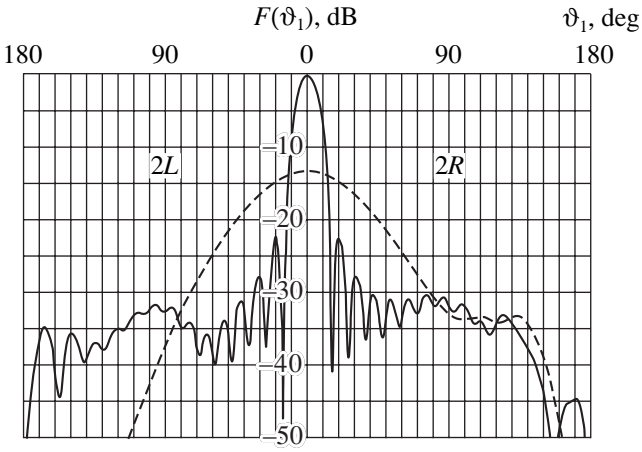

Fig. 2. Comparison of the radiation patterns of the Luneberg lens calculated for the given feed radiation patterns (2*R*) according to the proposed method (reproduced from Fig. 1*L*) and (2*L*) using an approximated radiation pattern of a real feed.

Application of the proposed method is illustrated in Figs. 1 and 2 by comparing the radiation patterns of the antenna and feed (normalized to the antenna field $E_\vartheta(\varphi = 0)$). In these figures, $\vartheta_1 = 180 - \vartheta$; $D/\lambda = 5$ is the lend diameter; $b = 1.1D/2$ is the distance to the feed; $N = 14$ is the number of layers in the lens; and $\varepsilon_{14} = 1.1$ is the permittivity of the outer layer of the lens.

In Fig. 1, the right-hand part (1*R*) shows the radiation pattern of the antenna with a feed in the form of a cophase radiating surface with the amplitude distribution decaying to the edge ($R = 0.6\lambda$ is the emitting surface radius). The left-hand part (1*L*) is the radiation pattern of the antenna with a feed whose radiation pattern is obtained by approximating that of the emitting surface with a polynomial of the fifth power (this polynomial is substituted in the expression for I_n).

In Fig. 2, the right-hand part (2*R*) reproduces the left-hand radiation pattern from Fig. 1 (1*L*). The left-hand part (2*L*) is the radiation pattern of the antenna with a feed whose radiation pattern coincides with that of the of the emitting surface in the region of angles at which the lens is viewed from the feed. In this region, the radiation pattern of the emitter is approximated by the function $\exp(-0.00067x^{1.85})$ (this function is substituted in the expression for I_n). The sidelobe level of the feed radiation pattern at the lens edge ($\vartheta_1 = 65°$) is –12 dB and the back radiation level is small (as in real feeds). Thus, allowance for the feed radiation pattern of a real feed most adequately reflects the pattern of phenomena taking place in the lens.

REFERENCES

1. R. J. Sanford, IEEE Antennas Propag. Mag. **37**, 76 (1995).
2. D. V. Shannikov and S. V. Kuzmin, in *Proceedings of the 1st IEEE International Conference on Circuits and Systems for Communications (ICCSC), St. Petersburg, 2002*.
3. D. M. Sazonov and N. Ya. Frolov, Zh. Tekh. Fiz. **35**, 763 (1965) [Sov. Phys. Tech. Phys. **10**, 990 (1965)].
4. J. R. Sanford, IEEE Antennas Propag. Mag. **42**, 690 (1994).
5. A. B. Vedenski, E. B. Zakharov, A. I. Skorodumov, and Yu. Ya. Kharlanov, Radiotekh. Élektron. (Moscow) **36** (4) (1991).
6. G. T. Markov and A. F. Chaplin, *Excitation of Electromagnetic Waves* (Radio i Svyaz', Moscow, 1983).
7. J. A. Stratton, *Electromagnetic Theory* (McGraw-Hill, New York, 1941; Gostekhizdat, Moscow, 1948).

Translated by P. Pozdeev

Technical Physics Letters, Vol. 29, No. 11, 2003, pp. 944–946. Translated from Pis'ma v Zhurnal Tekhnicheskoĭ Fiziki, Vol. 29, No. 22, 2003, pp. 46–52.

The Electron Beam with Virtual Cathode in a Two-Section Drift Tube

A. A. Grishkov, S. Ya. Belomyttsev, S. D. Korovin, and V. V. Ryzhov*

Institute of High-Current Electronics, Siberian Division, Russian Academy of Sciences, Tomsk, Russia

** e-mail: ryzhov@to.hcei.tsc.ru*

Received May 26, 2003

Abstract—An analysis based on the law of conservation of the *z* component of field and particle momentum in a thin annular magnetized monoenergetic electron beam in a two-section drift tube composed of tube segments with different radii ($R_1 < R_2$) allowed the critical injected beam current to be determined for which a virtual cathode, formed in the wider tube at the joint section, starts traveling through the narrower tube toward the beam injection region. A region behind the traveling virtual cathode features a "squeezed" single-flux state of the beam (corresponding to the "slow" left branch of the current characteristic, high charge density, but low relativistic factor). When the injected current decreases below a critical transition level ($I_{in} < I_{Tr}$), the virtual cathode returns to the initial position and restores the double-flux electron beam. This current is smaller than $(I_{lim1} + I_{lim2})/2$, and, depending on R_2, varies from the limiting transport current for the narrower section (I_{lim1}) up to $I_F/2$, where I_F is the Fedosov current for this tube section. © *2003 MAIK "Nauka/Interperiodica".*

Consider a drift tube composed of two long tube segments with different radii (Fig. 1, $R_1 < R_2$, $R_1 \ll |z_1 - z_{12}|$, $R_2 \ll |z_2 - z_{12}|$) and let a thin annular monoenergetic electron beam be injected from the left into the section of smaller radius R_1. The tube occurs at a potential of the anode and is exposed to a strong magnetic field with the strength vector **H** parallel to the system axis. The magnetic field strength is so large that the Larmor radius of electron is much smaller than the beam diameter.

When such a beam, transported via the two-section tube, is characterized by an injected beam current I_{in} exceeding the limiting transport current for the tube of greater radius (I_{lim2}), a virtual cathode (VC) is formed in this tube at a distance on the order of $R_1 - R_b$ from the joint cross section ($z = z_{12}$). The VC reflects a part (I_{back}) of the injected current, so that the transmitted (output) current is given by the relation $I_{out} = I_{in} - I_{back}$. The possible values of these currents for the stationary states with VC in an infinite homogeneous (smooth) tube ($R_1 = R_2$) were determined previously [1]. The calculations showed that, when the injected beam current exceeds a certain critical transition value ($I_{in} \geq I_{Tr}$), the VC (i.e., the plane of $\varphi_{VC} = 0$) shifts toward the beam injection region ($z = 0$, left end of the narrow tube) leaving the beam in a "squeezed" state behind (on the right). According to [2], the critical current value is close to $(I_{lim1} + I_{lim2})/2$, but the exact value of I_{Tr} is not yet determined.

A solution to this problem can be found based on the notion that, when the injected beam current increases after VC formation, the flux *F* of the *z* component of the field and particle momentum through the joint cross section between the two drift tubes cannot exceed a certain value F_{max} at which the electron beam in the narrow tube occurs in the "squeezed" state.

Select a volume (with the boundary depicted by dashed line in Fig. 1) such that the field and beam parameters on the left and right boundaries can be considered independent of the coordinate *z*. The momentum flux *F* through the joint cross section of the two drift tubes for the stationary states of the two-section system can be found from the law of conservation of the field and particle momentum. This flux is determined as

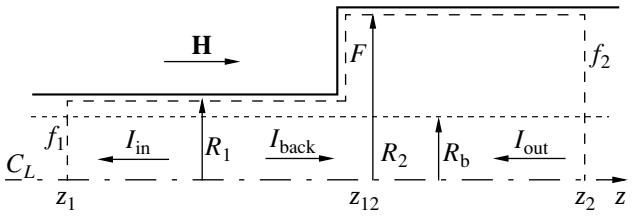

Fig. 1. The geometry of a two-section drift tube transporting a thin annular electron beam: (R_1, R_2) the tube radii; (R_b) the beam radius; (I_{out}, I_{in}, I_{back}) the output (transmitted) current, the injected current, and the current of electrons reflected from the VC; (f_1, f_2, *F*) the fluxes of *z*-component of the field and particle momentum in the corresponding cross sections of the calculation region indicated by the dashed contour.

1063-7850/03/2911-0944$24.00 © 2003 MAIK "Nauka/Interperiodica"

a difference between the corresponding fluxes $f_i(\gamma_i, \beta_i)$ through the end sections [1, 2]:

$$F = f_1(\gamma_2, \beta_2) - f_2(\gamma_1, \beta_1), \quad (1)$$

$$f_i(\gamma_i, \beta_i) = \frac{(\Gamma - \gamma_i)^2}{\ln(\beta_i)} + \frac{2(\Gamma - \gamma_i)(\gamma_i^2 - 1)}{\gamma_i \ln(\beta_i)}, \quad (2)$$

where $\Gamma = 1 + eU/mc^2$, U is the electrostatic (anode) potential of the drift tube, γ_i is the relativistic beam factor in the corresponding section of the tube, and $\beta_i = R_i/R_b$.

In the two-section system for the annular electron beam transport with VC, the output current is equal to the limiting transport current in the tube of greater radius $I_{out} = I_{lim2}$ [2]. Therefore, the flux F in the beam transport regime without VC formation can be found by varying the output current from zero to the limiting transport current in the tube of greater radius and taking into account that γ_1 and γ_2 must belong to the right-hand branch of the current characteristic [1]. The values of γ_1 are determined using the well-known relation

$$I = \frac{I_0}{2\ln\beta} \frac{(\Gamma - \gamma)^2 \sqrt{\gamma^2 - 1}}{\gamma}, \quad (3)$$

where $I_0 = mc^3/e \approx 17$ kA, m is the electron mass, e is the electron charge, and c is the speed of light in vacuum. The values of γ_2 are obtained from the same relation with $\beta = \beta_2$.

In the case of the electron beam transport with VC, the output current is $I_{out} = I_{lim2}$ = const and the tube section of smaller radius features two electron fluxes. The charge density in this tube is proportional to the sum of injected and reflected currents:

$$I_{eff} = I_{in} + I_{back} = (2I_{in} - I_{out}) \le I_{lim1}. \quad (4)$$

Apparently, the current can increase until $I_{in} + I_{back} \le I_{lim1}$ and the maximum injected current must obey the condition

$$I_{in}^{max} \le (I_{lim1} + I_{lim2})/2. \quad (5)$$

In calculating the momentum flux F, we should take into account that the relativistic beam factor in the wider section is constant ($\gamma_2 = \Gamma^{1/3}$), while the relativistic factor in the section of smaller radius γ_1 is determined from relation (3) with $I = I_{eff}$ varying from I_{lim2} to I_{in}^{max}.

Figure 2 shows the plot of F versus injected beam current (curve *ABCD*). As the current grows up to I_{lim2} (point *B*), the flux through the joint cross section slowly increases. Upon the VC formation, the output current reaches maximum and ceases to change. Therefore, the flux through the plane $z = z_2$ also remains constant. Thus, an increase in the flux of the z component of momentum on the left side (related to an increase in the injected current) in the system with VC is compensated only at the expense of increasing flux through the joint cross section. This leads to a sharp increase in the slope of the function F (segment *BD*). As can be seen from Fig. 2, the flux calculated as described above reaches maximum for $I_{in}^{max} = (I_{lim1} + I_{lim2})/2$ (point *D*).

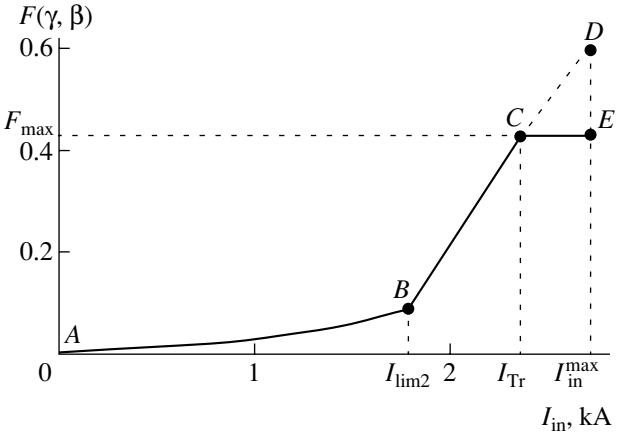

Fig. 2. A plot of the z-component of the field and particle momentum $F(\gamma, \beta)$ in the joint cross section of a two-step drift tube versus injected current I_{in} (for $\Gamma = 2$, $R_b = 0.35$ cm, $R_2 = 3$ cm): (*BC*) the VC occurs near the joint cross section; (*CE*) the VC occurs at the left end of the narrower tube, near the beam injection region.

However, the above calculation did not take into account that, at a certain value of the injected current, the VC shifts toward the beam injection region and a beam in the "squeezed" state is formed behind the VC (on the right) with a high charge density and a low relativistic factor γ_1. In this state, the flux through the joint cross section exhibits no increase because the beam in the narrow section is in the "squeezed" state and its electrostatic potential has a certain value independent of the injected current. Thus, the flux F corresponding to the "compressed" state formation over the entire narrow section is the maximum flux above which the VC begins to shift.

Let us determine the flux $F = F_m$ corresponding to this state. By solving Eq. (3) for the relativistic factor in the first tube at $I = I_{out} = I_{lim2}$ and taking into account that γ_1 must belong to the left branch of the current characteristic ($1 \le \gamma_1 \le \Gamma^{1/3}$) [1], we determine this relativistic factor and then calculate the corresponding F_m (Fig. 2, segment *CE*) using formulas (1) and (2).

The point of intersection of the curves $F = F(I_{in})$ and $F = F_m$ (point *C*) corresponds to the critical transition current I_{Tr} at which the VC begins to shift toward the beam injection region leaving a "compressed" beam behind. In the case when the VC occurs at the left end of the narrower tube, further increase in the injected current will no longer influence the flux F, which is

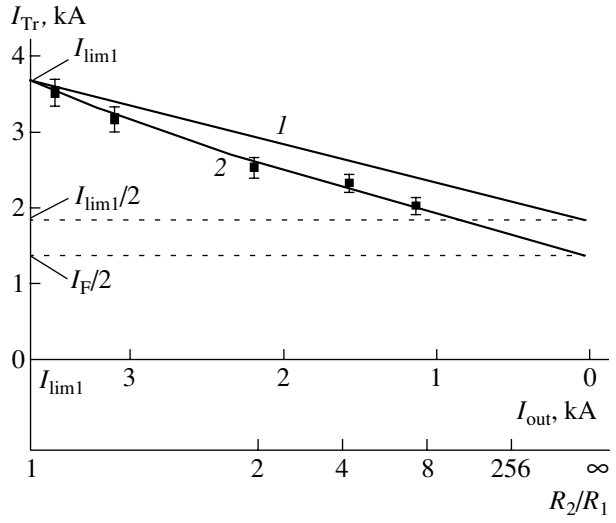

Fig. 3. Plots of the VC transition current I_{Tr} versus output current I_{out} or the R_2/R_1 ratio (for $\Gamma = 2$, $R_1 = 1$ cm, $R_b = 0.35$ cm): (*1*) $(I_{lim1} + I_{lim2})/2$; (*2*) theoretical calculation; black points show the results of calculations using PIC code KARAT.

determined by the "squeezed" state of the beam and retains a constant value of $F = F_m$ (Fig. 2, segment *CE*).

For a given anode voltage, the critical current is determined by the transport channel geometry. Figure 3 shows the dependence of the VC transition current I_{Tr} on the output current I_{out}, determined by the greater tube radius R_2. An analysis showed that the values of these currents coincide with those determined for the stationary states of a thin annular beam with VC in a homogeneous tube at an output current equal to I_{out} [1]. As $I_{out} \longrightarrow 0$ ($R_2 \longrightarrow \infty$), the VC transition current tends to half of the Fedosov current ($I_F/2$); for $R_2 \longrightarrow R_1$, this transition current tends to the limiting transport current for the first tube ($I_{Tr} \longrightarrow I_{lim\,1}$). Note that, as the injected beam current decreases below the critical level ($I_{in} < I_{Tr}$), the VC returns to the initial state at the joint cross section (Fig. 2) and the two-flux electron beam state in the narrow tube is restored.

In order to verify the above theoretical results, we have simulated the transport of a thin annular electron beam in a two-section drift tube by means of the electromagnetic PIC code KARAT [4]. In all calculations, the smaller tube radius and the beam radius remained fixed ($R_1 = 1$ cm; $R_b = 0.35$ cm), while the greater tube radius was varied from 2 to 10 cm. The results of these simulations confirmed that the VC is formed near the joint cross section ($z = z_{12}$) when the injected current reaches the limiting transport current for the second tube ($I_{in} = I_{lim\,2}$) [2, 3]. The critical transition current I_{Tr} obtained in this simulation (indicated by points in Fig. 3) is always below $I_{in}^{max} = (I_{lim1} + I_{lim\,2})/2$ (Fig. 3, plot *1*) and agrees well with the values obtained in the analytical calculation (Fig. 3, plot *2*). For $R_1 = R_2$, these values coincide with the limiting current for the narrower tube $I_{Tr} = I_{in}^{max} = I_{lim1}$.

These results allow us to predict the behavior of a thin annular magnetized monoenergetic electron beam with VC transported in a two-section tube channel, depending on the injected beam current I_{in}. For the injected currents $I_{lim\,2} \le I_{in} < I_{Tr}$, the VC occurs near the joint cross section. When the injected current reaches the critical value $I_{in} = I_{Tr}$, the VC begins to shift through the tube of smaller radius toward the beam injection region. In this state, I_{in} and I_{back} are equal to the corresponding currents in the stationary state of the beam with VC transported in a homogeneous drift tube with $R = R_1$ for the output current equal to the limiting transport current in the second tube $I_{lim\,2}$. This is related to the fact that the system geometry to the left of VC is close to the geometry of an infinite homogeneous tube considered previously [1], while the tube with $R = R_2$ only determines the output current.

For $I_{in} > I_{Tr}$, the VC occurs at the entrance to the narrower tube, close to the beam injection region. Irrespective of I_{in}, the output current I_{out} is constant, while the beam to the right of the VC occurs in a "squeezed" single-flux state which, according to [1], is a characteristic feature of the stationary state of a beam with VC in a homogeneous drift tube.

REFERENCES

1. S. Ya. Belomyttsev, A. A. Grishkov, S. D. Korovin, and V. V. Ryzhov, Pis'ma Zh. Tekh. Fiz. **29** (16), 16 (2003) [Tech. Phys. Lett. **29**, 666 (2003)].
2. A. M. Ignatov and V. P. Tarakanov, Phys. Plasmas **1**, 741 (1994).
3. A. E. Dubinov and I. E. Efimova, Zh. Tekh. Fiz. **71** (6), 80 (2001) [Tech. Phys. **46**, 723 (2001)].
4. V. P. Tarakanov, *User's Manual for Code Karat* (Berkley, Springfield, 1992).

Translated by P. Pozdeev

Technical Physics Letters, Vol. 29, No. 11, 2003, pp. 947–948. Translated from Pis'ma v Zhurnal Tekhnicheskoĭ Fiziki, Vol. 29, No. 22, 2003, pp. 53–57.

One-Dimensional Diffuser Based on a Thick Layer of Dichromated Gelatin

N. M. Ganzherli*, Yu. N. Denisyuk, and I. A. Maurer

Ioffe Physicotechnical Institute, Russian Academy of Sciences, St. Petersburg, 194021 Russia

** e-mail: nina@holo.ioffe.rssi.ru*

Received June 11, 2003

Abstract—A new diffuser capable of scattering light in one direction (one-dimensional diffuser) has been developed and experimentally tested. The diffuser is formed in a thick layer of dichromated gelatin. The scattering indicatrices of the diffuser measured in two mutually perpendicular directions are presented. It is demonstrated that the indicatrix width in one direction is significantly greater than that in the perpendicular direction. However, no zero-order diffraction has been observed. The proposed one-dimensional diffuser exhibits close scattering indicatrices for reading at a wavelength of 0.44 and 0.63 μm. *© 2003 MAIK "Nauka/Interperiodica".*

In solving some applied problems, in particular those encountered in recording and reconstructing the so-called pseudodeep holograms [1–3] and selectograms [4, 5] and projecting three-dimensional (3D) images by 3D-scene aspect method [6, 7], we have used a 1D diffuser. One of the main requirements to this device is the absence of light transmitted in the zeroth order of diffraction. Previously, 1D diffusers were obtained either by making a system of unidirectional grooves on a glass plate or by recording a pattern of special type speckles on photographic plates. However, these methods do not always ensure suppression of the zero-order diffraction in the transmitted light, and do not fully meet the requirements with respect to homogeneity of scattering over the entire diffuser area.

Brui and Orlov [8] proposed a method of preparation and studied the scattering characteristics of a 1D diffuser recorded on a standard holographic plate (PFG-03S type) and fixed by a special photochemical treatment. The diffuser was used for reconstructing images by the aspect method, under conditions when only a horizontal parallax was reproduced.

Below we report on a method of recording and present the results of the studying scattering properties of a 1D diffuser obtained in a thick layer of glycerin-containing dichromated gelatin [9, 10]. The gelatin layer thickness was varied from 80 to 150 μm. Glycerin was added in order to maintain water content in the layer on a certain level [11]. Owing to the presence of water, a latent image is immediately developed in the course of recording. Thus, the material works in real time and allows the pattern to be monitored in the course of recording. Data recording has a purely phase character.

A 1D diffuser is recorded in a dichromated gelatin layer using a pattern of speckles created by light scattered from a normal diffuser illuminated by a narrow light beam formed by a cylindrical lens. The beam was additionally filtered by a slit diaphragm situated in the diffuser plane. The speckle pattern was recorded using the light of a He–Cd laser operating at a wavelength of 0.44 μm (within the dichromated gelatin sensitivity region).

For measuring the scattering indicatrix, the 1D diffuser was probed with a collimated laser beam. Radiation scattered from the 1D diffuser was focused by a lens on the exit window of a photodetector situated in the focal plane. The photodetector was moved along a circle centered at the lens. Figures 1 and 2 show the scattering indicatrices of one of a series of diffusers, measured in the horizontal and vertical planes. The measurements were performed using the radiation of He–Cd and He–Ne lasers (as indicated in Figs. 1 and 2).

Let us consider the results in some detail. According to Figs. 1 and 2, the indicatrices of volume speckle pat-

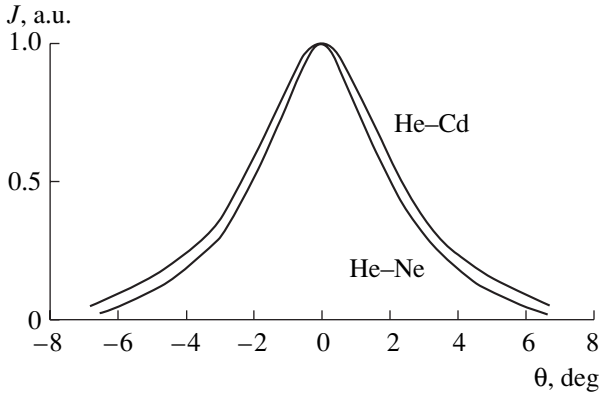

Fig. 1. Scattering indicatrices of a 1D diffuser in the horizontal plane measured using He–Cd and He–Ne lasers.

1063-7850/03/2911-0947$24.00 © 2003 MAIK "Nauka/Interperiodica"

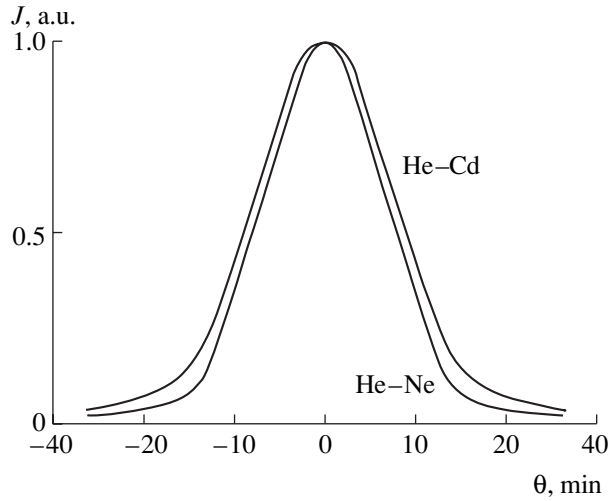

Fig. 2. Scattering indicatrices of a 1D diffuser in the vertical plane measured using He–Cd and He–Ne lasers.

terns recorded in a thick (~100 μm) layer differ from the analogous curves observed for thin (~7 μm) layers [8] in that the former exhibit virtually no zero-order diffraction (i.e., no intense peaks in the region of zero frequency). This makes the former 1D diffuser more suitable for use as directional screens for projecting 2D images.

The width of the indicatrix (defined as the full width at half maximum, FWHM) in the horizontal plane is several dozen times greater than that in the perpendicular direction. The light line has dimensions 10 and 0.5 mm and is situated 240 mm from the dichromated gelatin layer. The angular dimensions in the horizontal and vertical directions for the line viewed from the center of the recording medium amount to 2.5° and 6.8′, respectively. The angular dimensions reproduced by the 1D diffuser, determined as the scattering indicatrix FWHM in the horizontal and vertical directions, are 4° and 15′, respectively. Thus, there is an almost twofold magnification of the angular size.

The fact that the shape of the scattering indicatrix of the volume speckle patterns is weakly dependent on the reading wavelength allows the use of such diffusers for projecting color images. The 1D diffusers possessing a scattering indicatrix with FWHM ~ 4° in the horizontal plane can be considered unidirectional. This property can be useful, for example, in solving problems with recording data on media of the thick dichromated gelatin type characterized by low sensitivity and the diffraction efficiency decreasing with an increase in spatial frequency [10]. In particular, such 1D diffusers can be useful for recording unsupported selectograms. The method proposed for recording a 1D diffuser in a thick layer of dichromated gelatin can also be successfully used for recording 2D directional diffusers.

Acknowledgments. This study was supported by the Russian Foundation for Basic Research (project no. 01-02-17854) and the Program for Support of Scientific Schools (project no. NSh-98.2003.2).

REFERENCES

1. Yu. N. Denisyuk and N. M. Ganzherli, Zh. Tekh. Fiz. **63** (2), 81 (1993) [Tech. Phys. **38**, 98 (1993)].
2. N. M. Ganzherli and Yu. N. Denisyuk, Opt. Mem. Neural Netw. **1** (1), 1 (1992).
3. Yu. N. Denisyuk and N. M. Ganzherli, Opt. Eng. **31**, 731 (1992).
4. N. M. Ganzherli and Yu. N. Denisyuk, Opt. Spektrosk. **79**, 670 (1995) [Opt. Spectrosc. **79**, 618 (1995)].
5. Yu. N. Denisyuk and N. M. Ganzherli, Opt. Eng. **33**, 3307 (1994).
6. Yu. N. Denisyuk, V. B. Markov, and N. M. Ganzherli, Opt. Spektrosk. **84**, 104 (1998) [Opt. Spectrosc. **84**, 94 (1998)].
7. Yu. N. Denisyuk, N. M. Ganzherli, V. V. Orlov, *et al.*, Opt. Spektrosk. **86**, 864 (1999) [Opt. Spectrosc. **86**, 775 (1999)].
8. E. B. Brui and V. V. Orlov, Pis'ma Zh. Tekh. Fiz. **24** (5), 70 (1998) [Tech. Phys. Lett. **24**, 197 (1998)].
9. Yu. N. Denisyuk, N. M. Ganzherli, I. A. Maurer, and S. A. Pisarevskaya, Pis'ma Zh. Tekh. Fiz. **23** (4), 62 (1997) [Tech. Phys. Lett. **23**, 279 (1997)].
10. Yu. N. Denisyuk, N. M. Ganzherli, I. A. Maurer, and S. A. Pisarevskaya, Pis'ma Zh. Tekh. Fiz. **25** (5), 64 (1999) [Tech. Phys. Lett. **25**, 194 (1999)].
11. V. P. Sherstyuk, A. H. Malov, S. M. Maloletov, and V. V. Kalinkin, Proc. SPIE **1238**, 218 (1989).

Translated by P. Pozdeev

Technical Physics Letters, Vol. 29, No. 11, 2003, pp. 949–950. Translated from Pis'ma v Zhurnal Tekhnicheskoĭ Fiziki, Vol. 29, No. 22, 2003, pp. 58–62.

Wavy Surface Nanostructures Formed in Amorphous Silicon Films by Sputtering with Nitrogen Ions

I. V. Zhuravlev, D. S. Kibalov, G. F. Smirnova, and V. K. Smirnov

Institute of Microelectronics and Informatics, Russian Academy of Sciences, Yaroslavl, Russia

e-mail: IBTec@rambler.ru

Received May 30, 2003

Abstract—Wavy nanostructures are formed on the ion-bombarded surface of single-crystal and amorphous silicon films prepared by various methods. The period and depth of this structure have been determined as functions of the angle of incidence and the energy of nitrogen ions used for the surface sputtering. A comparative analysis of SEM images of the wavy surface nanostructures on various silicon films has been performed using a two-dimensional Fourier transform. The films of amorphous silicon obtained by electron beam deposition and magnetron sputtering techniques are closest to single-crystal silicon films with respect to the wavy surface nanostructure formation. *© 2003 MAIK "Nauka/Interperiodica".*

As is known, ion bombardment of the surface of various materials at oblique angles leads to spontaneous formation of a wavy surface relief (wavy nanostructure) on the target surface, in which the waves are oriented perpendicularly to the ion bombardment direction. Originally, such a wavy relief on the solid surface was observed for glass targets bombarded with ionized air molecules, the ion beam being composed predominantly of nitrogen ions [1]. Among various ion–semiconductor couples, the N_2^+–Si system is distinguished by a planar character, minimum spatial period (wavelength) λ (~20 nm), small depths of formation (D_F), and constancy of both wavelength and amplitude of the wavy structure formed upon ion sputtering to a depth exceeding D_F [2]. Further investigation of the wavy surface nanostructures formed on the surface of amorphous silicon (a-Si) in comparison to those on single crystal silicon (c-Si) is of interest, because replacing crystalline silicon with amorphous silicon may lead to a considerable expansion of the application field of such films with nanostructures.

We have studied the films of amorphous silicon prepared by various standard techniques [3], including magnetron sputtering of a silicon target (these samples denoted by a-Si_M), electron beam deposition (a-Si_E), chemical vapor deposition at low pressures (a-Si_V), and low-frequency discharge in silane (a-Si:H). The a-Si film thicknesses (D) and the temperatures of substrates (made of thermally oxidized c-Si) are indicated in the table. For a-Si_M and a-Si:H films, the parameters of deposition can be found elsewhere [4, 5]. The wavy nanostructures on the surface of samples were formed and studied in a high-vacuum setup equipped with an ion gun of the duoplasmatron type.

The process of the surface nanostructure formation is characterized by two sputtering depths: D_m, corresponding to the appearance of a small-amplitude relief with a wave sloping angle about 5° relative to the initial surface plane; and D_F, corresponding to the formation of a stable relief with a saturated value of the amplitude and a wave sloping angle of about 30°. In our experiments, the sample surface morphology before and after ion bombardment was studied using a scanning electron microscope (SEM). By means of two-dimensional Fourier transform of SEM images of the wavy surface nanostructures, it is possible to determine the most probable values of the wavelength λ and the corresponding distribution width $\Delta\lambda$ (defined as full width at half maximum, FWHM).

The parameters of amorphous silicon films and wavy surface nanostructures

	D, nm	T, °C	D_m, nm	D_F, nm	λ, nm	$\Delta\lambda$, nm	$\lambda/\Delta\lambda$
c-Si			125	205	122	87	1.40
a-Si_E	480	35	120	160	131	90	1.46
a-Si_M	270	120	130	185	128	80	1.59
a-Si_V	400	560	110	160	131	110	1.19
a-Si:H	380	220	40	110	152	175	0.87

1063-7850/03/2911-0949$24.00 © 2003 MAIK "Nauka/Interperiodica"

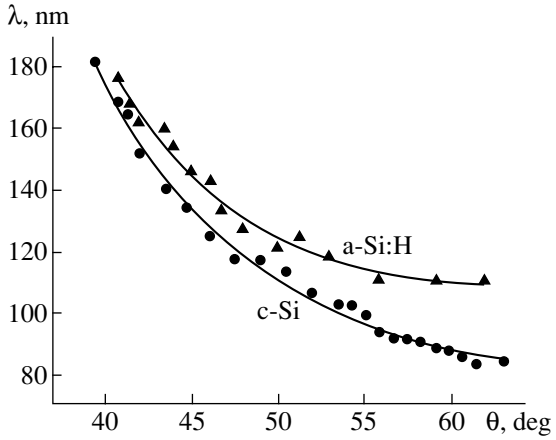

Fig. 1. Plots of the nanostructure period λ versus ion beam incidence angle for c-Si and a-Si:H samples bombarded with 8-keV nitrogen ions.

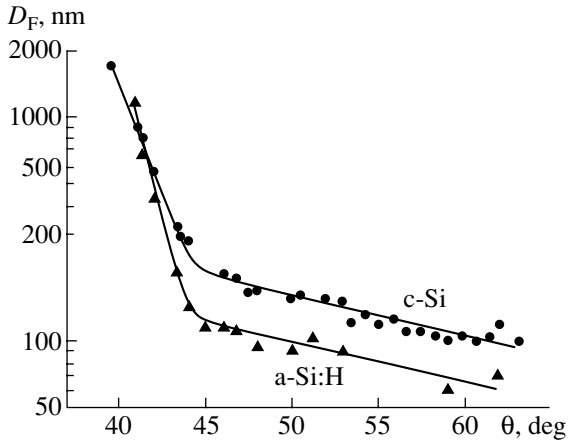

Fig. 2. Plots of the nanostructure formation depth D_F versus ion beam incidence angle for c-Si and a-Si:H samples bombarded with 8-keV nitrogen ions.

The results of determination of the D_m, D_F, λ, and Δλ values are summarized in the table. These data refer to the surface nanostructures formed by sputtering with N_2^+ ions at an ion beam energy of $E = 8$ keV and an incidence angle of θ = 45° relative to the sample surface normal. The λ and Δλ values were determined for the structures formed upon sputtering to a depth of D_F. The λ/Δλ ratio exhibits correlation with the degree of order of the surface nanostructures observed in SEM images. As can be seen from data in the table, amorphous silicon films of the a-Si_E and a-Si_M types are closest to single crystal layers c-Si with respect to the wavy surface nanostructure formation, while a-Si:H films are characterized by accelerated formation of the nanostructure and most significantly differ from c-Si layers in this respect.

The dynamics of the surface nanostructure formation depends on the initial topography of the material surface (before the onset of sputtering) [6], this dependence being reflected by the D_m and D_F values for a-Si films. An analysis of SEM images of the initial surface revealed the following features in the sample morphology. The surface of a-Si_M contained separate inhomogeneities with a diameter of about 100 nm, spaced by more than 10 μm. The surface of a-Si_E exhibited topographic inhomogeneities with an average size of 20–30 nm. SEM images of the cleaved samples showed the height of these inhomogeneities to be about 2–3 nm. Close topography was observed for a-Si_V. In the case of a-Si:H, SEM images revealed large spherical inhomogeneities with diameters ranging within 10–200 nm and heights within 3–100 nm.

Figures 1 and 2 show the plots of λ and D_F versus the ion beam incidence angle θ for c-Si and a-Si:H films bombarded with 8-keV nitrogen ions, representing the two types of the samples most distinct from the standpoint of the wavy nanostructure formation. As can be seen, the two plots exhibit analogous behavior in both figures. For a-Si:H versus c-Si, the maximum excess in λ is 30%, while the maximum decrease in D_F reaches 50%. For ion beam energies in the interval $E = 3$–9 keV at an incidence angle of θ = 45°, the wavelength λ is a linear function of the energy: for a-Si:H, λ[nm] = 14.6E[keV] + 28.7; for c-Si, λ[nm] = 14.1E[keV] + 16.9.

In conclusion, the films of amorphous silicon obtained by magnetron sputtering or electron beam evaporation of silicon targets can develop wavy nanostructures under the action of ion bombardment, the quality of these structures being comparable with that of the analogous wavy relief formed on single crystal silicon. The presence of a certain roughness on the film surface accelerates the formation of surface nanostructures without decreasing their quality.

Acknowledgments. The authors are grateful to P.A. Lepshin for his help conducting experiments.

This study was performed within the framework of an agreement (contract no. 1-2002/7I) between the Institute of Microelectronics and Informatics and the Agency for Marketing of Scientific Products.

REFERENCES

1. M. Navez, C. Sella, and D. Chaperot, C. R. Acad. Sci., Paris **254**, 240 (1962).
2. V. K. Smirnov, D. S. Kibalov, S. A. Krivelevich, *et al.*, Nucl. Instrum. Methods Phys. Res. B **147**, 310 (1999).
3. *VLSI Technology*, Ed. by S. M. Sze (McGraw Hill, New York, 1983; Mir, Moscow, 1986).
4. V. F. Bochkarev, V. V. Naumov, O. S. Trushin, *et al.*, Tr. FTIAN **9**, 25 (1995).
5. B. G. Budaguan, A. A. Sherchenkov, D. A. Stryahilev, *et al.*, J. Electrochem. Soc. **145**, 2508 (1998).
6. V. K. Smirnov, D. S. Kibalov, P. A. Lepshin, *et al.*, Izv. Ross. Akad. Nauk, Ser. Fiz. **64**, 626 (2000).

Translated by P. Pozdeev

Technical Physics Letters, Vol. 29, No. 11, 2003, pp. 951–952. Translated from Pis'ma v Zhurnal Tekhnicheskoĭ Fiziki, Vol. 29, No. 22, 2003, pp. 63–67.

Wavy Nanorelief Transferred to the Surface of Various Materials

D. S. Kibalov, I. V. Zhuravlev, P. A. Lepshin, and V. K. Smirnov

Institute of Microelectronics and Informatics, Russian Academy of Sciences, Yaroslavl, Russia

e-mail: IBTec@rambler.ru

Received May 30, 2003

Abstract—A wavy nanorelief is formed on the ion-bombarded surface of amorphous silicon. The nanorelief can be transferred from these films to the surface of various materials (glass, polyimide, fianite, and GaAs) by means of ion sputtering. The transferred nanorelief geometry is retained to within a depth equal to the initial relief amplitude in amorphous silicon. In the course of subsequent sputtering, evolution of the nanorelief amplitude is determined by various processes accompanying ion bombardment, rather than by the sputtering alone as characterized by the sputtering yield. © *2003 MAIK "Nauka/Interperiodica".*

Sputtering of the surface of single crystal silicon (c-Si) bombarded with 1–10 keV ions leads to the formation of an anisotropic periodic microrelief on the target surface [1]. The structure morphology significantly depends on the ion beam type. In particular, a wavy nanorelief formed in the N_2^+–c-Si system is characterized by a small depth of formation (D_F), minimum spatial period (λ = 20 nm), and stability of the highly planar nanorelief formed upon sputtering to a depth exceeding D_F [2–4].

We have established that the character of variation of the D_F and λ values depending on the ion energy and incidence angle θ for the amorphous silicon (a-Si) targets bombarded with nitrogen ions is analogous to the behavior observed in c-Si. For θ = 45°–55° (relative to the normal to the target surface), the morphologies of the surface nanorelief formed on c-Si and a-Si are very close. This circumstance allows c-Si to be replaced by a-Si in applications involving the formation of a nanorelief as the element of a nanostructure. Since the layers of a-Si can be deposited onto various materials, it was of interest to study the possibility of transferring the nanorelief pattern from a silicon film to the substrate surface.

In our experiments, the films of a-Si with a thickness of 0.3 μm were deposited by magnetron sputtering of a silicon target onto various substrates including SiO_2 (0.5 μm)/Si, polyimide (0.6 μm)/glass, Y–Zr–O (fianite) crystal (0.16 μm)/Si, Corning glass, and GaAs [5]. According to the Auger electron spectroscopy data, the content of oxygen in the a-Si deposits did not exceed 0.7 at. %. The samples were bombarded with a beam of N_2^+ ions at E = 8 keV and θ = 45°. Under these conditions, a wavy nanorelief with λ = 128 nm is formed at D_F = 185 nm. Owing to the nanorelief stability, this morphology is retained during sputtering of the a-Si layer down to the substrate. Measurements of the relative sputtering yields Y for the above systems in the absence of wavy relief on the a-Si surface (E = 8 keV, θ = 38°) gave the following ratios: Y(fianite)/Y(a-Si) = 0.7; Y(glass)/Y(a-Si) = 1.1; $Y(SiO_2)$)/Y(a-Si) = 1.3; Y(polyimide)/Y(a-Si) = 1.6; Y(GaAs)/Y(a-Si) = 3.8.

The sample surface morphology in various stages of ion bombardment was studied using a scanning electron microscope (SEM). Figure 1 shows the typical nanorelief formed on the surface of polyimide and Fig. 2 shows the pattern observed on the glass surface after sputtering off the a-Si layer down to the interface.

All the materials studied, sputtered from the interface with a-Si down to a depth within the spatial wavelength amplitude (~30 nm), exhibited virtually exact transfer of the nanorelief morphology from a-Si to sub-

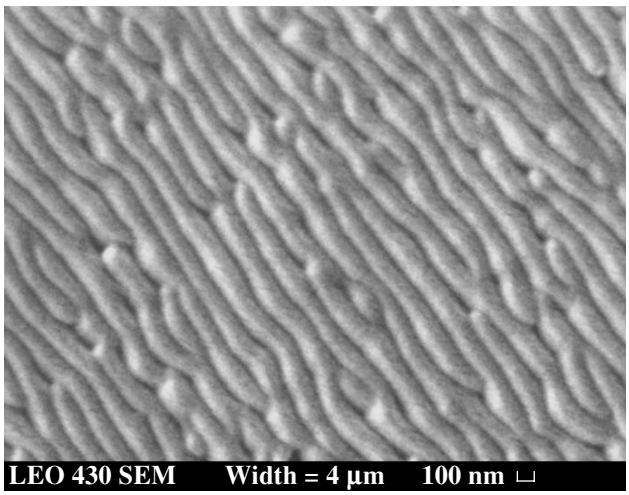

Fig. 1. A wavy nanorelief transferred to the surface of polyimide.

1063-7850/03/2911-0951$24.00 © 2003 MAIK "Nauka/Interperiodica"

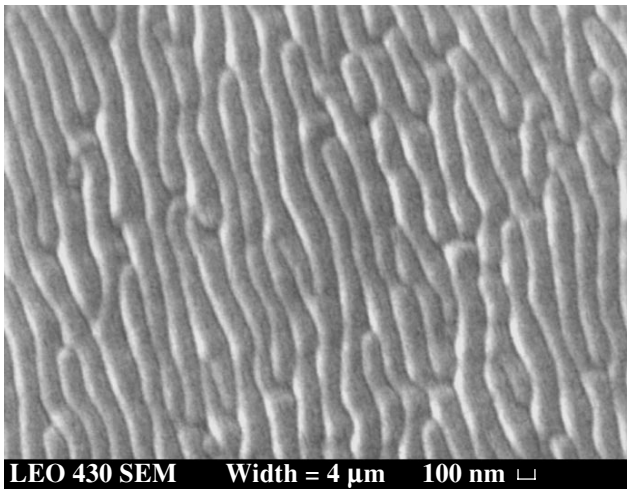

Fig. 2. A wavy nanorelief transferred to the surface of glass.

strate. Both the wavelength and geometry of the nanorelief are retained. Further sputtering gives rise to changes in the surface pattern morphology, the degree of which depends on the particular material. In fianite, the wave amplitude decreases without changing λ and is weakly pronounced upon sputtering down to the fianite/c-Si interface. Thus, the nanorelief exhibits smoothening in depth of the fianite layer, which is explained by a lower sputtering yield of this crystal compared to that of a-Si.

From the standpoint of the sputtering yield matching, a sufficiently optimistic situation can be expected in the a-Si/glass system. Indeed, SEM patterns showed the absence of any significant changes in the wavy nanorelief morphology even upon sputtering of the glass down do a depth of about 0.32 μm. Analogous behavior was observed during sputtering of a SiO_2 layer in the SiO_2/Si system, where changes in the nanorelief morphology appear and the λ value increases only at a depth of 0.30 μm.

A rather unexpected result was obtained in the case of polyimide. Despite an increase in the relative sputtering yield as compared to that for silicon oxide, the nanorelief morphology exhibits very weak evolution and becomes significant only upon sputtering polyimide down to a depth of 0.5–0.6 μm, without detectable changes in λ. Thus, polyimide has proved to be the most favorable material for the nanorelief transfer in the group of materials studied.

In contrast to the O_2^+–GaAs system [6], the sputtering of GaAs with N_2^+ ions at $E = 8$ keV and $\theta = 45°$ did not lead to wavy relief formation. During the nanorelief transfer from a-Si to GaAs, the surface wave amplitude exhibited a decrease without change in λ. In this system, the wavy nanorelief was retained during sputtering to a depth of about 1 μm. In contrast to expectations, intense sputtering did not accelerate evolution of the relief.

Thus, the possibility of obtaining a wavy nanorelief is no longer restricted to silicon. This morphology can be created on the surface of various materials by means of nanorelief transfer from an a-Si layer to a substrate during ion sputtering. The nanorelief is transferred without changes in shape upon sputtering down to a depth on the order of amplitude. Further evolution of the nanorelief amplitude is determined, besides pure sputtering effect, by some other factors accompanying ion bombardment (e.g., bombardment-enhanced surface diffusion).

Acknowledgments. The authors are grateful to G.F. Smirnova for her help in obtaining SEM images.

This study was performed within the framework of an agreement (contract nos. 1-2002/7I and 10-2003/7I) between the Institute of Microelectronics and Informatics and the Agency for Marketing of Scientific Products.

REFERENCES

1. G. Carter, V. Vishnyakov, and M. J. Nobes, Nucl. Instrum. Methods Phys. Res. B **115**, 440 (1996).
2. V. K. Smirnov, D. S. Kibalov, S. A. Krivelevich, *et al.*, Nucl. Instrum. Methods Phys. Res. B **147**, 310 (1999).
3. V. I. Bachurin, P. A. Lepshin, and V. K. Smirnov, Vacuum **56**, 241 (2000).
4. I. V. Zhuravlev, G. F. Smirnova, D. S. Kibalov, *et al.*, Poverkhnost, No. 10, 100 (2002).
5. V. F. Bochkarev, V. V. Naumov, O. S. Trushin, *et al.*, Tr. FTIAN **9**, 25 (1995).
6. A. Karen, Y. Nakagawa, M. Hatada, *et al.*, Surf. Interface Anal. **23**, 506 (1995).

Translated by P. Pozdeev

Technical Physics Letters, Vol. 29, No. 11, 2003, pp. 953–955. Translated from Pis'ma v Zhurnal Tekhnicheskoĭ Fiziki, Vol. 29, No. 22, 2003, pp. 68–73.

An Experimental Study of Millimeter Wave Absorption in Thin Metal Films

V. G. Andreev, V. A. Vdovin, and P. S. Voronov

Institute of Radio Engineering and Electronics, Russian Academy of Sciences, Moscow, Russia

e-mail: chusov@cplire.ru

Received June 2, 2003

Abstract—Optical characteristics (*R, T, A*) of thin aluminum films with thicknesses from 1.7 to 15 nm were studied at a wavelength of 8 mm with allowance for a substrate material. The absorption exhibits a maximum for a film thickness of 2.5 nm. The experimental data are interpreted taking into account the dependence of electric conductivity on film thickness. *© 2003 MAIK "Nauka/Interperiodica".*

Unusual properties of ultrathin metal films interacting with electromagnetic radiation have been known for a long time. Special effects are observed when radiation is transmitted through thin metal films with thicknesses below the skin layer depth. Although the electric field is virtually not attenuated in such a film because of extremely small metal thickness, the film is strongly reflecting and exhibits an absorption maximum. This behavior can be explained by manifestations of the anomalous skin effect [1]. If the film thickness is comparable with the mean free path of electrons l_0 in a thick metal layer, the pathlength is determined predominantly by reflections from the boundaries, rather than by interactions with the crystal lattice. Detailed theoretical description of the optical properties of metal films for the normal incidence of radiation in the SHF and radio wavelength range was given by Kaplan [2]. It was demonstrated that the optical characteristics of the films with thicknesses much smaller than the skin layer depth are independent of the radiation frequency.

We have studied the coefficients of reflection, transmission, and absorption of thin aluminum films exposed to radiation with a wavelength of 8 mm.

The experiments were performed with thin aluminum films prepared by thermal deposition in vacuum. This technique allows the deposit thickness to be readily controlled and ensures good quality of the films and reproducibility of their properties. The films were deposited onto polished quartz glass substrates with a thickness of 2.3 mm. The metal for deposition was selected for the following reasons: aluminum films are characterized by a very strong adhesion to glass, are sufficiently hard, and possess high corrosion resistance due to the presence of a spontaneously formed protective film of aluminum oxide (this is especially important in cases of contact with water [3]). Homogeneity of the film thickness over the glass substrate surface was ensured by using a point evaporator situated a large distance from the substrate. The film thickness scatter over the sample area did not exceed 5%. The film thicknesses were determined to within 0.5 nm by a Talystep profilometer.

A scheme used to measure the characteristics of the films was based on a panoramic VSWR meter of the R2-65 type and allowed simultaneous determination of the reflection and transmission coefficient. The reflection coefficient was calibrated by measuring the reflection from a metal plate placed on the position of the aluminum film. The absorption coefficient was calculated by the formula

$$A = 1 - R - T, \quad (1)$$

where $R = P_2/P_1$ is the reflection coefficient, $T = P_3/P_1$ is the transmission coefficient, and P_1, P_2, P_3 are the powers of incident, reflected, and transmitted waves, respectively.

Figure 1 shows a model of the three-layer structure studied. The experiments were performed in two modes of the SHF radiation incidence onto the aluminum film surface (from glass and from air). Figure 2 shows the results of measurements of the reflection, transmission, and absorption of aluminum films depending on their thicknesses *d* varied from 1.7 to 15 nm. Manufacturing films with thicknesses below 1.5 nm encountered considerable technical difficulties and the results of measurements for such films exhibited large scatter. For a film thickness of 15 nm and above, the reflection and transmission coefficients virtually ceased to change. As the film thickness was increased in the interval studied, the reflection coefficient exhibited monotonic growth, nearly approaching unity. Accordingly, the transmission coefficient was almost zero at a film thickness of 6–8 nm.

As can be seen from Fig. 2, the transmission coefficients are virtually the same for the radiation incident onto the film from air (Fig. 2a) and from glass (Fig. 2b). The coefficient of absorption exhibits a maximum in

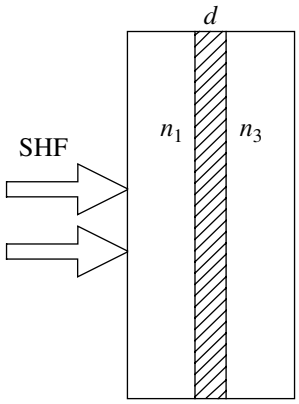

Fig. 1. The model of a three-layer structure exposed to SHF radiation (n_1 and n_3 are the refractive indices of glass and air and d is the metal film thickness).

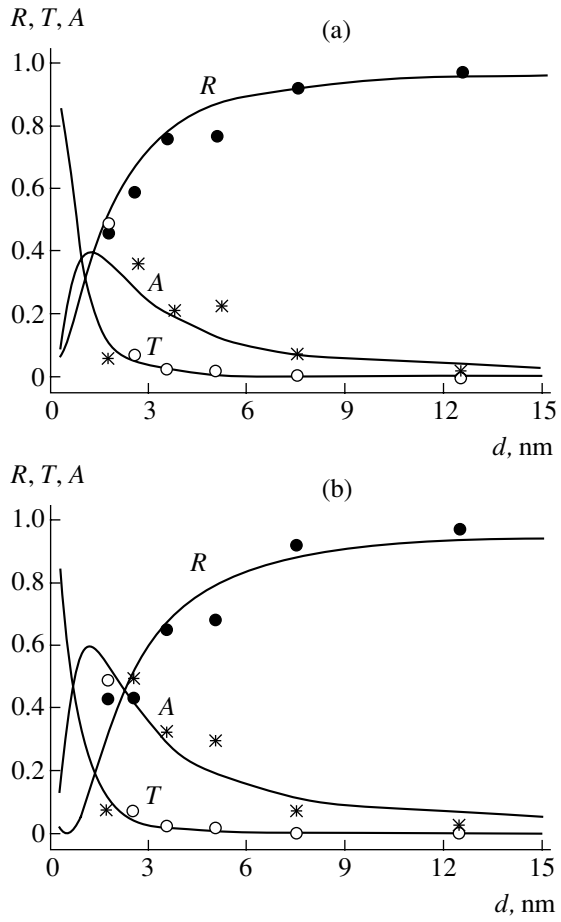

Fig. 2. Experimental (symbols) and theoretical (solid curves) plots of the optical coefficients of thin aluminum films versus film thickness with allowance for the given substrate material: (a) SHF radiation is incident onto the metal film surface in a three-layer structure of air ($n_1 = 1$), film, and glass ($n_3 = 1.5$); (b) SHF radiation is incident onto the metal film from glass in a three-layer structure of glass ($n_1 = 1.5$), film, and air ($n_3 = 1$).

the region of film thickness of about 2–3 nm, the maximum A value measured for the radiation incident glass ($A_m = 0.49$) exceeding the analogous value for the incidence from air ($A_m = 0.34$). The error of the determination of optical characteristics in our experiments did not exceed 5–7%.

A theoretical analysis of the behavior of optical coefficients determined for the normal incidence of a plane wave onto the three-layer structure studied (Fig. 1) leads to the following relations:

$$R = \frac{\left((n_3 - n_1) + 2\frac{d}{b}\right)^2}{\left((n_3 + n_1) + 2\frac{d}{b}\right)^2}, \quad T = \frac{4n_1n_3}{\left((n_3 + n_1) + 2\frac{d}{b}\right)^2}, \quad A = \frac{8\frac{d}{b}n_1}{\left((n_3 + n_1) + 2\frac{d}{b}\right)^2}, \tag{2}$$

where d is the film thickness, $b = c/2\pi\sigma$, and σ is the metal conductivity. With allowance for the size effects (for $d \le l_0$), the conductivity of a continuous metal film as a function of the film thickness (for $d \sim 10$ nm) is described by the expression [4]

$$\sigma(d) = \sigma_0(d/2l_0)(1 + \ln(l_0/d)). \tag{3}$$

Here, σ_0 is the bulk metal conductivity and l_0 is the mean free path of electrons in a thick metal layer. For aluminum, $\sigma_0 = 3.54 \times 10^7$ S/m and $l_0 = 15$ nm (at room temperature).

Figure 2 (solid curves) shows the values of R, T, and A calculated using formulas (2) and (3) as functions of the film thickness for the two orientations relative to the radiation source. Note that the absorption coefficient of aluminum films exhibits a maximum at a film thickness of 1.3 nm and the maximum absorption for the radiation incident from glass is greater by a factor of $n_3/n_1 = 1.5$ than that for the radiation incident from air.

As can be seen from Fig. 2, the experimental and theoretical results are in good agreement, beginning with a film thickness of 3 nm. At smaller film thicknesses, the experimental values are also qualitatively consistent with the theory. Both theory and experiment show a maximum in the dependence of the absorption coefficient on film thickness. The experimental ratio of maximum values of the absorption coefficient for the radiation incident from the glass substrate and from air is 1.44, which is close to the theoretical value. However, the maximum absorption was experimentally

observed at a film thickness of 2.5 nm, which is about two times greater than the theoretical value.

The experimental behavior of the optical characteristics can be explained as follows. A continuous film of aluminum is formed beginning with a deposit thickness of about 3 nm. Below this value, the film is inhomogeneous and exhibits the properties of an "island" structure. This circumstance significantly influences the conductivity, so that $\sigma(d)$ may differ from the value (3) predicted by the theory. In addition, the aluminum film surface is always covered by a metal oxide film. In the case of Al_2O_3, the oxide thickness may reach 1–2 nm. This oxide will affect the overall film conductivity. A decrease in conductivity probably accounts for a shift of the absorption maximum toward greater film thicknesses.

Acknowledgments. This study was supported by the Russian Foundation for Basic Research, project no. 01-02-17344.

REFERENCES

1. G. E. H. Reuter and E. H. Sondheimer, Proc. R. Soc. London, Ser. A **195**, 336 (1948).
2. A. E. Kaplan, Radiotekh. Élektron. (Moscow) **9**, 1781 (1964).
3. V. G. Andreev, V. A. Vdovin, and A. A. Karabutov, Izv. Ross. Akad. Nauk, Ser. Fiz. **66**, 1750 (2002).
4. G. V. Rosenberg, *Optics of Thin Coatings* (Fizmatgiz, Moscow, 1958).

Translated by P. Pozdeev

Technical Physics Letters, Vol. 29, No. 11, 2003, pp. 956–958. Translated from Pis'ma v Zhurnal Tekhnicheskoĭ Fiziki, Vol. 29, No. 22, 2003, pp. 74–79.

Determination of the Relaxation Time Distribution Function from Dielectric Losses

S. A. Ktitorov

Ioffe Physicotechnical Institute, Russian Academy of Sciences, St. Petersburg, 194021 Russia

e-mail: ktitorov@mail.ioffe.ru

Received June 2, 2003

Abstract—Conditions for reconstructing the relaxation time distribution function from the frequency dependence of dielectric losses have been studied using an approach analogous to that employed in the communication theory (Kotel'nikov–Shannon theorem). © *2003 MAIK "Nauka/Interperiodica".*

The traditional approach to description of dielectric relaxation in nonregular systems (polymers, impure ferroelectrics, etc.) and magnetic relaxation in disordered media of the spin glass type consists in introducing a continuous relaxation time distribution function (RTDF) [1]. In addition to theoretical models, it is important to develop a justified procedure for determining RTDF from the measured functions of dielectric ($\epsilon(\omega)$) or magnetic ($\mu(\omega)$) losses. For definiteness, the considerations below are restricted to the case of dielectrics, but the results are equally applicable to magnets.

An exact formula relating the dielectric losses and RTDF was derived by Fuoss and Kirkwood [2]. However, this relation cannot be directly used in practice because of non-uniqueness of the analytical continuation (see discussion below). Interest in this problem does not fade, and various approaches are periodically considered. In particular, numerical solutions of the general integral equation were attempted in [3, 4]. The aim of this study was to develop a justified procedure for determining the RTDF from the frequency dependence of dielectric losses.

RTDF $g(\ln(\tau/\tau_0))$ is introduced by a relation [5],

$$\chi(\mu) = \int_{-\infty}^{\infty} \chi_D(\omega\tau) g(\ln(\tau/\tau_0)) d\ln(\tau/\tau_0), \quad (1)$$

$$\chi_D(\omega\tau) = \frac{\epsilon_D(\omega\tau) - \epsilon_\infty}{\epsilon_0 - \epsilon_\infty} = \frac{1}{1 - i\omega\tau}, \quad (2)$$

where $\epsilon_D(\omega\tau)$ is the permittivity of a system of Debye relaxors with a single relaxation time; ϵ_0 and ϵ_∞ are the low- and high-frequency limits of the permittivity, respectively; and τ_0 is an arbitrary time scale. It should be noted that RTDFs are frequently estimated based on intuitive considerations, by assuming that $g(\ln(\tau/\tau_0)) = \mathrm{Im}\chi(\ln(\omega\tau_0))$. This Letter is aimed at outlining a regular and justified procedure.

Introducing logarithmic variables $z = \ln(\tau/\tau_0)$, $\omega\tau_0 = \Omega$, $\tau/\tau_0 = \exp(z)$, $\Omega = \exp(-\mu)$, $\omega\tau = \Omega\exp(z) = \exp(z - \mu)$, and $y = -\ln(\omega\tau_0)$, we can rewrite Eq. (1) as follows:

$$\chi(y) = +\int_{-\infty}^{\infty} dx \frac{g(x)}{1 - i\exp(x - y)}. \quad (3)$$

The integral equation (3) can be solved by using an exact Fourier transform. This yields for the imaginary part

$$\chi''(\mu) = \int_{-\infty}^{\infty} dz \frac{g(z)\Omega\exp(z)}{1 + \Omega^2\exp(2z)} \quad (4)$$

$$= \int_{-\infty}^{\infty} dz \frac{g(z)\exp(z - \mu)}{1 + \exp(2(z - \mu))} = \frac{1}{2}\int_{-\infty}^{\infty} dz \frac{g(z)}{\cosh(z - \mu)}. \quad (5)$$

Writing Eq. (5) in the standard form,

$$\chi''(\mu) = \int_{-\infty}^{\infty} dz K(\mu - z) g(z) \quad (6)$$

and using the Fourier transform

$$\chi''_y = \int_{-\infty}^{\infty} dz \exp(iyz)\chi''(z), \quad (7)$$

$$g_y = \int_{-\infty}^{\infty} dz \exp(iyz) g(z), \quad (8)$$

$$K(z - \mu) = 1/[2\cosh(z - \mu)], \quad (9)$$

we arrive at an algebraic equation

$$\chi''_y = K_y g_y. \quad (10)$$

1063-7850/03/2911-0956$24.00

Using the known integral [7],

$$\int_0^\infty dx \frac{\cos xy}{\cosh \alpha x} = \frac{\pi}{2\alpha \cosh\left(\frac{\pi y}{2\alpha}\right)}, \quad (11)$$

we obtain

$$K_y = \pi/[2\cosh(\pi y/2)]. \quad (12)$$

Thus, the Fourier transform of the solution is

$$g_y = 2\pi^{-1}\chi''_y \cosh(\pi y/2).$$

Taking the inverse Fourier transform,

$$g(z) = \int_{-\infty}^{\infty} \frac{dy}{2\pi} \exp(-iyz) g_y, \quad (13)$$

we can, in principle, calculate the RTDF from the known dielectric loss function $\chi''(\mu)$. These integrals can be calculated numerically, provided that the measured imaginary part of the permittivity is also available in the numerical form. Unfortunately, this pathway unavoidably encounters a difficulty related to a very slow convergence of the related integrals. However, there is an alternative possibility: once the analytical properties of the loss function are known, the integral can be exactly calculated in the general form. Assuming uniform convergence in the entire integration region, we can change the order of integration (in fact, the condition of uniform convergence can be reduced in accordance with the theory of generalized functions [8]):

$$\begin{aligned} g(z) &= \frac{1}{2\pi^2}\int_{-\infty}^{\infty} dy \int_{-\infty}^{\infty} d\mu \exp[(\mu - z)yi] \\ &\quad \times \chi''(\mu)[\exp(\pi y/2) + \exp(-\pi y/2)] \\ &= \frac{1}{\pi}\int_{-\infty}^{\infty} d\mu \chi''(\mu)[\delta(z - \mu + i\pi/2) + \delta(z - \mu - i\pi/2)] \\ &= \frac{1}{\pi}[\chi''(z + i\pi/2) + \chi''(z - i\pi/2)]. \end{aligned} \quad (14)$$

Fuoss and Kirkwood [2] derived this equation in a different way. Difficulty of the practical application of Eq. (14) is related to non-uniqueness of the analytical continuation.

Let us consider the possible ways of using formula (14) in practice. Assuming that $\chi''(z)$ is differentiable at least to the second order and slowly varying function, and expanding this function in powers of $i\pi/2$, we can write the solution in an approximate form:

$$g(z) \approx \frac{2}{\pi}\left[\chi''(z) - \frac{\pi^2}{8}\frac{d^2\chi''(z)}{dz^2} + \ldots\right]. \quad (15)$$

This approximate formula is asymptotically correct for slowly varying dielectric loss functions. At the same time, formula (14) can be used, in principle, in the most general case although non-uniqueness of the analytical continuation makes this possibility problematic. There are two principal difficulties. First, analytical properties of the loss function cannot be uniquely determined based on the results of measurements in a restricted frequency range. Second, the measurements are performed in a finite number of points in this frequency range. This implies that the analytical properties of the loss function have to be determined independently.

An analogous problem is encountered in the theory of communications, where discretization of the signal and the impossibility of transmitting a signal with unlimited spectrum via a communication channel necessitates optimization of the channel. This optimization is based on the Kotel'nikov–Shannon theorem [9], which is analogous to an approach previously developed in the mathematical approximation theory. The main idea of this approach consists in limiting the class of functions describing the transmitted signal. Following the spirit of this theory, we assume that $\chi''(z)$ is an integral function of finite power α [9]:

$$\lim_{r\to\infty} \frac{\ln \max_{|z|=r}|\chi''(z)|}{r^2} = \alpha < +\infty. \quad (16)$$

According to the Paley–Wiener theorem [6], such a function possesses a limited spectrum. In the case under consideration, the physical meaning of this result is as follows. The spectrum of the function $\chi''(z)$ characterizes time evolution of the polarization; the width of the spectrum corresponds to the maximum relaxation time (on the logarithmic scale); therefore, a limited spectrum of the loss function implies virtually complete relaxation of polarization over a finite interval of time. Theoretically, the process of relaxation in glasses is infinite (power and logarithmic tails of the response functions). In practice, however, the maximum possible (experimentally measured) response times are limited by noise and by instability of the parameter setting (frequency, temperature, etc.).

Therefore, we may require that the loss function $\chi''(z)$ is the integral function of a finite power. Let $\chi''(z)$ be a function with the spectrum g_y determined by Eq. (8) in the interval $-\beta < y < \beta$. For $\alpha > \beta$, we obtain the following expression for the loss function:

$$\chi''(z) = \sum_{k=-\infty}^{\infty} \chi''\left(k\frac{\pi}{\alpha}\right) \frac{\sin\alpha\left(z - k\frac{\pi}{\alpha}\right)}{\alpha\left(z - k\frac{\pi}{\alpha}\right)}. \quad (17)$$

This series uniformly converges to an entire analytical function and admits analytical continuation. Sub-

stituting formula (14) into (17), we eventually arrive at

$$g(z) = \frac{1}{\pi}\int_{k=-\infty}^{\infty} \chi''\left(k\frac{\pi}{\alpha}\right) \times\left[\frac{\sin\alpha\left(z + i\frac{\pi}{2} - k\frac{\pi}{\alpha}\right)}{\alpha\left(z - k\frac{\pi}{\alpha}\right)} + \frac{\sin\alpha\left(z - i\frac{\pi}{2} - k\frac{\pi}{\alpha}\right)}{\alpha\left(z - k\frac{\pi}{\alpha}\right)}\right] \quad (18)$$

$$= \frac{\cosh\frac{\alpha\pi}{2}}{\pi}\sum_{k=-\infty}^{\infty} \chi''\left(k\frac{\pi}{\alpha}\right)\frac{\sin\alpha\left(z - k\frac{\pi}{\alpha}\right)}{\alpha\left(z - k\frac{\pi}{\alpha}\right)}.$$

Thus, it was demonstrated that, in the case of a finite response time, the "naive" solution $g(z) \propto \chi''(z)$ is exact in the class of integral analytical functions. Although any real measurements yield a response of finite duration, it would be of interest to generalize the above results so as to include the case of response functions having power or logarithmic asymptotics. This will be done in future investigations.

REFERENCES

1. S. L. Ginzburg, *Irreversible Processes in Spin Glasses* (Nauka, Moscow, 1989).
2. R. M. Fuoss and J. G. Kirkwood, J. Am. Chem. Soc. **63**, 385 (1941).
3. H. Schäfer, E. Sternin, R. Stannarius, *et al.*, Phys. Rev. Lett. **76**, 2177 (1996).
4. R. Pelster, T. Kruse, H. G. Krauthäuser, *et al.*, Phys. Rev. B **57**, 8763 (1998).
5. C. J. F. Böttcher, *Theory of Electric Polarization* (Elsevier, Amsterdam, 1952).
6. E. C. Titchmarsh, *Introduction to the Theory of Fourier Integrals* (Clarendon Press, Oxford, 1948; Gostekhizdat, Moscow, 1948).
7. I. S. Gradshtein, *Table of Integrals, Series, and Products* (Fizmatgiz, Moscow, 1963; Academic, New York, 1980).
8. L. Schwartz, *Mathematics for the Physical Sciences* (Addison-Wesley, Reading, 1966; Mir, Moscow, 1965).
9. Ya. I. Khurgin and V. P. Yakovlev, *Methods of Theory of Integer Functions in Radio Physics, Theory of Communication, and Optics* (Fizmatgiz, Moscow, 1962).

Translated by P. Pozdeev

Technical Physics Letters, Vol. 29, No. 11, 2003, pp. 959–962. Translated from Pis'ma v Zhurnal Tekhnicheskoĭ Fiziki, Vol. 29, No. 22, 2003, pp. 80–87.

Cadmium Telluride Thin-Film Detectors of Nuclear Radiation

B. N. Zaveryukhin, Sh. A. Mirsagatov, N. N. Zaveryukhina, V. V. Volodarskiĭ, and E. B. Zaveryukhina

Physical Engineering Institute, "Solar Physics" Research and Production Corporation, Academy of Sciences of the Republic of Uzbekistan, Tashkent, Uzbekistan

e-mail: oybtm@physic.uzsci.net

PSP Company, Kaluga oblast, Russia

National University of Uzbekistan, Tashkent, Uzbekistan

Received March 17, 2003; in final form, June 11, 2003

Abstract—Semiconductor detectors for X-ray and γ radiation are developed based on thin cadmium telluride (*p*–*n*-CdTe) films possessing a columnar structure. The detector structures are formed on molybdenum substrates by CdTe sublimation and magnetron sputtering of cadmium. The *p*-CdTe films have a thickness of d = 30–150 μm and a resistivity of $\rho \geq 10^3$–10^7 Ω cm. The single crystal grains in the films have an average size of 50–100 μm and are oriented perpendicularly with respect to the Mo substrate. In comparison to the usual single crystal CdTe detectors, the proposed thin-film single crystal CdTe detectors possess a more perfect structure, since the grain boundaries act as effective sinks for defects. The energy resolution of the new generation of CdTe detectors reaches ~5 keV for the 59.6 keV line of ^{241}Am at room temperature. © *2003 MAIK "Nauka/Interperiodica".*

Currently, there is growing interest in thin-film semiconductor detectors of nuclear radiation, formed on the surface of single crystal semiconductors [1–3]. The base semiconductors are typically GaAs and SiC. GaAs has an effective atomic number Z close to that of germanium ($Z_{GaAs} \sim 31$) and, hence, cannot provide for a sufficiently high efficiency of detection, while SiC detector is principally inapplicable to the detection of X-ray and γ radiation.

Most promising candidates for the development of uncooled semiconductor detectors of X-ray, γ, and other types of nuclear radiation are semiconductor compounds of the $A^{II}B^{VI}$ type. Single crystal detectors based on CdTe ($Z_{CdTe} \sim 48$) and $Cd_{1-x}Zn_xTe$ have proved to be advantageous over the Si and GaAs based devices and can be successfully used in the spectrometry of X-ray and γ radiation in a broad range of energies E. The energy resolution R of single crystal CdTe detectors at room temperature reaches $R \cong 0.83$ keV for the line with E = 59.6 keV of a ^{241}Am source and $R \cong$ 1.2 keV for the line with E = 662 keV of a ^{137}Cs source [4–6]. The only (but serious) disadvantage of the $A^{II}B^{VI}$ single crystals for detectors obtained by various methods is the presence of a considerable amount of various defects negatively influencing the detector performance [7].

An analysis of the published data showed that thin-film single crystal CdTe detectors have not been developed so far. This study was aimed at the development of a manufacturing technology and the investigation of the main working characteristics of CdTe detectors based on thin single crystal films. The technology of new CdTe thin-film detectors (CdTe-TFDs) is developed from existing technology of effective thin-film photoconverters (TFPCs) based on polycrystalline CdTe films possessing a columnar structure, which was developed by one of the authors [8, 9]. The CdTe-TFPCs have been created and characterized [10, 11]. The technology of CdTe-TFDs has certain distinctions from that of TFPCs, related to special requirements posed on both the device and the material—in particular, low noise at full depletion voltage, the absence of a "dead layer," and large lifetime τ of minority carriers.

We have refined the TFPC technology and developed thin-film *p*-CdTe–*n*-CdTe structures for detectors. The base material represented polycrystalline *p*-CdTe films with a columnar structure, grown on molybdenum substrates by CdTe sublimation in a hydrogen flow. The film thicknesses range within d = 30–150 μm. It was established by etching that *p*-CdTe films are composed of single crystal grains with dimensions L = 30–150 μm oriented in the growth direction (i.e., perpendicularly to the Mo substrate plane). The grains have a diameter of k = 50–100 μm and are spaced by l = 50–70 Å. The rectangular samples of *p*-CdTe films possess a resistivity of $\rho = 10^3$–10^7 Ω cm and an area of S = 0.25–4 cm^2. The lifetime of minority carriers was $\tau \cong$ 50–70 μs. In the direction perpendicular to the Mo substrate, the *p*-CdTe

1063-7850/03/2911-0959$24.00

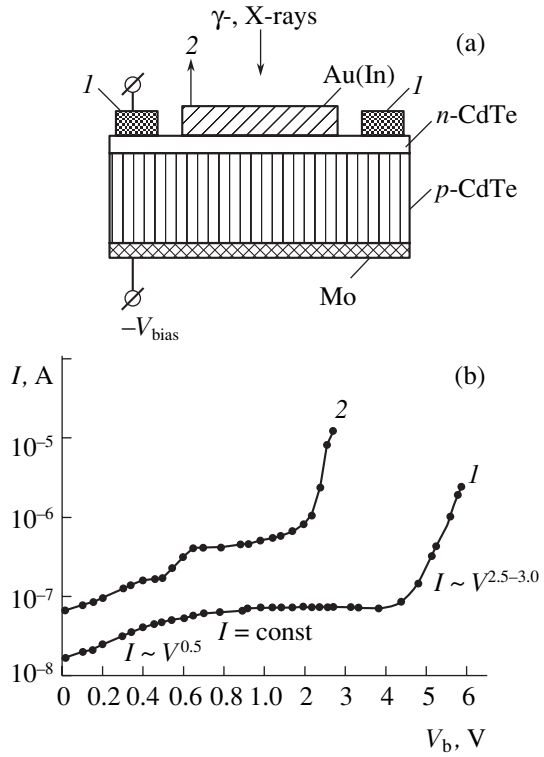

Fig. 1. Thin-film CdTe detectors: (a) structure showing (*1*) storage electrodes and (*2*) contacts to pulse electronics; (b) current–voltage characteristics measured at $T = 293$ K for (*1*) CdTe-TFD no. 05 ($d = 150$ μm, $S = 0.36$ cm^2) and (*2*) CdTe-TFD no. 04 ($d = 150$ μm, $S = 0.36$ cm^2).

film structure can be considered to be composed of single crystals separated by high-ohmic spacers. The properties of semiconductor devices employing charge carrier transport are determined predominantly by the properties of *p*-CdTe grains rather than grain boundaries.

The recombination characteristics of thin-film CdTe structures were studied previously [12]. It was also established [13] that the transport properties of polycrystalline CdTe layers are comparable with those of high-quality CdTe single crystals, since the grain boundaries in CdTe films with columnar structure can act as effective sinks for various structural defects [14]. The results of investigations showed that the synthesis of coarse-grained polycrystalline CdTe films is accompanied by the formation of free tellurium atoms due to re-evaporation of the volatile component (Cd). Interacting with residual oxygen present in the reactor, these Te atoms form high-ohmic TeO_2 layers, which passivate surface states in the grain boundaries [15–17]. This leads to a decrease in the surface recombination and to a significant increase in the lifetime of minority carriers (up to several dozen microseconds) [18]. The X-ray diffraction measurements showed that some *p*-CdTe films contain inclusions of the $CdTe_2O_3$, Mo_3Te_4, and MoO_2 types at the *p*-CdTe–Mo interface and $CdTe_2O_3$ inclusions in the bulk. Magnetron sputtering in an oxygen-containing atmosphere was used to deposit Cd onto the surface of *p*-CdTe films, so that a heterostructure of the type *p*-CdTe–*n*-CdTe–*n*-CdO was formed in a single technological cycle.

The geometric parameters and physical characteristics of *n*-CdTe layers obtained using the proposed technology were reported in [8, 9]. The results of investigations of the current–voltage, capacitance–voltage, and photoelectric characteristics and the potential and thermo emf measurements in oblique sections of the CdTe–CdO structure showed that (i) *n*-CdTe layers have a thickness of $l_k = 0.1$–1 μm and an equilibrium electron density of $n_0 \cong 10^{12}$ cm^{-3}; (ii) CdO layers have a bandgap width of $E_g \cong 2.7$ eV, a resistivity of $\rho \cong 4 \times 10^{-3}$ Ω cm, an electron mobility of $\mu_n \cong 100$–120 cm^2/(V s), and a shallow donor concentration of $N_D \cong 10^{20}$ cm^{-3}.

The surface barrier junction was created by a special chemical treatment of the *n*-CdTe surface in Mo–*p*-CdTe–*n*-CdTe–*n*-CdO structures. This treatment is one of the main stages in the proposed technology, determining the thickness of both the sensitive region and the "dead layer" of the detector. In the first step, the CdO layer is removed by chemical etching. The type and regime of chemical etching in the subsequent step provide for the obtaining of *n*-CdTe layers that are highly homogeneous over the entire working area of the detector. Chemical polishing and ultrasonic treatment of the *n*-CdTe layer render this layer still more homogeneous and provide for a homogeneous potential distribution on the surface.[1] It should be noted that the Mo–*p*-CdTe–*n*-CdTe structures not subjected to ultrasonic treatment at various intensities and frequencies (in MHz range) exhibited low functional and physical characteristics. An increase in the properties of ultrasound-treated Mo–*p*-CdTe–*n*-CdTe structures is probably related to the process of surface passivation similar to that studied in polycrystalline silicon TFPCs [19].

Figure 1a shows the design of a thin-film CdTe detector structure. The electric contacts and storage electrodes were applied to the entrance window of *n*-CdTe by thermal deposition of indium and gold in a vacuum via special masks. The surface density of the vacuum-deposited metals was 30–50 μg/cm^2. Below we will consider the results of experimental investigations of a particular sample of a thin-film CdTe detector.

As can be seen from Fig. 1b, the reverse branch of the current–voltage (*I–V*) characteristic of CdTe-TFD no. 05 can be subdivided into three regions. The first region is characterized by a sublinear dependence of

[1] Investigations of the acoustic-wave-induced effects in thin Si and GaAs layers showed that ultrasound modifies the properties of semiconductor films [19]. Description of the influence of the ultrasonic treatment on the characteristics of CdTe layers is beyond the scope of this publication. These results will be published separately.

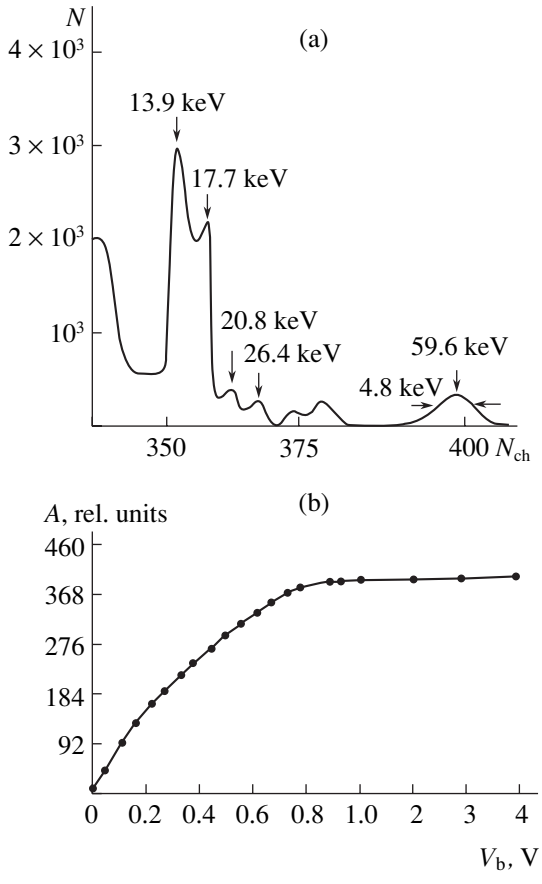

Fig. 2. Thin-film CdTe detector characteristics: (a) amplitude spectrum of an ^{241}Am source (N_{ch} is the channel number) measured with CdTe-TFD no. 05 at T = 293 K (V_b = 4.3 V); (b) amplitude versus bias voltage curve for CdTe-TFD no. 05 at T = 293 K.

the type $I \sim V_b^\alpha$ with $\alpha \geq 0.5$ (V_b is the bias voltage). The second region exhibits saturation ($I \sim$ const), evidencing the presence of a noninjecting base contact with a low junction resistance. This implies that the given CdTe-TFD operates in a full depletion regime (in the given V_b interval) and the *n–p* junction field reaches the Mo contact. In the case of a rectifying base contact, the reverse current and nose of the detector are significantly increased (Fig. 1b, curve *2*, CdTE-TFD no. 4). In the third region, the $I(V_b)$ curve is described by the dependence $I \sim V_b^\alpha$ with $\alpha > 2$. The results of our investigations showed that the temperature dependence of current for the CdTe-TFD with a sublinear dependence ($I \sim V_b^{0.5}$) at a fixed $V_b \leq 0.3$ V exhibits an activated character with an activation energy of $\Delta E \cong 0.73$ eV $\pm$ 0.02 eV. This ΔE value agrees quite well with the bandgap width of CdTe, which implies that the current is limited by generation in the space charge region [20].

The energy resolution R of CdTe-TFDs was studied using a pulsed electronic system of the ORTEC type with an AI-1024-95 multichannel analyzer. The electromagnetic radiation beam from an ^{241}Am source had a diameter of 0.5 cm. The CdTe-TFDs studied exhibited the following characteristics: (i) full depletion voltage, from 0.7 to 6 V; (ii) reverse current at a working bias voltage, from 5×10^{-8} to 10^{-6} A; (iii) energy resolution for X-ray and γ radiation in the energy range $E \cong$ 5–60 keV, $R \cong$ 5–10 keV (Fig. 2a). The plots of the signal amplitude versus V_b (Fig. 2b) for the CdTe-TFD studied and their extrapolation to the origin were indicative of a high homogeneity and structural perfection of the sensitive regions of detectors formed by a set of independent parallel single crystals [21]. Otherwise, the voltage dependence $A(V_b)$ and the temperature dependence $A(T)$ would exhibit anomalous regions [22, 23]. All the CdTe-TFD tested showed stability of working parameters when tested after a 2-month storage under ambient conditions at T = 293 K.

Conclusion. We have manufactured CdTe detectors of X-ray and γ radiation based on thin single crystal films possessing a columnar structure. The energy resolution R of the best thin-film CdTe detectors approaches that of single-crystal detectors. Further improvement of the CdTe-TFD structure, for example, by increasing the quality of the rear contact (elimination of various inclusions present at the *p*-CdTe–Mo interface), will additionally improve the resolution. High sensitivity with respect to X-ray and γ radiation makes the proposed detectors promising in practical applications.

Acknowledgments. The authors are grateful to N.N. Chernikov (Moscow) for stimulation of the investigation.

REFERENCES

1. V. M. Botnaryuk, Yu. V. Zhilyaev, A. M. Ivanov, *et al.*, Pis'ma Zh. Tekh. Fiz. **24** (7), 8 (1998) [Tech. Phys. Lett. **24**, 250 (1998)].
2. A. M. Ivanov, N. B. Strokan, D. V. Davydov, *et al.*, Fiz. Tekh. Poluprovodn. (St. Petersburg) **35**, 495 (2001) [Semiconductors **35**, 481 (2001)].
3. N. B. Strokan, A. M. Ivanov, N. S. Savkina, *et al.*, Fiz. Tekh. Poluprovodn. (St. Petersburg) **36**, 375 (2002) [Semiconductors **36**, 354 (2002)].
4. T. Takahashi, B. Paul, K. Hirose, *et al.*, Nucl. Instrum. Methods Phys. Res. A **436**, 111 (1999).
5. S. Matsumoto, T. Takahashi, K. Tikizawa, *et al.*, IEEE Trans. Nucl. Sci. **45**, 428 (1998).
6. T. Takahashi, K. Horise, S. Matsumoto, *et al.*, Proc. SPIE **34**–**46**, 29 (1998).
7. H. Hermon, M. Shieber, R. B. James, *et al.*, J. Electron. Mater. **28**, 688 (1999).
8. Sh. A. Mirsagatov and D. T. Rasulov, Dokl. Akad. Nauk Resp. Uzb., No. 7, 28 (1977).
9. S. A. Azimov, Sh. A. Mirsagatov, and S. A. Muzafarova, Geliotekhnika, No. 4, 7 (1982).
10. R. W. Burkmire *et al.*, in *Proceedings of the 18th IEEE Photovoltaics Spectral Conference, New York, 1985*, pp. 1413–1416.

11. T. Nakasawa and K. Takomirawa, Appl. Phys. Lett. **5** (5), 279 (1987).
12. Sh. A. Mirsagatov, K. Sabirov, and S. A. Muzafarova, Fiz. Tekh. Poluprovodn. (Leningrad) **21**, 733 (1987) [Sov. Phys. Semicond. **21**, 448 (1987)].
13. G. Gyaryagdyev, A. V. Lyubchenko, and S. A. Sypko, in *Proceedings of the 2nd Scientific Conference on Physics and Chemistry of Semiconductors, Ashkhabad, 1991* (Ylym, Ashkhabad, 1991), pp. 41–42.
14. N. N. Kristoffel, *Theory of Small-Radius Impurity Centers in Ionic Crystals* (Nauka, Moscow, 1974).
15. Sh. A. Mirsagatov, Doctoral Dissertation (Baku, 1988).
16. B. T. Boĭko, V. R. Kopach, *et al.*, Geliotekhnika, No. 6, 7 (1983).
17. A. Elina, A. Asano, and T. J. Takahaski, Phys. Rev. B **22**, 1980 (1980).
18. A. V. Gorshkov, F. A. Zaitov, Sh. A. Mirsagatov, *et al.*, Dokl. Akad. Nauk Resp. Azerb. **37** (11), 31 (1981).
19. B. N. Zaveryukhin, N. N. Zaveryukhina, and O. M. Tursunkulov, Pis'ma Zh. Tekh. Fiz. **28** (18), 1 (2002) [Tech. Phys. Lett. **28**, 752 (2002)].
20. I. M. Vikulin and V. I. Stafeev, *Physics of Semiconductor Devices* (Sov. Radio, Moscow, 1980).
21. V. K. Eremin, Candidate's Dissertation (Leningrad, 1978).
22. V. K. Eremin, N. B. Strokan, B. N. Zaveryukhin, *et al.*, Fiz. Tekh. Poluprovodn. (Leningrad) **13**, 2407 (1979) [Sov. Phys. Semicond. **13**, 1409 (1979)].
23. B. N. Zaveryukhin, V. D. Krevchik, R. A. Muminov, *et al.*, Fiz. Tekh. Poluprovodn. (Leningrad) **20**, 525 (1986) [Sov. Phys. Semicond. **20**, 330 (1986)].

Translated by P. Pozdeev

Technical Physics Letters, Vol. 29, No. 11, 2003, pp. 963–965. Translated from Pis'ma v Zhurnal Tekhnicheskoĭ Fiziki, Vol. 29, No. 22, 2003, pp. 88–94.

Investigation of the Growth and Properties of Epitaxial Layers of $Si_{1-x}Sn_x$ Solid Solutions

B. Sapaev and A. S. Saidov

Physicotechnical Institute, "Solar Physics" Research and Production Corporation, Academy of Sciences of the Republic of Uzbekistan, Tashkent, Uzbekistan

e-mail: atvi@physic.uzsci.net

Received June 2, 2003

Abstract—Epitaxial layers of $Si_{1-x}Sn_x$ ($0 \le x \le 0.04$) solid solutions on silicon substrates were grown by liquid phase epitaxy in a temperature interval from 1050 to 950°C. Optimum conditions favoring the growth of crystallographically perfect epitaxial films of $Si_{1-x}Sn_x$ were established based on the results of the X-ray diffraction, X-ray radiometry, and morphology investigations. The obtained Si–$Si_{1-x}Sn_x$ structures are intended for use in the technology of various microelectronic devices. *© 2003 MAIK "Nauka/Interperiodica".*

The search for new solid solution systems based on Group IV semiconductors and semimetals with tetrahedral bonds, aimed at expanding the photosensitivity spectrum of semiconductor detectors to the longwave spectral range, is among the currently important problems in modern photoelectronics. Although the formation of solid solutions of the Si–Sn system, by analogy with the Si–Ge system, was considered as theoretically possible, no such solutions were obtained in experiment.

Previously [1], we reported on the growth of epitaxial layers of $Ge_{1-x}Sn_x$ solid solutions from a tin-based solution melt and showed that epilayers with perfect structures can be obtained by controlled cooling in a temperature interval of 450–740°C. Recently [2], the structure of substitutional solid solutions of the $Ge_{1-x}Sn_x$ system was studied by computer simulation using the molecular dynamics method. A comparison shows satisfactory agreement between theoretical and experimental values of lattice constants and indicates that the Vegard law is valid for $x < 0.7$.

The existence of Ge_2 and Si_2 molecules was predicted and experimentally confirmed in [3]. Following this analogy, it is possible to admit the existence of Si–Sn molecules that can form as a result of Sn substitution for Si atoms in the crystal lattice of silicon, the more so that Si and Sn are isovalent.

Below we present the results of experiments on the growth of a new diamondlike solid solution of the $Si_{1-x}Sn_x$ from the liquid phase. The layers of $Si_{1-x}Sn_x$ solid solutions were grown from a limited volume of tin-based solution melt in a palladium-purified hydrogen atmosphere. In order to obtain epilayers possessing preset electrical properties, it is necessary to know the mutual solubility of the elements and study the influence of various technological factors on the growth of the semiconductor compound. These include, in particular, the physical state of a solution melt contacting the substrate. The composition of a Sn–Si solution melt and the temperature interval of crystal growth were determined from published data [4] and from the results of experiments. The films were grown on substrates representing disks with a diameter of $D = 20$ mm and a thickness of $d = 350$–400 μm cut from single crystal silicon wafers of *n*- and *p*-type with a resistivity of $\rho_1 \sim 30\ \Omega$ cm and $\rho_2 = 0.5$–$3.0\ \Omega$ cm, respectively. The developed liquid phase epitaxy (LPE) technology is described in more detail elsewhere [5].

Depending on the crystallization start and end temperatures and the confined solution melt volume (i.e., on the gap between horizontal substrates), the thickness *d* of obtained epilayers varied from 3 to 70 μm. The distribution of chemical elements in the sample volume was studied and the epilayer thickness was determined by various methods.

The composition and thickness of grown epilayers were determined by X-ray radiometry [6]. The characteristic emission from Sn was excited by γ quanta from an ^{241}Am isotope source. The emission was detected by a pulsed spectrometry system comprising a Si(Li) detector with an energy resolution of $R = 300$ eV (for a ^{241}Am line with $E = 59.6$ keV) and a multichannel amplitude pulse analyzer of the AI-1024-95-02 type. Figure 1a shows the spectrum of the characteristic emission from Si, Sn, and Sb. An analysis of these emission lines showed that Sb was present in the epilayers, because the Si substrates were doped with this element. The component composition of $Si_{1-x}Sn_x$ solid solutions was determined by comparing the relative intensities of the characteristic spectral lines to the calibration curves constructed for a series of standard samples. The percentage compositions and the thicknesses

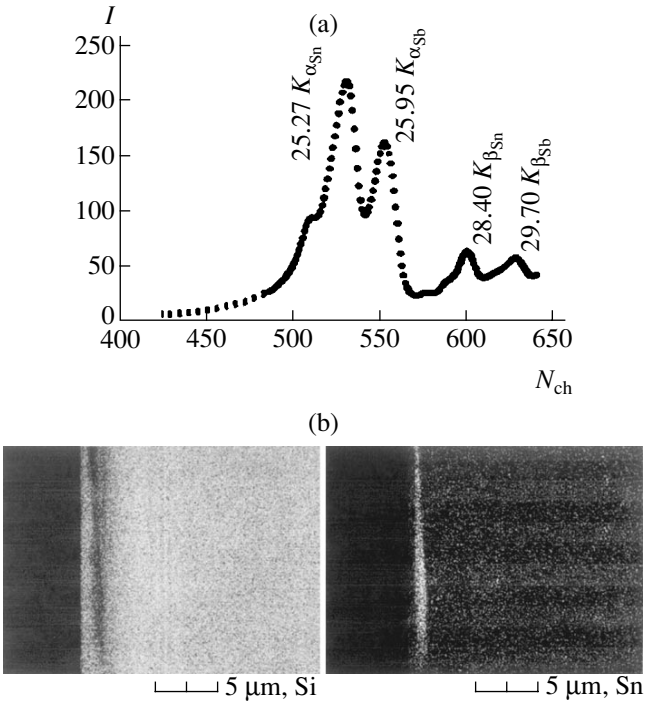

Fig. 1. Si–$Si_{1-x}Sn_x$ epilayers: (a) the characteristic spectrum of Sn and Sb excited by γ quanta from a ^{241}Am source; (b) scanning micrographs of the transverse cleavages of Si–$Si_{1-x}Sn_x$ structures.

of epilayers were determined using the known initial content of the initial element (in grams).

Compositions of the initial $Si_{1-x}Sn_x$ solid solutions and the distribution of components in the grown epilayers were studied on a JSM 5910LV X-ray electron-probe microanalyzer (JEOL, Japan). It was found that the x value falls within the interval $0 \le x \le 0.04$. The homogeneity of the component distribution both in depth of the epitaxial layer and in the directions parallel to the crystallization front depends on the melt composition and the crystallization start temperature. As the crystallization start temperature and the temperature interval (from start to end of the growth process) increase (under otherwise equal conditions and the same solution melt composition), the content of Sn in the $Si_{1-x}Sn_x$ solid solution tends to grow.

The quality of epitaxial $Si_{1-x}Sn_x$ layers grown on Si substrates was also dependent on the controlled cooling rate v, which was varied between 0.5 and 5.5 K/min. The optimum interval of cooling rate favoring the growth of mirror-smooth $Si_{1-x}Sn_x$ films was 0.5–1.5 K/min, which corresponded to the crystallization rate (front velocity) of v_k = 0.1–0.25 μm/min. In addition, the structural perfection of the grown semiconductor layers depended (under otherwise equal conditions) on the gap width δ between the horizontal substrates. This gap could be varied from 0.25 to 2.5 mm with the aid of special graphite spacers. For $\delta < 0.25$ mm, no epitaxial growth took place—probably because the melt did not wet the substrate surface. The most perfect layers of solid solutions on both upper and lower substrates were grown for $\delta = 0.5$–1.0 mm. For $\delta > 0.8$ mm, layers of significantly different quality were obtained on the upper and lower substrates: the quality of epitaxial films was always better on the lower substrates than on the upper ones. This was manifested, in particular, by a difference in the surface dislocation density N_D, which was about ten times smaller in the latter case. In our opinion, this is explained by the fact that the convective flows dominated over molecular diffusion in the overall mass transfer to the crystallization front [7]. The character of component distribution in depth of the epitaxial layers was qualitatively assessed by studying the transverse cleavages of Si–$Si_{1-x}Sn_x$ structures. An analysis of the scanning micrographs showed evidence of a highly homogeneous distribution of components across the epitaxial film (Fig. 1b).

An analysis of the scanning micrographs and the morphological study of $Si_{1-x}Sn_x$ solid solutions showed that defects appearing at the substrate–epilayer interface depend on the x value. A mismatch between the lattice parameters of substrate and the first crystallized solid solution layer appears because this layer comprises $Si_{1-x}Sn_x$ with $x > 0$, while the substrate is made of pure Si. As the subsequent epitaxial growth proceeds, this mismatch gradually decreases because the difference in x between the adjacent layers is insignificant. Elastic deformation of each completed layer, which serves as a substrate for the subsequent layer growth, leads to a decrease in the total system energy [8]. After the crystallization of each next layer without changing the lattice constant, this energy is always smaller than that in the initial process stage. By changing the growth regime, it is possible to control the perfection of heteroboundaries in the Si–$Si_{1-x}Sn_x$ structures.

The quality of the crystal structure was assessed and the lattice parameters of $Si_{1-x}Sn_x$ solid solutions were determined by X-ray diffraction measurements performed on a DRON-3M diffractometer. These measurements were performed on specially prepared Si–$Si_{1-x}Sn_x$ structures with a thickness of d = 3–5 μm. The diffractograms were obtained by continuous recording using filtered Cu$K_{\alpha 1}$ ($\lambda_{\alpha 1}$ = 1.54051 Å) and Cu$K_{\alpha 2}$ ($\lambda_{\alpha 2}$ = 1.54431 Å) radiation from an X-ray tube operating at 30 kV and 10 mA. Separate recording of the reflections from the same plane provided an increase in the accuracy of determination of the interplanar spacing d for the Miller indices hkl. The parameters of $Si_{1-x}Sn_x$ layers were determined in a regime of point-by-point scanning with a step not exceeding $2\theta = 0.01°$ (θ is the Bragg reflection angle) and a scanning time of τ = 20 s at each point.

As is seen from the typical diffractogram presented in Fig. 2, the positions of peaks from the film and substrate differ insignificantly. This implies that the lattice

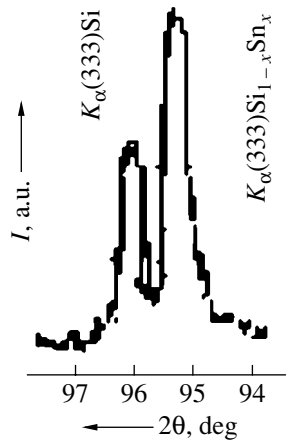

Fig. 2. A typical X-ray diffractogram of the Si–$Si_{1-x}Sn_x$ epitaxial structure.

parameters are also close to each other (a_{Si} = 5.4296 ± 0.0004 Å, $a_{Si_{1-x}Sn_x}$ = 5.4311 Å), while the absence of other peaks in the diffractogram is additional evidence of the single crystal structure of the obtained epilayers.

It should be noted that the intensity of reflections measured from the side of the epilayer was usually somewhat higher than that measured from the side of the silicon substrate (Fig. 2). This is most probably due to the extinction effect, whereby the lower planes are screened by the upper ones. This effect is frequently observed even in perfect single crystals of silicon [9]. On the rear side of the Si–$Si_{1-x}Sn_x$ structure (where a $Si_{1-x}Sn_x$ is present), the ideal periodicity of the silicon lattice is broken and the extinction effect decreases or vanishes completely, while the reflection intensity increases as compared to that on the side possessing a perfect crystal structure. The lattice parameter a was calculated by the formula $a = d\sqrt{h^2 + k^2 + l^2}$ [8].

According to an analysis of the preliminary experimental data, the resistivity of epilayers is $\rho \approx 0.5\ \Omega$ cm, the carrier density is ~10^{17} cm^{-3}, and the Hall mobility of the carriers is ~600 $cm^2/(V\ s)$.

Thus, we have experimentally demonstrated the possibility of growing high-quality epitaxial layers of $Si_{1-x}Sn_x$ solid solutions with $0 \le x \le 0.04$ on silicon substrates. The obtained Si–$Si_{1-x}Sn_x$ structures can find wide application in semiconductor microelectronics.

REFERENCES

1. A. S. Saidov, É. A. Koshchanov, and A. Sh. Razzakov, Pis'ma Zh. Tekh. Fiz. **27** (16), 71 (2001) [Tech. Phys. Lett. **27**, 698 (2001)].
2. V. G. Deĭbuk and Yu. T. Korolyuk, Fiz. Tekh. Poluprovodn. (St. Petersburg) **35**, 298 (2001) [Semiconductors **35**, 283 (2001)].
3. M. S. Saidov and A. A. Saidov, in *Proceedings of the 7th International Conference on Vapor Growth and Epitaxy, Nagoya, 1991*, p. 25.
4. V. M. Andreev, L. M. Dolginov, and D. N. Tret'yakov, *Liquid-Phase Epitaxy in Technology of Semiconductor Devices* (Sov. Radio, Moscow, 1975).
5. A. S. Saidov, A. Kutlimratov, B. Sapaev, *et al.*, Vest. Gulistansk. Gos. Univ., No. 2, 40 (2001).
6. S. V. Mamikanyan, *Fluorescence X-ray Radiometric Analysis: Apparatus and Methods* (Atomizdat, Moscow, 1976).
7. A. S. Saidov, B. Sapaev, É. A. Koshchanov, *et al.*, Dokl. Akad. Nauk Resp. Uzb., No. 11, 18 (1994).
8. E. F. Vegman, Yu. G. Rufanov, and I. N. Fedorchenko, *Crystallography, Mineralogy, Petrography, and X-ray Radiography* (Metallurgiya, Moscow, 1990).
9. N. B. Hannay, *Solid-State Chemistry* (Prentice-Hall, Englewood Cliffs, 1967; Mir, Moscow, 1971).

Translated by P. Pozdeev